COMPUTATIONAL MODELLING AND COMPARATIVE DAMAGE ANALYSIS OF ANGIOPLASTY AND ORBITAL ATHERECTOMY INTERVENTIONAL PROCEDURES.

A THESIS

SUBMITTED TO THE FACULTY OF THE

UNIVERSITY OF MINNESOTA

BY

ROHIT R DEOKAR

IN PARTIAL FULFILLMENT OF THE REQUIREMENTS

FOR THE DEGREE OF

MASTER OF SCIENCE

RESEARCH ADVISOR: DR. BARNEY KLAMECKI

AUGUST 2015

ACKNOWLEDGEMENTS

I would like to thank my advisor Prof. Barney Klamecki for all his support and tutelage. He has always been approachable and guided me throughout the course of this research. The weekly meetings and discussions and his constant encouragement definitely got me through the tough times. I have learned a lot from Dr. Klamecki and am forever indebted to his invaluable support. He is a true engineer and his viewpoint and approach towards every problem truly inspires me.

I would like to acknowledge the National Science Foundation for the funding of this Master's research and the Mechanical Engineering department at the University of Minnesota for the teaching support and resources provided. I would like to thank the Minnesota Supercomputing Institute (MSI) for the state of the art computing resources.

I wish to acknowledge the guidance provided by Prof. Henryk Stolarski, Prof. Dominik Schillinger, Prof. Kumar Tamma and his group, Dr. Masao Shimada and Tsunghui Huang. Dr. Tamma helped me develop the fundamental understanding of numerical methods and time integration which paved my way to accomplish the work in this research.

I am grateful to the support by Yihao Zheng, Prof. Albert Shih at the University of Michigan, Robert Kohler at Cardiovascular Systems Inc (CSI) and other members at CSI like Rich Mattison, Victor Schoenle, Alex Nikanorov and Brad Martinsen for the resources and support with the experimental work done.

Thanks to my roommates Arjun and Mustafa and my friends Sampreeti, Biswaranjan, Apurv Ayaan and Nikhita for keeping me motivated throughout these years and always being there for me.

Most importantly I would like to give special thanks to my family, who have always been loving and supportive. The financial and more importantly the emotional support I received from them throughout my life has been unfaltering and I would like to dedicate my work to them.

ABSTRACT

Percutaneous Transluminal Angioplasty (PTA) is frequently used for revascularization of atherosclerotic lesions in patients with peripheral and coronary artery disease. The secondary success rate of the intervention is low due to the process of restenosis which is said to be a response of the tissue to vascular injury post dilation. The stresses and damage in the artery may be an important marker for this process. Morphology of the plaque is an important predictor for these arterial stresses and there is a need to understand the dependence of wall damage to the underlying plaque morphology. Orbital atherectomy (OA) is a minimally invasive interventional procedure used in heavily diseased and calcified lesions. Clinical studies have demonstrated that OA procedure may increase the lesion compliance. However the computational studies for OA procedure are rare. Given the increasing use of OA in clinical practice, a computational investigation of the procedure is in order.

Angioplasty simulations were carried out for a peripheral lesion model based on a histological study of the superficial peripheral artery. The effect of changing the degree of calcification on stresses and damage in the vessel wall during PTA was examined. The results indicate that increasing the degree of calcification increases the peak stresses in the non-calcified portion of the wall making it more susceptible to injury. Plasticity of the lesion components and the original SFA geometry were also considered for some simulations and demonstrate similar results in stresses. In another set of simulations, the influence of decreasing the plaque stiffness on the vessel stresses and damage was investigated. The results show that under the action of a semi-compliant angioplasty balloon, the stresses in the wall decrease with decreasing stiffness of the plaque components. This necessitates the investigation of procedures like atherectomy which are hypothesized to increase lesion compliance.

An experimental study was carried out at Cardiovascular Systems Inc to explore the change in compliance of the lesion post OA procedure. Cadaveric SFA lesion was internally pressurized before and after OA and the cross-sectional lumen areas were recorded using an Optical Coherence Tomography imaging catheter. The analysis of the results showed that there was an increase in compliance of the vessel after OA.

A computational analysis of OA was also carried out based on experimental crown dynamics observed in a study carried out by a fellow researcher, Yihao Zheng at the University of Michigan, Ann Arbor. The same lesion model used in the PTA simulations was used for this study and the results demonstrate that the stress field in OA is quite localized the area of contact near the crown tool. The damage field and peak stresses are therefore localized to the plaque components and the peak stresses in the vessel wall are much smaller than in PTA simulations.

The softening of the plaque components was evident through the damage field and compliance at low internal pressure levels similar to ones used in the experimental investigation was calculated. The results show an increase in compliance at low internal pressure levels after OA procedure.

Damage energy density analysis was carried out for simulations of both the interventional procedures and the damage in the individual components was compared. The results show that the damage in the media and adventitia much smaller in the OA simulations as compared to PTA.

The work presented in this thesis has provided a better understanding of the mechanical response of atherosclerotic lesions to PTA and OA interventional procedures and serve as a basis for future work for computational work in this field.

TABLE OF CONTENTS

LIST OF TABLES

LIST OF FIGURES

1. INTRODUCTION

The heart is the organ responsible to pump oxygenated blood to the different parts of the body through the circulatory system. The human heart is made up of four primary chambers namely, the right atrium and ventricle and the left atrium and ventricle. Deoxygenated blood from different parts of the body is received at the right atrium and is passed onto the right ventricle which pumps it to the lungs through the pulmonary artery. The oxygenated blood is then received from the lungs through pulmonary veins into the left atrium and passed onto the left ventricle which then pumps the blood to various parts of the body through the aorta. Arteries form a crucial part of the circulatory system to carry oxygenated blood from the heart (except pulmonary artery which carries deoxygenated blood).

1.1 THE HUMAN ARTERY

Arteries are broadly classified into two types, namely muscular arteries which have smaller diameters and are located at the peripheries of the arterial tree and larger elastic arteries which are closer to the heart [68]. A histological characterization of arteries [68] for example, revealed that arteries are made up of three distinguishable layers namely the tunica intima which is the innermost layer, the tunica media and the tunica externa or adventitia which is the outermost layer. The intima and media are separated by the internal elastic lamina and the adventitia and the media are separated by the external elastic lamina. A diagram depicting the different layers is shown below in Figure (1.1).The intima is made up of a single layer of endothelial cells lining the wall of the artery. In addition there is also a subendothelial layer of variable thickness depending on location in the arterial tree, age and disease progression. In a healthy artery, the intima is thin and mechanically insignificant as compared to the other layers. However with the progression of atherosclerosis which will be discussed in the next section, intimal thickening and hardening may make the intima mechanically relevant. The media is the intermediate layer made up of smooth muscle cells, and elastin and collagen fibrils which make up a continuous fibrous helix. The fibrils in the media are almost circumferentially oriented. The adventitia is made up of fibroblasts, fibrocytes, ground substance and thick bundles of collagen fibrils. The thickness of the adventitia depends on the type of artery

which in turn depends on the location of the vessel in the arterial tree. The media and adventitia are the mechanically relevant layers of the artery with the media being the most significant. At low strains, the adventitia is pliant but as the strain is increased, the collagen fibers in the layer align making the adventitia quite stiff. [68] Several researchers have studied the properties of the arteries as a whole and of individual layers of the vessel. Proper characterization of the material properties of the tissue is key to characterizing the response of the tissue to various treatment procedures that will be discussed in a later section.

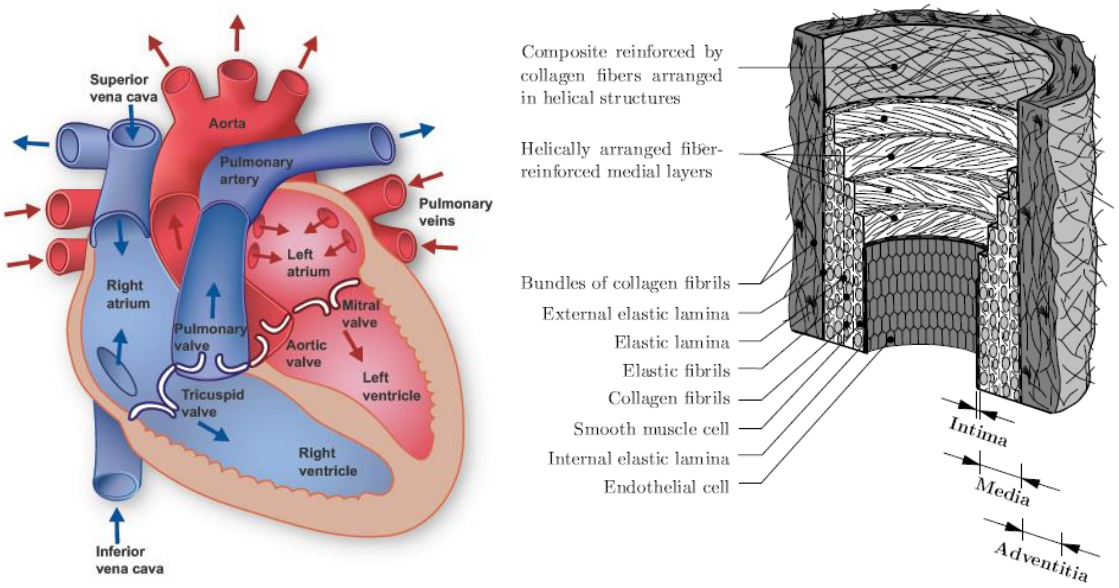

Figure 1.1: *Blood passage in the human heart* [69] *and sectional cut of a model of the human artery showing different layers* [68]

1.2 ATHEROSCLEROSIS

Atheroscelrosis is a build up of plaque which is made up of lipids, cholestrol, fibrotic material, necrotic waste and other things such as calcium deposits in the arterial wall. Deposition of plaque may lead to narrowing of the arterial lumen. Atherosclerosis of the coronary arteries leads to coronary heart disease (CHD) also known as Ischemic heart disease which is the leading cause of death worldwide according to a report by the World Health Organization. In 2014, the number of people in the United States suffering from CHD was 15.4 million. Approximately one in every six deaths in the Unites States in 2010 was caused by CHD. It is considered that approximately every 1 minute 23 seconds,

an American death is caused by a coronary event [70]. Coronary arteries supply blood to the heart muscle. Blockage of coronary arteries causes chest pain known as angina pectoris due to reduced blood flow to the heart muscle. Reduced blood supply to the heart may cause an ischemic heart event such as a myocardial infarction commonly known as a heart attack. In some cases however, vulnerable plaque present in the arteries which does not cause severe blockage can crack and bleed which leads to the cytokines of the arterial wall to capture blood cells that rush to the site of the injury creating a clump/thrombus that may block the artery [69]. Similarly atherosclerosis of peripheral arteries (arteries that supply blood to the legs, arms, stomach or kidneys) causes peripheral arterial disease (PAD) which affects about 8 million people in the United States. PAD in the limbs also known as critical limb ischemia may be asymptomatic for a while. The degree of pain felt depends on severity of blockage is and in severe cases, limb amputations may be needed.

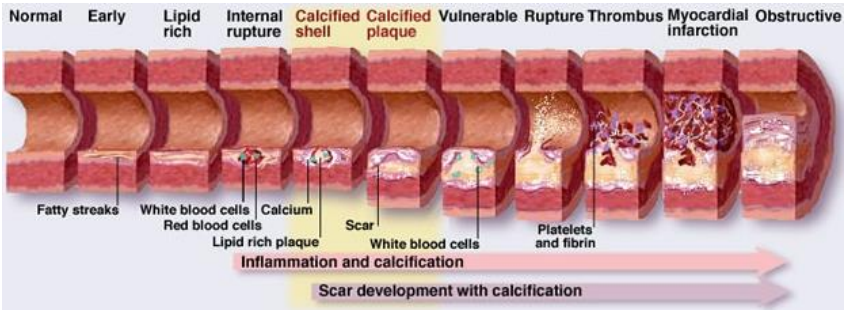

Figure 1.2: *Development of atherosclerotic plaque* [71]

The term atherosclerosis has been coined from two terms namely atheroma which means degeneration of the walls of the arteries caused by fatty deposits and scar tissue, and sclerosis which means hardening of tissue. Atherosclerotic plaque is generally classified into 8 categories according to a histological study by Stary [72]. Type I is made of isolated macrophage foam cells, Type II is multiple layers of foam cells, Type III is a preatheroma which is an intermediate lesion, Type IV is atheroma, Type V is a fibroatheroma, Type VI is a fissured, ulcerated, hemorrhagic thrombotic lesion, Type VII is a calcified lesion and Type VIII is a fibrotic lesion. Types I to III are considered to be early stages of lesion and IV to VIII are considered to be advanced lesions. The study reports that most people have types I and II plaques and the plaque may be stable and not progress thereon. However during puberty some of these lesions get transformed into a

preatheroma (Type III) which then progress on to the atheroma phase (type IV). The classifications after type IV are not chronologically ordered but rather are possible outcomes that form the next stage of the plaque. According to Vogel et al [73], the traditional risk factors for coronary heart disease are hypercholesterolemia, hypertension, cigarette smoking, diabetes mellitus and high fat diet. Males are seen to be more susceptible than women to CHD [70] and postmenopausal women are at a more risk of CHD than premenopausal women.

1.3 TREATMENT PROCEDURES

1.3.1 Percutaneous Transluminal Angioplasty

Percutaneous transluminal angioplasty (PTA) commonly known as balloon angioplasty is one of the most frequently used procedures to reduce plaque burden and increase lumen size in lesions with atherosclerotic plaque buildup. The procedure entails expansion of a cylindrical balloon at the site of the lesion to be treated. In order to carry out the procedure, access is gained into the arterial tree usually through the common femoral, radial or brachial artery sites. A needle is inserted into the access site and a flexible guide wire and a flexible sheath are passed over it. The balloon catheter is passed onto the guidewire to the site of blockage and expanded using internal pressure. The size of the balloon is usually based on the size of the parent vessel to be treated. Once the balloon is fully expanded the balloon is held for 30-120 seconds and then deflated and removed from the site. The complete process is monitored using fluoroscopic imaging. In many cases a PTA is accompanied by stenting which will be discussed in the next section.

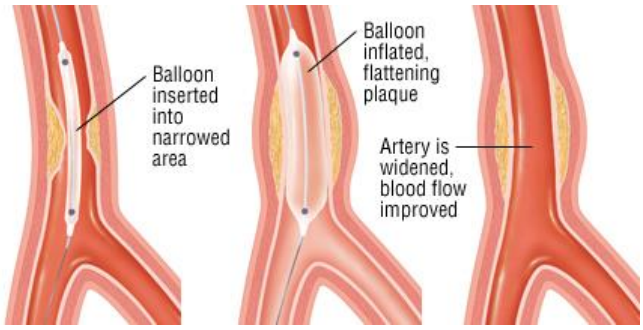

Figure 1.3: *Percutaneous Transluminal Angioplasty, (pre-deployment, inflation and post-intervention)*

The angioplasty procedure takes around 1 to 2 hours to complete and the patient is usually discharged after a night stay at the hospital. The patient can resume normal activities within a week. The PTA procedure is preferred over the alternative coronary artery bypass surgery which is performed in case the blockage is too narrow to pass the balloon catheter or if two or three coronary arteries are occluded. The patient undergoing coronary artery bypass surgery needs to spend around 4-7 days in the hospital and it may take up to 3 months to recover completely. [74]

In the United States around 955,000 angioplasty procedures were performed in the year 2010 [70] and is the most practiced medical intervention worldwide [23] The primary success rates of PTA are seen to be around 91.5% [35] however the secondary success rates are low due to restenosis (re-occlusion) of the treated vessel. The percentage of clinical restenosis for coronary angioplasty was seen to be 36-40% [36]. Restenosis has been attributed to the excessive repair reaction of the artery due to the mechanical damage during the procedure. Mechanical damage during the procedure could be due to overstretching of the arterial wall and denundation of the endothelium due to lesion-balloon interactions. [23]

1.3.2 Stenting

Balloon expanding stents (BX) and self-expanding stents (SX) are used to hold the artery open. BX are manufactured in the crimped state and mounted onto a balloon catheter. On balloon expansion, the BX stent is plastically deformed so that on balloon deflation, the stent stays open and holds the lesion in the expanded state. SX stents are manufactured in their open configuration depending on the parent vessel diameter and then crimped using a constraint so that on removal of the constraint at the site of blockage, the stent opens therefore opening the lumen. [75]

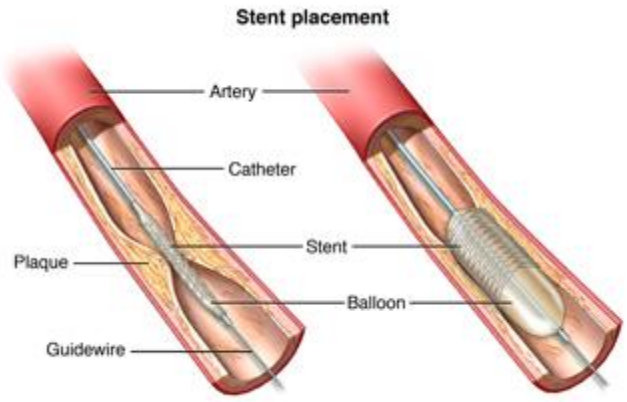

Figure 1.4*: Balloon expandable stent implantation in atherosclerotic lesion* [76]

In the US, about 454,000 stent implantations were carried out in the year 2010 [70]. The restenosis rates associated with stenting are seen to be lower than those observed in the traditional PTA procedure. IJsselmuiden et al [37] observed that the restenosis rates associated with stenting with balloon pre-dilatation was around 18.8 %. As mentioned earlier, restenosis is associated with the vessel's response to injury caused during the interventional procedure. Drug eluting stents were therefore introduced with a coating of a drug to suppress the vessel's response to injury by delayed healing. In 2010, about 75% of the stents implanted during percutaneous coronary interventions were drug eluting stent [70]. Although drug eluting stents provide a promise of reduced restenosis rates [77], increased rates of late stent thrombosis were found in patients with acute myocardial infarction treated with drug eluting stents. In some cases, placing a stent is difficult if the lesion is hardened due to excessive plaque burden. Also in peripheral vessels like the femoropopliteal artery, the vessel is subject to biomechanical forces that exhibit significant twisting, axial compression and bending forces on the stent during leg motion [78,79] which may lead to stent fractures [78]. This necessitates the use of procedures like atherectomy for plaque removal and lesion modification especially in peripheral vessels.

1.3.3 Atherectomy

Atherectomy is a procedure for atherosclerotic plaque removal from the site of disease. Most atherectomy procedures are carried out in patients with peripheral arterial disease.

In the year 2006, atherectomy was performed in 42% of all endovascular procedures in the femoropopliteal artery (FPA) and has contributed in the successful treatment of the FPA disease allowing for revascularization without the need for stenting [61]. The atherectomy procedure is minimally invasive and different mechanisms of action have been implemented, such as rotational, jetstream, directional and orbital atherectomy.

1.3.3.1 Rotational atherectomy

The rotational atherectomy (RA) procedure using the tool by Boston Scientific called the Rotablator, involves a rotating tool called the burr inside the lesion. The burr size is chosen depending on the lumen and vessel size with an optimum burr-to-artery ratio of 0.5-0.6 [80] and rotational speeds of 140,000 to 150,000 rpm. The rotating burr is advanced through the length of the lesion and produces lumen enlargement by physically removing the plaque and by reducing plaque rigidity to facilitate PTA procedure. The device is shown in the figure (1.5) below.

Figure 1.5 *Rotablator device (peripheral), advancer and some of the available burr sizes for the device.* [81]

The burr of the Rotablator device is diamond-encrusted and driven by a helical driveshaft. Owing to the mechanism of action, RA is said to produce lesser intimal splits and medial dissections in lesions with high calcification content as compared to the PTA procedure. The device has been approved for coronary and peripheral interventions.

1.3.3.2 Jetstream

The Jetstream device (Boston Scientific) for atherectomy was initially designed by Pathway Medical and was cleared by FDA for use in peripheral atherectomy procedures in 2009.

Figure 1.6: *Jetstream device for atherectomy procedure in peripheral lesions* [82]

The atherectomy tool is made of rotating cutters that were designed with a principle of differential cutting taking advantage of the faster rate of removal at lower rotational speeds. The device is said to be designed to work for all types of plaque morphologies. [83]

1.3.3.4 Directional Atherectomy

Directional atherectomy, using devices like the SilverHawk and TurboHawk by Covidien, is a minimally invasive procedure for plaque removal in patients with peripheral arterial disease. During the intervention, the device is guided to the location of the plaque buildup and plaque is removed using a cutting tool shown in Figure (1.7).

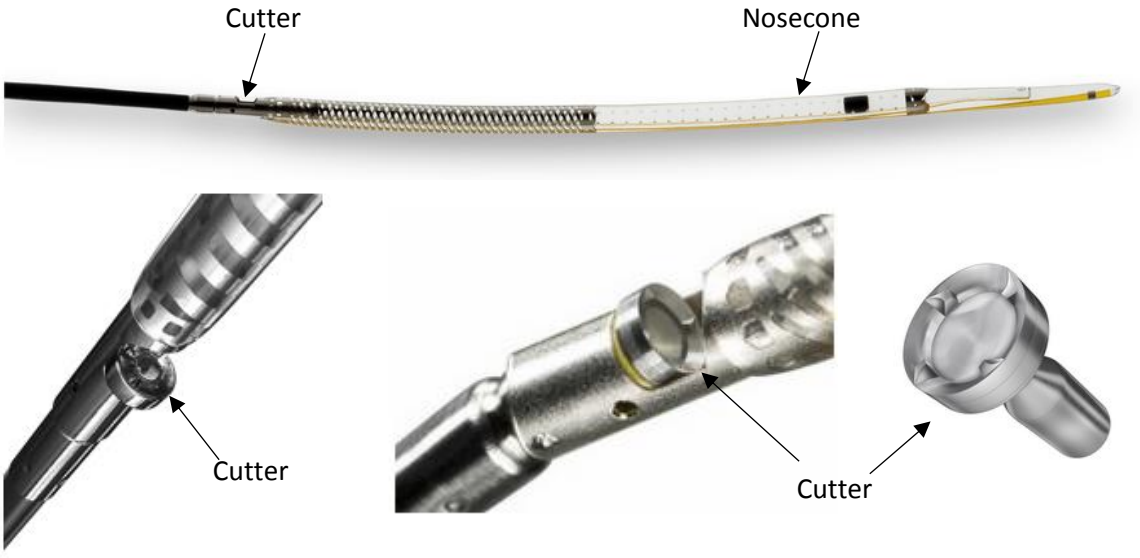

Figure 1.7: *Directional atherectomy devices, Silverhawk and Turbohawk repsectively* [84]

The cutting tool for the SilverHawk has a single inner blade while the TurboHawk has 4 contoured blades to be used in highly calcified lesions and to allow more plaque removal per pass. The devices come in variable sizes and are suitable to work with vessels of diameters 1.5-7mm. [85] The SilverHawk device is said to be more suitable for eccentric lesions. The nosecone as shown in Figure (1.7) above is used to pack the plaque after excision. Due to the nature of the operation not being overstretching of artery or internal pressure, the device has an advantage of lack of barotrauma and lesser risk of dissections. As discussed by Akkus et al [85] distal embolization is the main disadvantage of the directional atherectomy system. The two aforementioned devices are US FDA approved for use in atherectomy of peripheral diseases but not coronary carotid or renal arteries [85]

1.3.3.5 Orbital Atherectomy

Orbital atherectomy (OA) is a procedure for plaque removal and lesion modification with the use of a diamond-coated eccentric crown spinning and orbiting inside the lumen. The Diamondback 360^{o} device (Cardiovascular Systems Inc.) has been designed to allow for differential sanding which is said to flex away the healthy vessel wall therefore affecting the hardened plaque [62]. The device is used in the treatment of mild to severely calcified lesions.

Figure 1.8: *Diamondback 360^{o} device handle for peripheral procedures and diamond-coated crowns*. [63]

The device is US FDA approved for interventions in coronary and peripheral arterial disease. Three types of crowns are used for the orbital atherectomy system, namely the Classic crown, the Solid crown and the Predator crown depending on their size and objective of operation [62]. The rotational speeds levels of driveshaft typically used in

practice are 60,000 rpm, 90,000 rpm and 120,000 rpm. The crown is seen to orbit around the vessel lumen at orbiting frequencies much smaller than the rotational frequencies [64]. A saline supply unit is used in combination with the tool to deliver saline through a sheath to the lesion being treated to remove the heat generated from the friction. The mean particle size from sanding during OA is seen to be 1.7μm to 3.1μm and expected to be small enough to be removed through the normal reticuloendothelial system [90].

1.4 **OBJECTIVE OF THE THESIS**

Percutaneous transluminal angioplasty (PTA) discussed above is one of the most common lines of treatment for patients with coronary or peripheral arterial disease however it suffers from high rates (36-40%) of restenosis [36]. One of the primary mechanisms of PTA is said to be overstretching of the non-diseased portion of the artery [26]. Restenosis has been associated with vascular injury and increasing arterial stresses [58]. Inelastic effects like arterial weakening or damage and permanent deformation are seen during angioplasty [26]. Plaque morphology and presence of calcification also have a key role in determining the vessel's response during angioplasty [86] and stresses observed in the media [61]. Therefore it is important to understand the stresses and damage in the vessel during PTA and how varying the plaque morphology affects the response of the vessel.

The rates of restenosis with the use of stent implantation have been found to be lower. However, as reported by studies, stenting may not be viable in some cases for patients with PAD therefore necessitating the need for procedures like atherectomy. The atherectomy procedure was built around the idea of reducing plaque burden without significantly affecting the rest of the arterial wall. In addition, clinical investigation of orbital atherectomy has demonstrated an increase in lesion compliance post procedure [31], and lesser dissections were observed during PTA when pre-treated with OA [30]. Change in the compliance suggests that there may be a modification of material properties during the procedure. To the author's knowledge, no numerical/computational studies investigating the vessel structural response to OA procedure are seen in the literature. Given the increasing use of OA procedures for treatment of PAD, a computational analysis of the same is in order.

Therefore the objective of the work presented in this thesis is twofold,

- To characterize the stresses and damage in the arterial wall of a superficial femoral artery (SFA) lesion with a variable plaque morphology during balloon angioplasty procedure,
- To evaluate the effect of orbital atherectomy procedure on arterial stresses and damage in SFA lesions with calcified plaque in order to observe the change in compliance that has been reported clinically

Finite element simulations based on experimental material data are presented for PTA and OA procedures and the stresses and damage in the vessel wall are reported. Experimental work and numerical simulations were conducted to investigate the change in lesion compliance during OA procedure.

The scope of this thesis has a certain assumptions and limitations that are outlined at the end of the thesis.

1.5 **ORGANIZATION OF THE THESIS**

The thesis was organized in a way to build the understanding and familiarity of the reader with the subject at hand. Chapter 2 is a review of the key concepts in continuum mechanics, material models, damage and nonlinear finite element analysis.

Chapter 3 is a the literature review of experimental material properties of tissues, computational trends seen in modelling of interventional procedures, some key damage modelling theories related to biological tissues and clinical observations related to the treatment procedures like PTA and OA.

Chapter 4 discusses experimental data which are used to describe the tissue behaviour in this thesis. Material model fits used in this research, their stability and verification has been carried out in this chapter.

Chapter 5 presents the computational set up of the PTA simulations. The results for various iterations of plaque morphology, plaque material properties, variable geomtries and paramaters are presented.

Chapter 6 inlcudes the Experimental investigation of OA based on work done at Cardiovascular Systems Inc (CSI) and has been reported with permission from CSI. In addition, numerical simulations demonstrating tissue reponse in the lesion are also conducted. The results for stress fields and damage have been reported.

In Chapter 7, a discussion section with key findings from the simulations and a note of the limitations of current work along with the future work are presented.

2. KINEMATICS OF DEFORMATION AND THEORY OF HYPERELASTICITY

Biological tissues undergo large deformations during processes like balloon angioplasty and atherectomy that were discussed in the previous chapter. The material response at such large strains for cardiovascular tissues is highly nonlinear. In order to capture the experimentally observed material response, an understanding of nonlinear material models and continuum mechanics is a must. Therefore this chapter will be dedicated to outlining the theory necessary to accurately represent these processes using mathematical models and numerical methods to solve them.

The fundamental theory of continuum mechanics and non-linear finite element analysis can be found in several texts. Some of the key-concepts that serve as a revision of these fundamentals have been outlined below. Interested readers are encouraged to refer to the textbook by Bonet and Wood [87] for a detailed understanding.

2.1 LAGRANGIAN AND EULERIAN DESCRIPTION

A deformable body Ω shown in Figure (2.1) has been resolved using the Cartesian orthonormal bases, X_1, X_2 and X_3. This undeformed configuration of the body is known as the reference configuration or the initial configuration. The basis vectors are known as the reference basis and will hence forth be depicted as X_i in the indicial form or **X** in vector form. The body Ω is then transformed into a deformed configuration by a combination of rotation, translation and deformation of the body. This new configuration of the body is known as the deformed configuration resolved into the orthonormal bases x_1, x_2 and x_3 denoted as x_i in the indicial form or **x** in the vector form. In order to maintain physical form, this transformation must be a one to one mapping such that every point in the reference configuration will be mapped to one and only one corresponding point in the deformed configuration.

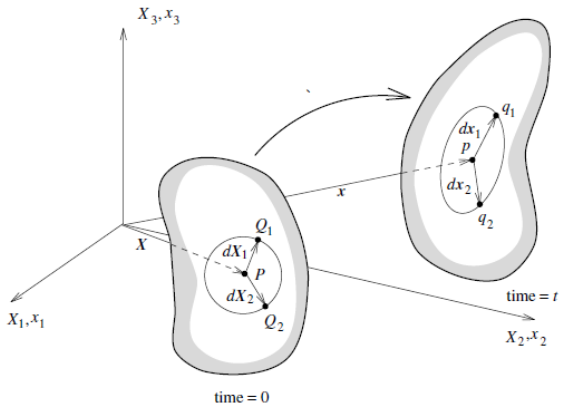

Figure 2.1 *Motion of a body from the reference to deformed configuration and local deformation field at a point on the body* [87]

Let this transformation be denoted mathematically by ϕ such that,

$$x = \phi(X, t) \tag{1}$$

where t denotes the time variable. The displacement of every point in the body is given by **u = x-X.** This displacement can be large or small and therefore no small deformation assumptions have been made. Quantities such as volume, density etc. can be described in the reference configuration or in the deformed configuration. The former is known as the Lagrangian or the material description and the latter is known as the Eulerian or the spatial description. For problems in solid mechanics it is often easier to use the Lagrangian description and therefore all quantities will be described in the reference configuration henceforth.

2.2 DEFORMATION GRADIENT

The simplest and one of the most important underlying quantities in continuum mechanics is the deformation gradient, often denoted by **F.** It is a mapping of all quantities in the undeformed configuration to the corresponding quantities in the deformed configuration. It enables the description of relative spatial position of two neighboring particles during the process of deformation and therefore is a key concept to describe the strain in the body. [87]

An infinitesimal vector **dX** in the reference configuration is mapped to a vector **dx** during the deformation. The deformation gradient is then given by,

$$F = \frac{\partial \phi(\mathbf{X}, t)}{\partial \mathbf{X}} = \nabla \phi \tag{2}$$

$$\mathbf{dx} = F.\,\mathbf{dX} \tag{3}$$

Since the deformation gradient maps vectors from the initial configuration to vectors in the deformed configuration, it is known as a two point tensor.

If e_i and E_i are unit vectors in the deformed and reference configuration respectively, then the deformation gradient in indicial notation is given by,

$$F = F_{iJ} e_i \otimes E_J \; ; \quad F_{iJ} = \frac{\partial x_i}{\partial X_j} \tag{4}$$

2.3 POLAR DECOMPOSITION THEOREM

According to the polar decomposition theorem, the transformation from the reference to the deformed configuration can be split into rotation and stretch. Therefore the mapping described by the deformation gradient tensor **F** can be multiplicatively split into an orthogonal rotation tensor **R** and a Stretch tensor **U** such that,

$$F = RU \tag{5}$$

It is worth noting that if the body Ω undergoes a rigid body translation, the deformation gradient is the identity tensor, however if the body undergoes a rigid body rotation, the deformation gradient is not the identity tensor. Therefore another tensor called the right Cauchy green deformation tensor **C** is defined such that

$$C = F^T F = (RU)^T RU = U^T R^T R\, U = U^T U = U^2 \tag{6}$$

Since R is orthogonal, $R^T R = I$. Similarly, the deformation gradient can be split multiplicatively such that,

$$F = VR \tag{7}$$

Where R is the same orthogonal tensor and V is a stretch tensor. The difference in equations (5) and (7) is that in the former, the body is stretched in the reference basis **X** and then rotated and in the latter, the body is first rotated into the deformed basis **x** and then stretched. Therefore the tensor **U** is the material stretch tensor and the tensor V is the spatial stretch tensor.

The left Cauchy green deformation tensor **b** is defined such that

$$b = FF^T = VR(VR)^T = VRR^TV^T = VV^T \tag{8}$$

The tensors **C** and **b** can be seen to be independent of rigid body rotations and therefore are true measures of the deformation the body undergoes. They can therefore be used to describe strain.

2.4 STRAIN MEASURES

The Lagrangian measure of strain better known as the Green Strain is defined as

$$E = \frac{1}{2}(F^TF - I) = \frac{1}{2}(C - I) \tag{9}$$

As stated earlier, the displacement is given by

$$u = x - X \tag{10}$$

$$\therefore \nabla_0 u = \frac{\partial u}{\partial X} = \frac{\partial (x - X)}{\partial X} = \frac{\partial x}{\partial X} - \frac{\partial X}{\partial X} = F - I \tag{11}$$

$$\therefore F = \nabla_0 u + I \tag{12}$$

$$\therefore F^TF = (\nabla_0 u + I)^T(\nabla_0 u + I) = I + \nabla_0 u + \nabla^T{}_0 u + \nabla^T{}_0 u.\nabla_0 u \tag{13}$$

The Green Strain therefore can also be expressed as

$$EE = \frac{1}{2}(F^TF - I) = \frac{1}{2}(I + \nabla_0 u + \nabla^T{}_0 u + \nabla^T{}_0 u.\nabla_0 u - I) \tag{14}$$

$$\therefore E = \frac{1}{2}(\nabla_0 u + \nabla^T{}_0 u + \nabla^T{}_0 u.\nabla_0 u) \tag{15}$$

If the quadratic term $\nabla^T{}_0 u.\nabla_0 u$ is neglected, the Green strain reduces to the linearized strain measure

$$Ee_{lin} = \frac{1}{2}(\nabla_0 u + \nabla^T{}_0 u) \tag{16}$$

Similar to the Lagrangian description, another strain measure in the spatial description called the Almansi-Green Strain is defined as

$$e = \frac{1}{2}(I - F^{-T}F^{-1}) = \frac{1}{2}(I - b^{-1}) \tag{17}$$

For small deformation case, the Green strain and the Almansi-Green Strain reduce to the linearized strain. Further, in the undeformed state, $F = I$, therefore, $E = e = e_{lin} = 0$.

2.5 VOLUME CHANGE

The change in volume of the body Ω during the transformation from reference to deformed configuration is calculated by the Jacobian of the deformation gradient F. Consider a volume element with edges aligned with the axes X_1, X_2 and X_3 given by dX_1, dX_2 and dX_3. The volume of the element is given by

$$dV = dX_1 dX_2 dX_3 \tag{18}$$

The deformation gradient transforms every vector dX into another vector dx such that,

$$dx_1 = FdX_1;\ dx_2 = FdX_2\ ; dx_3 = FdX_3 \tag{19}$$

The volume after deformation is given by the triple product,

$$dv = dx_1(dx_2 \times dx_3) = \det F\, dX_1 dX_2 dX_3 \tag{20}$$

$$\therefore dv = \det F\ dV = J\, dV \tag{21}$$

where J is the Jacobian or the determinant of the deformation gradient

Similarly the density by inverse relation is given by

$$\rho_0 = J\rho \tag{22}$$

2.6 DISTORTIONAL COMPONENT

Many materials in literature are formulated as incompressible or nearly incompressible materials. When dealing with such materials, the deformation gradient F is split into a distortional component $\hat{F}$ and a volumetric component. The distortional component is the isochoric part of the deformation gradient and therefore, we must have

$$\det \hat{F} = 1 \tag{23}$$

By choosing the distortional component $\hat{F}$ such that,

$$\hat{F} = J^{-\frac{1}{3}}F \tag{24}$$

$$\det \hat{F} = \det\left(J^{-\frac{1}{3}}F\right) = \det J^{-\frac{1}{3}} \det F = \left(J^{-\frac{1}{3}}\right)^3 \det F = J^{-1}J = 1 \tag{25}$$

Therefore the deformation gradient and the right Cauchy green deformation tensor can be written as

$$\mathrm{F} = \mathrm{J}^{\frac{1}{3}}\,\hat{\mathrm{F}}\,;\;\; \mathrm{C} = \mathrm{J}^{\frac{2}{3}}\,\hat{\mathrm{C}} \tag{26}$$

The distortional components and volumetric components are used to formulate their respective stiffness matrices. Special treatment of the volumetric component is carried out to take care of volumetric locking.

2.7 STRESS MEASURES

2.7.1 Cauchy Stress

Cauchy stress or True stress σ is defined as the Force per unit area in the deformed configuration at a given instant. The Cauchy stress at a point is a 2^{nd} order tensor and can be resolved into the three basis vectors dx_i to give 9 components. The force or traction vector **t** acting at a given point with normal **n** can be expressed in terms of the Cauchy stress.

$$\mathrm{t} = \sigma.\,\mathrm{n} \tag{27}$$

$$\sigma = \sigma_{ij}\,\mathrm{e_i} \otimes \mathrm{e_j} \tag{28}$$

By the principle of conservation of angular momentum, Cauchy stress is a symmetric tensor.

2.7.2 First Piola-Kirchoff Stress

The First Piola Kirchoff (PK) stress tensor P is defined as the Force in the deformed configuration per unit area in the reference configuration. Therefore, similar to the deformation gradient, the first PK stress is a two point tensor. An element of force dt acting on an element of deformed area da is expressed using the Cauchy stress tensor as $\mathrm{dt} = \sigma\mathrm{da}$. Similarly, this area can be expressed in the undeformed configuration dA using Nanson's Formula ($\mathrm{da} = \mathrm{JF^{-T}dA}$) such that,

$$\mathrm{dt} = \sigma\mathrm{da} = \sigma\mathrm{J}\,\mathrm{F^{-T}dA} = \mathrm{P}\,\mathrm{dA} \tag{29}$$

$$\therefore \mathrm{P} = \mathrm{J}\sigma\,\mathrm{F^{-T}} \tag{30}$$

$$\mathrm{P} = \mathrm{P_{iJ}}\,\mathrm{e_i} \otimes \mathrm{E_j} \tag{31}$$

The First Piola Kirchoff Stress Tensor is not symmetric. As discussed later, it is a work conjugate of the deformation gradient F.

2.7.3 Second Piola-Kirchoff Stress

The second PK stress tensor *S* is defined as the force in the undeformed configuration per unit area in the undeformed configuration. It is created by performing a pull-back operation on the force from the deformed to the reference configuration using the inverse deformation gradient mapping.

$$dT = F^{-1}dt \tag{32}$$

$$\therefore dT = F^{-1}PdA = JF^{-1}\sigma F^{-T}dA = S\,dA \tag{33}$$

$$\therefore S = JF^{-1}\sigma F^{-T} \tag{34}$$

Since the Cauchy Stress σ is symmetric, the above formula suggests that the second PK stress is also a symmetric tensor. This makes it much easier to work with as compared to the First PK stress. The second PK stress is the work conjugate of the Green Strain E.

2.8 PRINCIPLE OF VIRTUAL WORK AND WORK CONJUGATE MEASURES

The principle of virtual work is a weak form formulation which can be derived by multiplying the governing equation by a test function and integrating the residual over the deformed volume dV of the body Ω. The solution procedure is analogous to Galerkin weighted residual formulation. The governing equation in structural mechanics is basically a Newton's law F= ma given by

$$\sigma_{ij,j} + \rho b_i = \rho \ddot{u}_i \tag{35}$$

where u is the displacement field and b is the body force per unit volume. The residual is defined as, $R = \sigma_{ij,j} + \rho b_i - \rho \ddot{u}_i$ and the Galerkin weighted residual method gives,

$$\int \delta v\,.\ R\,dV = 0 \tag{36}$$

$$\therefore \int \delta v_i\, \sigma_{ij,j} dV + \int \delta v_i\, \rho b_i\, dV - \int \delta v_i\, \rho \ddot{u}_i dV = 0 \tag{37}$$

where δv is a test function which is an admissible virtual velocity that conforms to the boundary conditions the body is subject to. On using the divergence theorem on the first term and denoting the resulting surface integral by a traction boundary term, equation (37) becomes,

$$\therefore \int \sigma_{ij}\delta D_{ij}\, dV + \int \delta v_i\, \rho \ddot{u}_i dV - \int \delta v_i\, \rho b_i\, dV - \int \delta v_i\, t_i\, dA = 0 \qquad (38)$$

where t is a traction vector over the deformed boundary domain dA and D_{ij} is the strain rate tensor. The Cauchy stress σ and the strain rate tensor D are doubly contracted to give a product equivalent to the internal work of the system. Therefore the two quantities are known as work conjugates. Equation (38) is known as the Principle of Virtual power (POVP). The POVP can be equivalently written in terms of reference configuration with volume dV_0 and area dA_0. The Stress and strain quantities used are referred to the reference configuration

$$\therefore \int S_{ij}\delta \dot{E}_{ij}\, dV_0 + \int \delta v_i\, \rho_0 \ddot{u}_i dV_0 - \int \delta v_i\, \rho_0 b_i\, dV_0 - \int \delta v_i\, t_i\, dA_0 = 0 \qquad (39)$$

Similarly using a test function of virtual displacement, one can formulate the Principle of Virtual Work (POVW),

$$\int S_{ij}\delta E_{ij}\, dV_0 + \int \delta u_i\, \rho_0 \ddot{u}_i dV_0 - \int \delta u_i\, \rho_0 b_i\, dV_0 - \int \delta u_i\, t_i\, dA_0 = 0 \qquad (40)$$

where the Second PK stress and the Green strain are used as work conjugate measures in the reference configuration. As mentioned earlier, the First Piola Kirchoff stress tensor P and the deformation gradient tensor are also work conjugates.

The Principle of Virtual Work is in essence an energy balance equation which forms the basis for numerical formulations in solid mechanics with the use of techniques like the Finite Element method that will be discussed in a later section.

2.9 HYPERELASTICITY

Materials for which the constitutive behavior is only a function of the current state of deformation are known as elastic. In special cases when the work done by the stresses during a deformation process is dependent only on the initial state and the final configuration, the behavior of the material is said to be path independent and the material is termed to be hyperelastic [87]. For such materials, the stored strain energy or elastic potential ψ per unit volume can be written in terms of the current state variables. These materials are known as Hyperelastic materials

$$\psi(F(X), X) = \int P(F(X), X) : \dot{F} dt \quad \text{or} \quad \psi(E(X), X) = \int S(E(X), X) : \dot{E}\, dt \qquad (41)$$

$$\therefore \mathrm{P}(\mathrm{F}(\mathrm{X}),\mathrm{X}) = \frac{\partial \psi(\mathrm{F}(\mathrm{X}),\mathrm{X})}{\partial \mathrm{F}} \quad \text{and } \mathrm{S}(\mathrm{E}(\mathrm{X}),\mathrm{X}) = \frac{\partial \psi(\mathrm{F}(\mathrm{X}),\mathrm{X})}{\partial \mathrm{E}} \tag{42}$$

2.10 STRAIN ENERGY DENSITY

The strain energy potential per unit volume is known as Strain energy density and the functional ψ is known as the Strain energy density function.

2.10.1 Strain energy density for isotropic materials

Isotropic materials are required to have the same constitutive model behavior irrespective of the direction in which the properties are measured. Therefore the Strain energy must be independent of the material axes and therefore the Strain energy density function ψ must be invariant of the material orientation and therefore is expressed as a function of invariants of the right Cauchy green deformation tensor C. The first three invariants of C are

$$\mathrm{I}_1 = \mathrm{tr}(\mathrm{C}) \tag{43}$$

$$\mathrm{I}_2 = \frac{1}{2}\left(\left(\mathrm{tr}(\mathrm{C})\right)^2 - \mathrm{tr}(\mathrm{C}^2)\right) \tag{44}$$

$$\mathrm{I}_3 = \det \mathrm{C} = \mathrm{J}^2 \tag{45}$$

The strain energy density function ψ for isotropic materials is therefore given as

$$\psi\,(\mathrm{C}(\mathrm{X}),\mathrm{X}) = \psi(\mathrm{I}_1,\mathrm{I}_2,\mathrm{I}_3,\mathrm{X}) \tag{46}$$

The second Piola Kirchoff stress can be written as

$$\mathrm{S} = \frac{\partial \psi(\mathrm{E}(\mathrm{X}),\mathrm{X})}{\partial \mathrm{E}} = \frac{\partial \psi(\mathrm{C}(\mathrm{X}),\mathrm{X})}{\partial \mathrm{C}} \cdot \frac{\mathrm{dC}}{\mathrm{dE}} = \frac{\partial \psi(\mathrm{C}(\mathrm{X}),\mathrm{X})}{\partial \mathrm{C}} : 2\mathrm{I}^4 = 2\frac{\partial \psi}{\partial \mathrm{C}} \tag{47}$$

Where I^4 is the fourth order identity tensor

$$\therefore \mathrm{S} = 2\frac{\partial \psi}{\partial \mathrm{C}} = 2\left(\frac{\partial \psi}{\partial \mathrm{I}_1}\frac{\partial \mathrm{I}_1}{\partial \mathrm{C}} + \frac{\partial \psi}{\partial \mathrm{I}_2}\frac{\partial \mathrm{I}_2}{\partial \mathrm{C}} + \frac{\partial \psi}{\partial \mathrm{I}_3}\frac{\partial \mathrm{I}_3}{\partial \mathrm{C}}\right) \tag{48}$$

These derivatives can be evaluated easily as

$$\frac{\partial I_1}{\partial C} = \frac{\partial \mathrm{tr}(C)}{\partial C} = I\,;\ \frac{\partial I_2}{\partial C} = \frac{1}{2}\frac{\partial\left(\left(\mathrm{tr}(C)\right)^2 - \mathrm{tr}(C^2)\right)}{\partial C} = \frac{1}{2}\,(2\,\mathrm{tr}(C)I - 2C^T) \tag{49}$$
$$= I_1 I - C\,;\ \frac{\partial I_3}{\partial C} = \frac{\partial \det C}{\partial C} = \det C\ C^{-1}$$

2.10.2 Elasticity Tensor

The elasticity tensor gives the relation between the strain and the conjugate stress of the material such that,

$$S_{ij} = C_{ijkl}E_{kl}\,;\, C_{ijkl} = \frac{\partial S_{ij}}{\partial E_{kl}} = \frac{4\,\partial^2 \psi}{\partial C_{ij}\,\partial C_{kl}} \tag{50}$$

Most biological tissues are modelled as incompressible or nearly incompressible materials, therefore henceforth; the strain energy density functions presented will be those for an incompressible material.

2.10.3 Isotropic Material models

The strain energy density function (SEDF) completely governs the material response and therefore when defining a Hyperelastic material, the SEDF is the most important material relation. Some of the most common material models and the models relevant to this thesis will now be presented below.

2.10.3.1 Neo Hookean model

The Neo Hookean material is one of the simplest hyperelastic materials. In the case of incompressible material, the strain energy density function of this type is a function of its first invariant only.

$$\psi = \frac{\mu}{2}(I_1 - 3) \tag{51}$$

The Neo hookean material model is based on the statistical thermodynamics of cross-linked polymer chains and is is used to model rubber-like materials in the initial linear strain range. The Neo-Hookean material is generally known to not accurately predict the material response at large strains.

2.10.3.2 Mooney Rivlin and Polynomial model

The Strain Energy density function of the Mooney Rivlin type is a special form of the polynomial model for incompressible rubbers. It is a function of the first and the second invariants of C. In general form the polynomial model is expressed as,

$$\psi(C) = \sum C_{rs} (I_1 - 3)^r (I_2 - 3)^s \quad \text{where } r, s \geq 0 \tag{52}$$

The 2 term form of the polynomial model or the Mooney Rivlin material is given by $r, s = (1,0) \text{and } (0,1)$ such that

$$\psi(C) = C_{10} (I_1 - 3) + C_{01}(I_2 - 3) \tag{53}$$

The two term Mooney Rivlin model reduces to the Neo-Hookean material when C_{01} is set to 0. The two term material model is said to describe the material response to up to 200% strain levels. [88]

2.10.3.3 Ogden material model

The Ogden material is often used to predict Non-linear stress strain response of materials like rubber or polymers. It was introduced by Ogden in 1972 and the strain energy density is expressed in terms of Stretch ratios instead of invariants.

$$\psi = \sum_{i=1}^{N} \frac{\mu_i}{\alpha_i} (\lambda_1^{\alpha} + \lambda_2^{\alpha} + \lambda_3^{\alpha} - 3) \tag{54}$$

Where N is the order of the Ogden function, the $\lambda' s$ are principal stretch ratios, $\alpha' s$ and $\mu' s$ are material constants. The Ogden material model is known to show good agreement for material response to upto 700% strain results [88]. A third order Ogden function is used in this thesis to describe the plaque response as will be discussed in the forthcoming section on Material modelling and Verification.

2.10.3.4 Yeoh Model

The Yeoh material model is completely based on the first invariant of the Cauchy green deformation tensor. It is also known as a third order reduced polynomial form. The strain energy density function for the Yeoh model has been given below.

$$\psi(I_1) = \sum_{i=1}^{3} C_{i0}\,(I_1 - 3)^i \tag{55}$$

Stability of this model is ensured if all the material constants are positive. This material model has been traditionally used to describe isotropic rubber with carbon black.

2.10.4 Anisotropic Hyperelastic Material models

An important characteristic of biological tissues is the anisotropy induced as a result of the collagen fibers that are distributed in the material and therefore make the material direction dependent. As discussed later in the chapter on Literature review soft tissues like the artery walls have two distinct distributions of collagen fiber directions associated with collagen fiber orientations.

2.10.4.1 Fung's Model

Fung was one of the first to describe the anisotropic material behavior of biological tissues using a phenomenological material model. The strain energy density function for the same is given by

$$\psi = \frac{C}{2}(e^Q - 1) \tag{56}$$

Where, $Q = A_1\varepsilon_{11}^2 + A_2\varepsilon_{22}^2 + 2A_3\varepsilon_{11}\varepsilon_{22} + A_4\varepsilon_{12}^2 + 2A_5\varepsilon_{11}\varepsilon_{12} + 2A_6\varepsilon_{12}\varepsilon_{22}$

And ε_{ij} are green strain components and A_i are material constants

2.10.4.2 Holzapfel Gasser Ogden (HGO) Model

The Strain energy density function in this case is a function of the invariants of the right Cauchy deformation tensor along with an additional set of invariants which are function of the direction of orientation of the fiber-vectors a_1, a_2.

$$\psi\,(C, a_1, a_2) = \psi_{iso}(C) + \psi_{aniso}(C, a_1, a_2) \quad \text{or eqivalently,} \tag{57}$$

$$\psi(I_1, I_2, I_4, I_5, I_6, I_7, I_8) = \psi_{matrix}(I_1, I_2) + \psi_{fiber}(I_1, I_2, I_4 \dots\dots I_8) \tag{58}$$

$$\text{where } I_1 = \mathrm{tr}(C); \quad I_2 = \frac{1}{2}\left(\left(\mathrm{tr}(C)\right)^2 - \mathrm{tr}(C^2)\right); \quad I_3 = \det C \tag{59}$$

$$I_4 = C{:}A_1\ ;\ I_5 = C^2{:}A_1\ ;\ I_6 = C{:}A_2\ ;\ I_7 = C^2{:}A_2\ ;\ I_8 = (a_1.a_2)\,a_1.C.a_2\ \ \&\ A_i = a_i \otimes a_i \text{ (no sum)} \tag{60}$$

In order to reduce the number of parameters, the strain energy density function for arterial layers is reduced to a simpler form

$$\psi = \psi_{\text{matrix}}(I_1) + \psi_{\text{fiber}}(I_4, I_6) \tag{61}$$

The anisotropy is accounted for by the fiber component of the strain energy function which is a function of the invariants I_4 *and* I_6. The matrix and the fiber strain energies introduced by Holzapfel et al are

$$\psi_{\text{matrix}} = \frac{c}{2}(I_1 - 3)\,; \quad \psi_{\text{fiber}} = \frac{k_1}{2k_2}\sum_{i=4,6}[\exp(k_2(I_i - 1)^2) - 1] \tag{62}$$

Where c, k_1, k_2 are material parameters, specific to a given layer of the artery, I_4 and I_6 are functions of the fiber orientation vectors which in turn are dependent on the angle ϕ at which the fiber is oriented [89].

2.11 MULLINS EFFECT, DAMAGE ENERGY

Similar to rubber, elastomers follow stress softening when cyclically loaded and unloaded from their virgin state. The material model for softening can be described by Mullin's Effect. When such a material is loaded, it follows the primary path, b between a-b' as shown in Figure (2.2). On unloading from b', the path taken by the material is B. The material follows the same path B on reloading from a to b' and then follows the path c on further loading, which is a part of the original primary path.

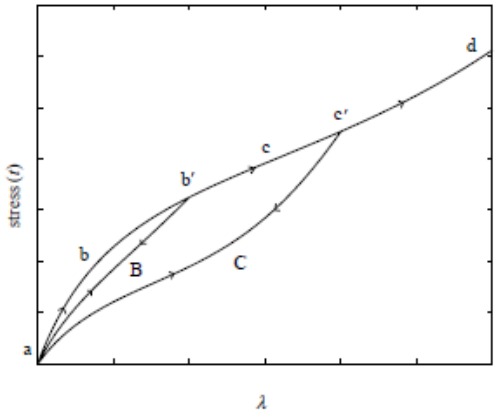

Figure 2.2 *Mullin's effect in a material under uniaxial loading and unloading* [15]

The model first described by Ogden and Roxburgh in 1998 is based on an incompressible isotropic elastic material amended by a single continuous parameter interpreted as a damage parameter. This damage variable stores the history of deformation and material response is governed by a strain energy function which is different in loading and unloading (and subsequent reloading). This model is referred to as a pseudo elastic material model. The dissipation is measured by the damage variable. [15] In Abaqus, the amount of energy dissipated on loading and unloading is known as Damage Energy. The strain energy function is modified to be a function of an additional variable called the damage variable η as mentioned above.

$$\psi(\lambda_1, \lambda_2, \lambda_3, \eta) = \eta\, \bar{\psi}(\lambda_1, \lambda_2, \lambda_3) + \phi(\eta) \tag{63}$$

Where $\phi(\eta)$ is known as the damage function. The damage variable $\eta = 1$ for as long as the material is not unloaded and $\phi(1) = 0$.

For simplicity, we will consider the biaxial deformation case as mentioned in [15],

$$\psi(\lambda_1, \lambda_2, \eta) = \eta\, \bar{\psi}(\lambda_1, \lambda_2) + \phi(\eta)\ ;\ \ \sigma_i - \sigma_3 = \eta\, \lambda_i \frac{\partial \bar{\psi}}{\partial \lambda_i} \tag{64}$$

If the material is not been unloaded, the value of $\eta = 1$ therefore the stress response of the material follows the primary hyperelastic curve. However once unloaded, the value of η is a function of value of ψ at the maximum loaded state, such that

$$\eta = 1 - \frac{1}{r}\,\mathrm{erf}\left[\frac{1}{m}\left(\psi_m - \bar{\psi}(\lambda_1, \lambda_2)\right)\right] \tag{65}$$

Where ψ_m is the value of the strain energy at the maximum loading and m and r are material constants. In Abaqus, the expression for η is a modified form of equation (65) with an additional material parameter β

$$\eta = 1 - \frac{1}{r}\,\mathrm{erf}\left[\frac{\left(\psi_m - \bar{\psi}(\lambda_1, \lambda_2)\right)}{m + \beta\psi_m}\right] \tag{66}$$

2.11.1 Dissipation or Damage energy

On complete unloading of the material, the strain energy has a residual value

$$\psi(1,1,\eta_m) = \eta_m\, \bar{\psi}(1,1) + \phi(\eta_m) = 0 + \phi(\eta_m) = \phi(\eta_m) \tag{67}$$

This is known as the damage energy as mentioned earlier and is given by the area between the loading and the unloading curves. The damage energy may be interpreted as a measure of how much softening takes place in the material. The more the material is stressed and unloaded, more is the damage energy that is dissipated in the material. In other words, more the amount of damage energy that has been dissipated in the material, softer will be the response of the material on reloading.

2.12 FINITE ELEMENT ANALYSIS

The Principle of Virtual Work described in equation (40) is a partial differential equation in time and space since the strain contains gradients of the displacement field in space and the acceleration is a second derivative of the displacement field in time.(the force field can also be time dependent). Analytical methods to solve this equation are highly complex for complicated geometries and therefore numerical techniques are used to approximate the solution. The finite element method (FEM) is one such numerical method to discretize the space into nodes connected via elements. The POVW is satisfied on an elemental level in this method. The POVW equation after discretization in space becomes an ordinary differential equation in time. These ODE's can then be solved using time stepping schemes which will be discussed later.

The discretization at the element level is given by

$$\mathbf{u}\,(x,t) = N_i(x)u_i(t) \tag{68}$$

where the index i implies summation over all the nodes contained in the element. The quantities u_i are the value of the displacement field at the nodal locations i, and the N_i represent shape functions which are used to interpolate the displacement $\mathbf{u}(x)$ in the element using the nodal values at a given time. Note that $\mathbf{u}(x)$ implies $\mathbf{u}(x,y,z)$ at a given time and the spatial variation in all the directions has been represented using x.

In the Finite Element Method, the shape functions have an important property of dirac delta which implies that $u(x = x_i) = u_i$ since $N_i(x = x_j) = \delta_{ij}$.

The virtual displacement field is a test function that can be interpreted as a permissible perturbation conforming to the prescribed boundary conditions. The virtual displacement

in the Galerkin finite element method is also interpolated using the same the same shape functions such that,

$$\delta\mathbf{u}(x,t) = N_i(x)\,\delta u_i(t) \tag{69}$$

The gradient of the displacement field on discretization is given by,

$$\nabla\mathbf{u} = \nabla N_i(x)\,u_i(t) \tag{70}$$

Therefore the Green Strain can be given as

$$E = \frac{1}{2}\left(\nabla\mathbf{u} + \nabla^T\mathbf{u} + \nabla^T\mathbf{u}\nabla\mathbf{u}\right);\ \ \delta E = \frac{1}{2}\left(\nabla\delta\mathbf{u} + \nabla^T\delta\mathbf{u} + \nabla^T\delta\mathbf{u}\nabla\mathbf{u} + \ \nabla^T\mathbf{u}\nabla\delta\mathbf{u}\right); \tag{71}$$

$$\therefore E_{ij} = \frac{1}{2}\left(\mathbf{u}_{i,j} + \mathbf{u}_{j,i} + \mathbf{u}_{k,i}\mathbf{u}_{k,j}\right);\ \delta E_{ij} = \frac{1}{2}\left(\delta\mathbf{u}_{i,j} + \delta\mathbf{u}_{j,i} + \mathbf{u}_{k,i}\delta\mathbf{u}_{k,j} + \ \mathbf{u}_{k,j}\delta\mathbf{u}_{k,i}\right) \tag{72}$$

In matrix form, the variation in green strain and the second PK stress can be expressed as

$$\{\delta E\} = [B]\{\delta u\};\ \ \{S\} = \{S_{11}, S_{22}, S_{33}, S_{12}, S_{13}, S_{23}\}^T \tag{73}$$

where B is a matrix representing the spatial derivatives of the shape functions N

On substituting these quantities into the virtual work equation (40),

$$\begin{aligned}&\int S{:}\,\delta E\, dV_0 + \int \rho_0\ddot{\mathbf{u}}.\,\delta\mathbf{u}\, dV_0 - \int \rho_0\mathbf{b}.\,\delta\mathbf{u}\ dV_0 - \int \mathbf{t}.\,\delta\mathbf{u}\, dA_0 = \ \ 0, \text{ becomes}\\ &\int \{\delta u\}^T[B]^T\{S\}\, dV_0 + \int \rho_0\{\delta u\}^T\{N\}^T\{N\}\{\ddot{u}\}dV_0 - \int \{\delta u\}^T\{N\}^T\{b\}\rho_0 dV_0\\ &\qquad - \int \{\delta u\}^T\{N\}^T\{t\}dA_0 = 0\end{aligned} \tag{74}$$

Since the variation, δu is arbitrary, the equation reduces to

$$\{F_{int}\} + [M]\{\ddot{u}\} - \{F_{ext}\} = 0\ ; \text{where} \tag{75}$$

$$\{F_{int}\} = \int [B]^T\{S\}dV_0;\ [M] = \int \rho_0\{N\}^T\{N\}dV_0;\ \{F_{ext}\} = \int \{N\}^T\{b\}\rho_0 dV_0 + \int \{N\}^T\{t\}dA_0$$

The above equation (75) is the final equation of motion to solve. It is an ordinary differential equation in time and can be solved using implicit and explicit methods. The key difference between the two methods is as follows,

The implicit methods solve for the solution variable (u or $\ddot{u}$ in this case) at time t_{n+1} which is the next time step based on the equation of motion at t_{n+1} such that,

$$\{F_{int}\}^{n+1} + [M]\{\ddot{u}^{n+1}\} - \{F_{ext}\}^{n+1} = 0 \tag{76}$$

However, the explicit finite element methods use the equation of motion at the current time step t_n to solve for the solution variable at the next time step t_{n+1}

Implicit finite element methods like Newmark or generalized alpha schemes apply the Newton-Raphson scheme to the above equations and solve iteratively by defining the residual R such that

$$R^{n+1}(u^{n+1}) = \{F_{int}\}^{n+1} + [M]\{\ddot{u}^{n+1}\} - \{F_{ext}\}^{n+1} \tag{77}$$

$$R^{n+1}(u^{n+1} + \Delta u^{n+1}) \cong R^{n+1}(u^{n+1}) + \frac{\partial R^{n+1}(u^{n+1})}{\partial u}.\Delta u^{n+1} = 0 \tag{78}$$

$$\therefore \frac{\partial R^{n+1}(u^{n+1})}{\partial u^{n+1}}.\Delta\, u^{n+1} \cong\ -R(u^{n+1}) \tag{79}$$

$$\therefore J^{n+1}.\Delta u^{n+1} = -R(u^{n+1}) \tag{80}$$

where, $J^{n+1} = \frac{\partial R^{n+1}(u^{n+1})}{\partial u^{n+1}} = \frac{\partial F_{int}^{n+1}}{\partial u^{n+1}} + \frac{\partial(M\ddot{u}^{n+1})}{\partial u^{n+1}} - \frac{\partial F_{ext}^{n+1}}{\partial u^{n+1}},$ (81)

is called the Jacobian

the first part of the Jacobian is composed of the linearized stiffness matrix, the second part contains the mass matrix along with some constants based on the time stepping scheme used and the third part is made up of the stiffness contribution from spatially varying load. The calculation of the Jacobian matrix is one of the most time consuming aspects of the implicit methods. The Δu is calculated for every iteration and updated until a specified error condition is met such that the absolute or relative residual error is smaller than the tolerance. Implicit methods are based on a predictor corrector algorithm where the initial guess (usually based on an explicit method) is used to calculate the residual and once the converged displacement is obtained, the initial guesses for displacement velocity and acceleration are updated. An iterative scheme like the Newton-Raphson is therefore employed at every time-step. Depending on the type of Newton-Raphson procedure, the Jacobian is updated at every iteration or at selected iterations.

In the explicit methods like the central difference method, the jacobian is not calculated; therefore the stiffness matrix need not be evaluated at all. The mass matrix M is lumped (diagonalized) to \[M]\ so that the linear system of equations is reduced to an uncoupled system of equations which can be directly solved.

$$\backslash[M]\backslash\ddot{u}^{n+1} = \{F_{ext}\}^{n} - \{F_{int}\}^{n} \tag{82}$$

Once the acceleration at the next time step is obtained, the displacement and velocity are updated and used to calculate the internal force for the next time-step. Since the internal

stiffness matrix is not constructed, and the mass matrix is diagonalized, the explicit methods are fast at solving for the solution variable at a given time-step. Explicit methods however are conditionally stable so a time increment lesser than the critical time-step needs to be used. The critical time step is based on the highest frequency of the system and can be estimated from the dilatational wave speed in the material,

$$\Delta t \leq \frac{2}{\omega_{max}} \approx \frac{\min(L_{elem})}{c_d};\ \text{where}\ c_d = \sqrt{\frac{\lambda + 2\mu}{\rho}} \tag{83}$$

c_d is the dilatational speed based on Lamé constants λ and μ and the density of the material ρ. As the critical time step depends on the smallest element size, as the mesh gets finer, the critical time-step and thus the time-step used gets smaller. The time step size in explicit methods is usually much smaller than that used in implicit methods.

3. LITERATURE REVIEW

This literature review provides a brief overview of the articles that have been referred to during the creating of this thesis. It gives an account of the current or previous experimental and modelling techniques and results that are relevant to the scope of this thesis.

3.1 MATERIAL PROPERTIES OF THE HUMAN ATHEROSCLEROTIC PLAQUE

Loree et al [1] performed tensile tests on dog-boned specimens of plaques from human abdominal and thoracic aorta in the circumferential direction. The specimens were classified as Cellular, Hypo-cellular and calcified in nature and their respective stress-strain responses were recorded and a circumferential tangent modulus of elasticity was determined. A significant amount of variability was observed within the responses of the specimens tested. It was concluded that inter patient variability may be an important reason for the results.

Pericevic et al [2] used the material data from Loree et al to fit a third order polynomial strain energy density function to each of the three different plaque types. The plaque types were differentiated using the same classifications as in Loree et al as Cellular, Hypo-cellular and Calcified. A one eighth symmetry Finite Element model was created to simulate the response of the lesion characterized by different plaque types. The model therefore had a concentric plaque around the lumen due to symmetry conditions. It was concluded that the plaque morphology had a significant impact on the level of stresses induced in the arterial wall. The calcified plaque seemed to play a protective role therefore reducing the stresses in the arterial wall. However at a given pressure, the increase in vessel lumen was much lesser, in case of calcified plaque compared to the other plaque types.

Maher et al in 2009 [3] studied the compressive and tensile response of fresh human carotid plaques. The plaques were classified as echolucent (soft), mixed and calcified. The study showed that the calcified plaque had the stiffest behavior compared to the other classifications. A general second order Polynomial Hyperelastic strain energy density

function was used to fit parameters to the material response in tension as well as in compression.

Ebenstein et al [4] conducted nanoindentation tests on fibrous tissue, partially calcified fibrous tissue and on bulk calcifications from human plaque tissues. Carotid bifurcation plaques were used in the study. The stress response of the calcified has been reported to be much higher than those found in the tests by Loree et al [1]. These observations have been attributed to the differences in bulk vs local behavior.

Lawlor et al [5] performed uniaxial tensile testing on fresh carotid plaques that were excised using the endarterectomy procedure (surgical removal of plaque from arteries) from 14 patients. The plaques were classified as Hard, Mixed and Soft plaques. A Yeoh material strain energy density function was fit to the material responses and material parameters were documented. The ultimate tensile stress and ultimate tensile strains for these specimens were also reported. It was found that the average ultimate tensile stress for the samples was 366.6 ± 220.5 kPa and the ultimate tensile strain was 0.49 ± 0.088.

Maher et al in 2011, [6] studied the inelasticity of the human carotid plaques through cyclic loading of radial compressive specimens. The inelasticity included the softening of the plaque and residual strains. A constitutive model was proposed that incorporated the inelastic effects of softening and permanent set. The plaque was again classified as echolucent, mixed and calcified plaque. The softening curves were presented using material parameters to the proposed constitutive model. These curves have been used in this thesis to describe plaque behavior in the compressive regime and will be discussed in detail in Chapter 4.

3.2 MATERIAL PROPERTIES OF THE HUMAN ARTERY

Traditionally Human artery was modelled as a single layered, linear elastic, isotropic/ orthotropic material model [7] [8] [9]. However, these models are unable to capture the response of the tissue at supra-physiological loading conditions. The individual layers of

the artery have been shown to have separate responses and are highly nonlinear in nature. In addition it has also been shown that these tissue layers have different responses in different directions, which implies that the response is anisotropic in nature [10]. Therefore the literature review on this matter will largely focus on recent experimental data that treat the arterial tissue as an anisotropic nonlinear material.

Lally et al, in 2001 [11], performed uniaxial and biaxial loading tests on porcine aorta and human femoral artery. The stress strain response of the tissues was fit to a 5 parameter Mooney-Rivlin Model. This isotropic material model was then used to model stent-artery interaction in order to analyze the prolapse due to stent implantation. Radial deflection was observed for 4 different stent stent types under a pressure of 450 mm Hg. The peak stress in the vascular wall was used as a measure to compare the potential for restenosis from the different stent types.

Holzapfel et al [10], 2005 performed cyclic quasi static uniaxial tests on 13 nonstentotic human left anterior coronary arteries. Tests were performed on tensile specimens from the circumferential direction and the axial direction. Ultimate tensile stresses of the all arterial layers were determined. It was observed that the intima was the stiffest layer in samples studied. The experimental curves were then used to fit parameters to the popular HGO model that was discussed earlier. Small hysteresis was found in unloading and loading branches of all arteries.

Gultova et al [12] performed uniaxial cyclic loading tests on human aorta tissue to characterize the tissue for Mullin's effect. Four loading and unloading cycles to the same stretch level were performed for each sample in the circumferential and axial direction. An anisotropic form of softening variable was used to describe the Mullin's effect in this study. It was concluded that under cyclic loading conditions, large strain induced softening occurs in human thoracic aorta.

Horny et al [13] performed a similar study in 2010 with cyclic loading on uniaxial tensile test samples of the human aorta to describe Mullin's effect softening. They observed significant softening and residual strains during cyclic loading and unloading of the aorta tissue.

Weisbecker et al [14] performed uniaxial cyclic loading tests on individual layers of the human thoracic and abdominal aorta. A novel pseudo elastic damage model is used to describe the discontinuous softening in the tissue. The effect of preconditioning before testing was also studied. It was concluded that preconditioning above the physiological loading conditions may alter the material properties since the material would undergo softening at supraphysiological loading conditions. The material and damage parameters presented in this study have been used for modelling the arterial layers in the analysis covered in the current thesis and will be discussed in detail in Chapter 4.

3.3 DAMAGE MODELLING THEORIES

Soft tissues undergo cyclic softening behavior as seen in various studies such as the ones by Maher et al [6], Horney et al [13], Gultova et al [12], Weisbecker et al [14]. This softening can be characterized using different damage models. One of the more important and fundamental theories was developed by Ogden and Roxburgh [15] to explain the Mullin's effect which is a softening phenomenon in filled elastomers. The details and formulation of the softening phenomenon was discussed in the previous chapter. This model and its variants were then adopted by other researchers to characterize response of biological tissues. There are two general schools of thought in these models, known as the discontinuous and the continuous type damage models. The fundamentals of some of these theories are outlined in this section.

Mullins in 1947 observed a softening phenomenon when cyclic loading on rubber specimens was performed [16]. This has been widely known as Mullins effect. As stated above, the formulation by Ogden and Roxburgh [15] was one of the first models to successfully predict the behavior of filled rubber using a pseudo-elastic material model. This model is a discontinuous type damage model, which means that the damage in the sample occurs only after the previously loaded state is surpassed. Ogden and Roxburgh note that it is the maximum energy state attained in the loading history that governs the response of the material on further loading or unloading.

Balzani et al in 2004 [17] introduced an anisotropic damage model of the discontinuous type and applied it to a fiber direction based primary hyperelastic function. Only the fiber

component of the strain energy density function was scaled by a damage factor and the isotropic matrix component has been unaltered.

$$\psi\,(C, M_i, D_i) = \bar{\psi}(C) + \sum_{i=1}^{2}[(1 - D_i)\psi_i^0(C, M_i)] \quad ; \text{where } M_i = a_i \otimes a_i \tag{1}$$

Where a_i are the structural direction vectors. The damage variable D was defined as

$$D_i(\psi_i^0) = \gamma_1\left(1 - e^{-\frac{\beta_i}{\gamma_2}}\right) \text{ where } \beta_i = \sup_{0\le s\le t}[\psi_i^0(C, M_i, s)] \tag{2}$$

Such that $\psi_i^0(1, M_i, 0) = 0$ to specify discontinuous damage effect. The parameters γ_1, γ_2 are material constants. It was noted that the damage is motivated by breakage of collagen cross-links. A numerical example was provided demonstrating the implementation of the material model.

Balzani et al in 2006, [18] note that arterial walls undergo reduction in stiffness during angioplasty due to the overstretching mechanism of PTA. They provide an anisotropic damage model to reflect the damage mechanism during angioplasty. Damage is only applied to the fiber component since the assumption was that damage occurs due to rupture of cross-bridges between collageneous micro-fibrils. A mechanism for incorporating the residual arterial stresses is also presented in this study. Balzani et al in 2013 [19] provided a comparison of different damage functions required for the soft tissue damage approach with smooth and non-smooth tangent moduli models and investigated the numerical difficulties with the same.

As discussed earlier, Maher et al in 2011 [6] performed cyclic compression tests on human atherosclerotic plaques and fit a discontinuous type damage evolution function to describe the softening in the material. The damage variable D was given by

$$D = \zeta_\infty\left(1 - e^{\frac{(\psi_{IL}(C) - \alpha(t))}{i}}\right) \tag{3}$$

Where ζ_∞, i are material constants and ψ_{IL}, α are the values of the SEDF in the current state and the maximum loaded state in the history of deformation respectively. The damage variable D was incorporated in the stress softening by scaling the stress by a factor of $(1 - D)$ similar to the approach seen in Balzani et al 2004. [17]

Weisbecker et al [14] as stated earlier, fit a discontinuous type pseudo-elastic damage model to the cyclic loading experiments on human arterial tissue. The damage function was applied to the collageneous and matrix components and it was noted that the damage in the matrix components is quite insignificant in comparison. The model formulation will be discussed in the material modelling section of the thesis.

Gultova et al [12] also fit a discontinuous type pseudo-elastic damage model to cyclic loading results of human aorta. The pseudo-energy function used was that of the limiting fiber extensibility form. The damage variable η is a modification of the Mullin's effect form by Ogden and Roxburgh [15], and is given by

$$\eta = 1 - \frac{1}{r}\left(\mathrm{erf}\left(\frac{W_m - W_0}{k}\right)\right) \tag{4}$$

Where the parameter k is in the form that would incorporate material anisotropy as opposed to the traditional Mullin's effect.

Calvo et al in 2006 [20] presented a continuous type large strain damage model for fibrous tissue. The difference between continuous type and discontinuous type damage is that in the latter, damage can take place only once the maximum energy during the loading history has been surpassed. As long as the material is loaded to a lower energy state than previously achieved, discontinuous damage model states that there will be no further damage. This is in contrast to the continuous type damage model where damage model takes the entire loading history into account. Calvo et al [20] state that non-physiological loads drive the soft tissue to damage that arises from two possible mechanisms. One is the tearing or plasticity of fibers and the other is the biochemical degradation of the extracellular matrix from protease release associated with cellular necrosis. Therefore a structural damage model with damage process for the matrix as well as for the fibers was proposed. The damage variables for the collagenous part and the matrix part $D_f and\ D_m$ are used in the equation below to simulate softening response.

$$\psi\left(C, M, N, D_m, D_f\right) = \psi_{vol}(J) + (1 - D_m)\bar{\psi}_o^m(\bar{C}) + \left(1 - D_f\right)\bar{\psi}_0^f(\bar{C}, M, N) \tag{5}$$

Where symbols have their usual meanings and M and N are structural tensors related to the fiber directions. The evolution of the damage variable was given by,

$$\Xi_s^m = \sqrt{2\bar{\psi}_0^m\left(\bar{C}(s)\right)} \quad \text{and } \Xi_s^f = \sqrt{2\bar{\psi}_0^f\left(\bar{C}(s)\right)} \tag{6}$$

Where $\bar{C}(s)$ is the modified Cauchy green deformation tensor at a given time *s*. w=With $\Xi_t^m \; and \; \Xi_t^f$ being the maximum values of the respective functions over the history of loading until time t, a damage criterion $\phi_m(C(t), \Xi_t^m)$ was defined as a function of the current value of Ξ_s^m and the maximum value Ξ_t^m for the matrix component. The evolution of the damage variable was then specified as

$$\frac{dD_m}{dt} = \begin{cases} \bar{h}(\Xi^m, D_m)\dot{\Xi}^m & if\ \phi = 0 \ \text{ and } \frac{\partial \phi_m}{\partial C} : \dot{C} > 0 \quad (7) \\ 0 & \text{otherwise} \quad (8) \end{cases}$$

where $\bar{h}$ is a given function that characterizes damage evolution in the material. Similarly a damage evolution of the collagen fibers was also specified. Calvo et al [20] also simulated the response of the arterial tissue in balloon angioplasty to demonstrate the effect of supra-physiological loading conditions on the behavior of the tissue under internal pressure loading post angioplasty. It was observed that the arterial wall had a softer response after angioplasty due to the damage induced during the process.

Pena et al in 2008 [21] performed a comparative study between the continuous damage model and the discontinuous Mullin's type damage model. A mixed model was also introduced as a combination of the two types of damage theories. Comparison with experimental results on uniaxial tests on pig arteries was made. It was concluded that the mixed model performed better than both the discontinuous and continuous type damage models. The discontinuous type damage model was able to capture the Mullin's type effect but not the hysteretic behavior, whereas the continuous type model was able to capture the hysteretic behavior but not the Mullin's effect.

3.4 PREVIOUS COMPUTATIONAL STUDIES OF BALLOON ANGIOPLASTY

Balloon angioplasty and its effects on the arterial wall have been of great interest to researchers. A significant portion of this thesis covers the analysis of the procedure. Some of the studies involving balloon angioplasty with and without stenting have been discussed below.

The folded angioplasty balloon model commonly used in simulations was first introduced by Laroche et al [22] in 2006. The study provided a mathematical formulation of radial and circumferential position of the surface of a balloon in the folded state as a function of number of folded flaps, the initial internal radius, the initial external radius and the final radius of the expanded balloon. The same model was adopted by other researchers like Martin et al [23] in 2013 and Conway et al in 2014 [24]. Martin et al [23] studied the effect of the model of a semi-compliant angioplasty balloon on the deployment of stent. Three increasingly complex balloon configurations were used in the study and it was concluded that the balloon configuration has a substantial influence on the transient response of the stent and on its impact on mechanical environment of the coronary artery.

Holzapfel et al in 2002 [25] conducted a numerical study using Finite Element Analysis of balloon angioplasty and stenting of human iliac arteries. The artery was modelled as diseased and non-diseased media, adventitia, and intima composed of non-diseased intima, collagenous cap, lipid pool fibrotic plaque and calcification. The geometric model of individual layers was derived from an MRI scan. The individual layers were modelled as HGO type models with fiber orientations and the non-diseased intima and media models included plasticity. The balloon and stent expansions were simulated using displacement boundary conditions. Simulations using axial pre-stretch (reference simulation), without axial pre-stretch, plane strain approximation and isotropy were performed and compared. It was concluded that these simplified models may lead to significant erroneous deviations of stress states from the reference simulation.

Gasser and Holzapfel in 2005 [26] performed a computational study on arterial response to balloon angioplasty using Finite element Analysis. The study states that the primary mechanism of angioplasty being overstretching of the nondiseased arterial wall, the motivation for the study was therefore to investigate the deformation and stress evolutions along with the overstretch of the vessel due to a Gruntzig-type balloon catheter. The artery was modelled as adventitia, media and plaque. Residual stresses were considered in modelling the layers of the artery using the opened-up configuration. The material model for the layers of the artery was of the HGO type with fiber distribution and inelastic effects were considered for the media. Fibrous components of the plaque

and the intimal layer were neglected and the plaque was modelled as a rigid calcified layer. The observations from the study were that an increase in the lumen size along with weakening of the response under internal pressure is expected post angioplasty. The study suggests that the commonly used plane strain condition for arterial models would be inappropriate. The dominating stresses in the media and adventitia were found to be in the circumferential and axial directions respectively. It was claimed that the balloon induced mechanical changes in the arterial wall might be responsible for the development of smooth muscle cell proliferation, neointimal hyperplasia and refractory restenosis.

Conway et al [24], [27] studied the effect of different type of stent designs as an impact on the overall lumen gain as well as tissue damage risk assessment for individual layers of arteries including plaque tissue. The artery was modelled as equally thick layers of the arterial wall made up of intima, media and adventitia of the HGO type material. Different plaque material models were considered and results were presented for each model. Tissue damage risk was defined as the percentage of elements experiencing stress levels above the ultimate tensile stress values of the layer. This study was motivated by a need to investigate the influence of radius of curvature of the vessel along the length for coronary applications. It was concluded that the implantation behavior is not significantly affected for severely curved vessels. It was also observed that increasing the percentage stenosis increased the tissue damage risk value.

3.5 ISSUES ASSOCIATED WITH BALLOON ANGIOPLASTY

Grassman et al [35] in 1997 reported that in their study through 1990-1994, 4366 coronary percutaneous transluminal angioplasties were performed to treat myocardial infarction. The overall success rate of the procedure was found to be 91.5% with an in-hospital mortality rate of 2.5% and that of emergency surgery procedure to be 4.3%. However the secondary success rate of angioplasty has been seen to be lower. Levine et al [36] in 1994 reported that the percentage of clinical restenosis found in several studies on coronary angioplasty has been 36-40%. Most patients that develop restenosis are seen to show symptoms within 3 months of the procedure. Often repeat angioplasty is used as the treatment to restenosis although even bypass surgery or medical therapy might be possible alternatives. The use of stents has become a common practice for treating

coronary occlusions because the secondary success rate of stenting has been seen to be higher than just PTA.

Coronary stenting without prior balloon dilatation is known as direct stenting. IJsselmuiden et al [37] studied the in-stent restenosis rate of direct stenting and stenting accompanied by PTA. The primary success rate was seen to be as high as 98.3 % for direct stenting and 97.8% for stenting with predilitation. However the restenosis rate at 6 months was observed to be 23.1% for the former and 18.8% percent for the latter.

E.Faglia et al [38] in 2005 stated that PTA is also the first choice for revascularization in diabetic eschemic foot. In their study, PTA was performed in 993 diabetic patients that suffered from critical limb ischemia from 1999 to 2003. The restenosis rate in the study was found to be 11.3% with infrequent complications and low mortality rate. Ferraresi et al [39] in 2008 carried out a study on 101 diabetic patients with 107 critically ischemic limbs and PTA was performed on isolated below-the knee lesions. The results showed a high rate of limb salvage which was 93%, however after 1 year, 42% of the non-amputated limbs were reported to have restenosis.

Balloon angioplasty and stenting are often associated with injury to the vascular tissue. Lam et al [40] ,found that in porcine arteries post Angioplasty, dilated vessels without a Medial tear had much less platelet deposition and no evidence of thrombus formation at the site of endothelial loss. After deep arterial injury with a tear into the media, there is mobilization of factors promoting thrombus formation and destruction of factors inhibiting thrombus formation and promoting thrombus dissolution. Also, Cragg et al in [41], state that the injury during angioplasty is pronounced in the media.

Rogers et al [42] state that “although injury to the endothelial cells alone produces mild neointimal thickening, more substantial neointimal hyperplasia requires direct injury to medial smooth muscle cells” [43] [44]. In humans “higher inflation pressures and larger balloon sizes may also cause greater neointimal hyperplasia” [45] [46] [47]. It is interesting to note that higher inflation pressures and higher balloon sizes may contribute to higher peak stresses in the vessel. They also state that “acute luminal stretching during angioplasty is shown to be an accurate predictor of later luminal loss”. [48] [49] [50] [51]

Holzapfel and Gasser [26] state that the primary mechanism of balloon angioplasty is by (1) overstretching the non-diseased portion of the artery, (2) plaque disruption or dissection, (3) redistribution inside the arterial wall (4) lipid extrusion (if Lipid pools are present). Lumen enlargement by angioplasty has been shown to be primarily due to the stretching of the artery [52] [53] [54]. The plaque structure in case of collagenous caps did not change during radial compression whereas the nondiseased portion of the wall was stretched. Similar results were observed by numerical simulations by Holzapfel et al in [3,4]. During supraphysiological loading of vessels, the artery undergoes (1) a permanent deformation with increasing load and (2) tissue weakening/softening or damage that was discussed in the earlier section. Based on the studies [55] [56] [57] Gasser and Holzapfel [26]reported that the vascular injury that is seen during angioplasty in the dilated artery is especially pronounced in the media whereas inflation tests on adventitial layer show that the adventitia behaves nearly elastically with negligible material damage. Also, it was noted that balloon induced wall overstretch seems to be mainly due to the histostructural changes in the medial layer. Therefore the peak stresses induced in the artery especially in the media may be an important measure to predict the vessel damage and injury. [58]

3.6 PREVIOUS STUDIES ON ORBITAL ATHERECTOMY

There have been a limited number of computational studies of orbital Atherectomy. The experimental work that has been documented has been focused on patient and cadaver studies and a comparative assessment of orbital atherectomy when accompanied by balloon angioplasty versus standalone balloon angioplasty.

Lovik et al [28], performed cadaver and in-vitro experiments followed by numerical simulations to assess whether orbital atherectomy could cause thermal injury to the tissue. The experiments were performed in a graphite surrogate artery and a cadaver artery in order to get the temperature distributions measured by thermocouples. These temperature distributions were matched up by numerical simulations with different thicknesses of plaque insulation. The resulting temperatures in the simulations were used to assess a thermal injury index and it was concluded that it is highly unlikely that arteries suffer from thermal injury during orbital atherectomy.

Safian et al in 2009 [29] conducted a study on one hundred and twenty four patients suffering from chronic infrapopliteal arterial occlusive disease which is a common cause of critical limb ischemia and claudication. The study was carried out for a stenosis percentage greater than 50 percent with 12% lesions having total occlusions and 55% lesions being heavily calcified. The patients were monitored for 6 months post the procedure. Statistical results were presented at the end of the study. The results state that "The primary safety endpoint of major adverse events (MAE) at 30 days was observed in four patients. The primary efficacy endpoint was 17.8±13.5%. The secondary endpoints of procedural success and 6 month MAE were observed in 90.1 and 10.4 % of the patients respectively". It was concluded that Oribital atherectomy provides a predictable and safe lumen enlargement option for infrapopliteal disease. Short term data indicated infrequent need for revascularization or amputation.

Shammas et al in 2012 [30] studied the role of orbital atherectomy (OA) and balloon angioplasty (BA) versus standalone balloon angioplasty (BA) in patients with critical limb ischemia. Fifty patients were enrolled in the study and 25 each were treated with OA +BA and only BA. The average balloon expansion pressures for the OA +BA arm was 5.9 ± 4.2 atm versus 9.4± 3.8 atm for standalone BA. In the OA +BA category, the procedural success was found to be 93.1% as opposed to BA alone which was 82.4%. Bailout stenting was required in 2 of 29 lesions in OA +BA and in 5 of 35 lesions in BA alone. One patient that underwent the OA procedure experienced a type D dissection due to accidental pull back of the OA device guidewire. In the BA category 6 patients experienced a dissection of types A, B, D and F. It was concluded that since OA + BA needed statistically significant balloon pressures and resulted in lesser dissections than standalone BA, OA increases the chances of reaching a desirable outcome of angioplasty.

Dattilo et al [31] conducted a similar study in 2014 to test the hypothesis that OA improves the lesion compliance. 50 patients were enrolled with calcified femoropopliteal disease. Since BA for calcified lesions in FP disease is associated with increased dissection rates, the objective of this study was to compare the results of OA + BA vs standalone BA. It was seen that the mean maximum balloon pressures in OA +BA was 4 atm as compared to 9.1 atm in BA alone. Therefore it was concluded that OA + BA

yields better luminal gain by improving lesion compliance and decreasing stenting for femoropopliteal disease.

4. MATERIAL MODELLING AND VERIFICATION

In numerical analysis, obtaining a good material mode that accurately represents the experimental data and is stable in the range of operation is of paramount importance. Some material data fits provide good accuracy but lack model stability and some provide a good stability especially in case of unconditionally stable models but might lack accuracy to the experimental data. Therefore obtaining a material model fit with both accuracy and stability is worth investigating. Based on the some of the experimental results discussed in the literature review section, material data has been selected for the scope of this thesis. The details of the same are covered in this chapter.

4.1 MATERIAL STABILITY ACCORDING TO DRUCKER CRITERION

In order for a hyperelastic material model to be stable, it must satisfy a stability condition known as the Drucker stability criterion [32]. A requirement of elastic materials is to have a positive definite tangential material stiffness matrix. Drucker stability criterion for an incompressible material requires that an infinitesimal change in stress $d\sigma$ following from an infinitesimal increase in strain $d\epsilon$ satisfies the inequality [33],

$$d\sigma : d\epsilon > 0 \tag{1}$$

And at a given strain level, $d\sigma_{ij} = C_{ijkl} d\epsilon_{kl}$ makes the above equation,

$$d\epsilon_{ij} C_{ijkl} d\epsilon_{kl} > 0 \tag{2}$$

, therefore requiring the tangent material stiffness to be positive definite. [33]. Abaqus checks the stability of the material model in the Drucker sense for the first three deformation modes; uniaxial tension and compression, biaxial tension and compression and planar tension and compression. If the material model is not stable in the Drucker sense within the strain range of operation, the material results may be unstable and not unique. Therefore Drucker stability criterion is an important factor to be considered when performing any material data fit.

4.2 COMPUTATIONAL MODELLING OF ATHEROSCLEROTIC PLAQUE

Maher et al in 2011, [6] performed cyclic loading experiments on Atherosclerotic plaque to characterize the tissue softening over cyclic loading similar to soft materials like rubber. Plaque samples of Calcified, Echolucent and Mixed type were cut into compression test specimens. Cyclic compression tests were performed on the samples to yield stress strain responses. The stress-strain curves were then used to fit an elasto-plastic type discontinuous damage model. The model was similar to Mullins effect model however with a different form for the softening/damage parameter. The strain energy density function for the model is given below.

$$\sigma = (1 - D)(\sigma_{IL} - \sigma_{IN}), \text{ Where} \tag{3}$$

$$\sigma_{IL} = 2J^{-1}F\frac{\partial \psi_{IL}}{\partial C}F^{T} \quad \text{and} \tag{4}$$

$$\sigma_{IN} = 2J^{*-1}F^{*}\frac{\partial N}{\partial C^{*}}F^{*T} \tag{5}$$

F, J and C are the deformation gradient tensor, the Jacobian determinant and the right Cauchy Green Deformation Tensor respectively. F^{*}, J^{*} and C^{*} are the values of the deformation gradient tensor, the Jacobian determinant and the right Cauchy Green Deformation Tensor respectively calculated at the maximum loading during the deformation history.

$$\psi_{IL} = \psi_{IL}\big(I_1(C)\big) = \frac{a}{b}\left(\exp\left(\frac{b}{2}(I_1 - 3)\right) - 1\right) \qquad \text{and} \tag{6}$$

$$N = c^{*}(I_1^{*} - 3), \tag{7}$$

The softening parameter D is given by,

$$D = \zeta_{\infty}\left(1 - e^{\frac{(\psi_{IL}(C) - \alpha(t))}{i}}\right) \tag{8}$$

Where ζ_{∞} and i are material constants and $\alpha(t)$ is the maximum value of ψ_{IL} in the loading history. Since the material is initially loaded, $\alpha(t) = \psi_{IL}$ for all points until the material is unloaded for the first time. Therefore, D =0 for the first loading until unloading starts. D becomes 0 again once the maximum loading is surpassed and further loading takes place.

The parameter values documented for average calcified, echolucent and mixed plaques were used as characteristic values for the respective plaque types. A Matlab code was written for the material model and Nominal Stress vs Nominal Strain values were plotted for the 3 plaque types. The average values for the parameters of the different plaque types reported by Maher et al [6] are shown the table below

Plaque type	**a (KPa)**	**b**	**C*(KPa)**	**ζ∞**	**I**
Calcified	68.5 ± 49.49	1.99 ± 1.82	13.33 ± 10.04	0.864 ± 0.099	0.017 ± 0.013
Echolucent	12.18 ± 9.87	0.67 ± 0.37	2.44 ± 2.32	0.904 ± 0.034	0.008 ± 0.004
Mixed	47.93 ± 44.38	1.05 ± 1.37	8.81 ± 8.81	0.771 ± 0.321	0.014 ± 0.008

Table 4.1 Material parameters for Average response of Calcified, Echolucent and Mixed plaque reported by Maher et al [6]

The experimental fit material model for the different types of plaques is shown below.

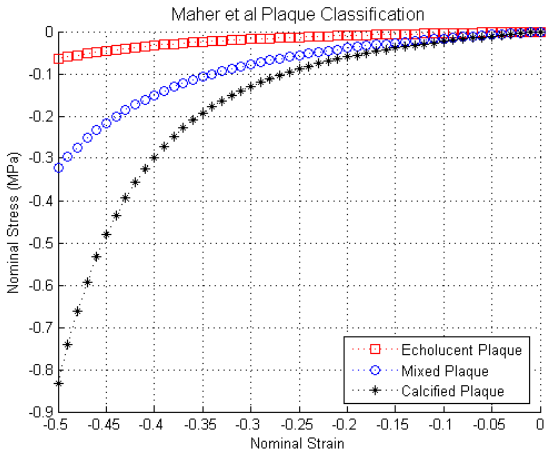

Figure 4.1: *Experimental primary hyperelastic response of Calcified, Echolucent and Mixed plaque types reported by Maher et al* [6]

It can be seen above that the calcified plaque is much stiffer than the echolucent (soft) plaque, as would be expected. The mixed plaque has an intermediate response as compared to the other two plaque types. The plots generated from this data were then used to fit a 3rd order Ogden Primary Hyperelastic curve in order to fit the Mullin's damage parameters; r, m and β. In order to get an accurate fit for damage parameters, the

permanent set generated from the data plots was neglected for the data fit and then included directly into Abaqus as permanent set values.

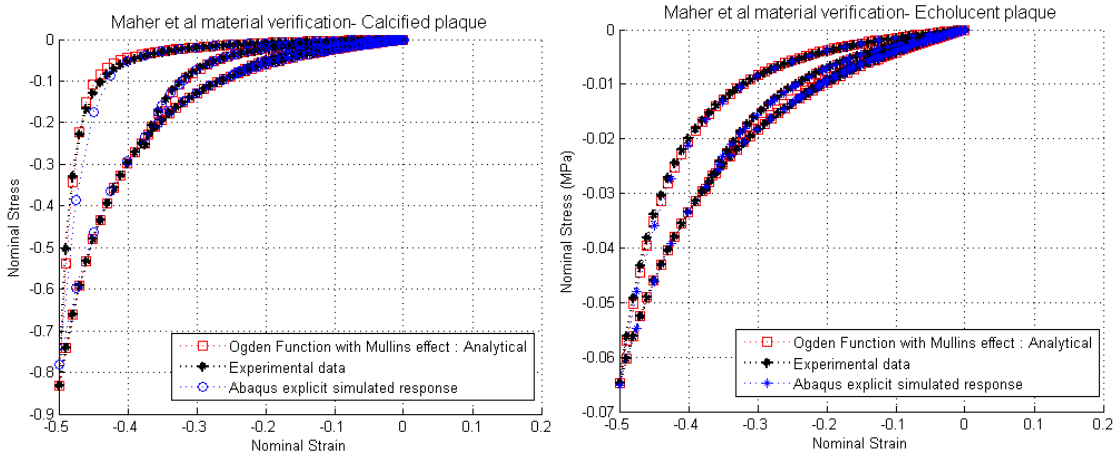

Figure 4.2: *Experimental results from Maher et al* [6] *fitted to a 3rd order Ogden Function with Mullins effect*

The third order Ogden function fit to the compressive data by Maher et al [6] seems to match up perfectly with the experimental results. However, if extended into the tensile regime, the data seems to be extremely soft as shown in the figure below.

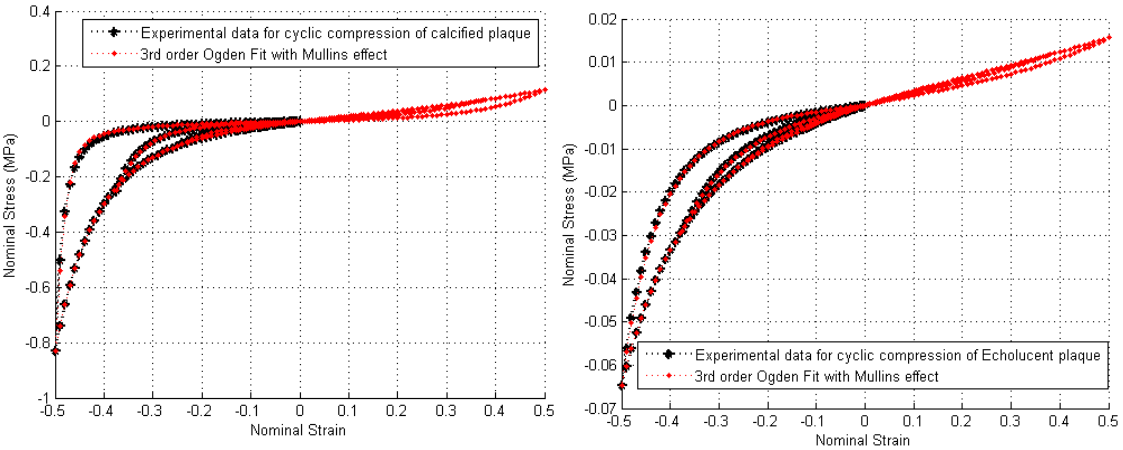

Figure 4.3: *Ogden models with Mullins effect fit to compressive data from Maher et al* [6] *extended into the tensile regime*

Therefore the Ogden fit generated above would work only if the strains observed in the simulation are compressive. However this is not the case, since the strains during Atherectomy and Angioplasty observed during a test simulation revealed that both the plaque components are primarily in compression during Atherectomy but are in tension

during Angioplasty. Therefore the model mentioned above alone would not be able to capture the physical process, especially during Balloon Angioplasty.

Lawlor et al [5] in 2011 conducted uniaxial tensile loading tests on fresh human carotid plaques that were excised by the endarterectomy procedure. The response of the plaques was then fit on to a Yeoh strain energy density function as given below,

$$\psi\,(I_1) = \sum_{i=1}^{3} C_{i0}(I_1 - 3)^i \tag{9}$$

The material parameters $C_{10}, C_{20}\ and\ C_{30}$ were reported for the different plaque samples. An average for the three plaque types (hard, soft and mixed plaques) was also reported. The plots for the three different plaque types have been shown below.

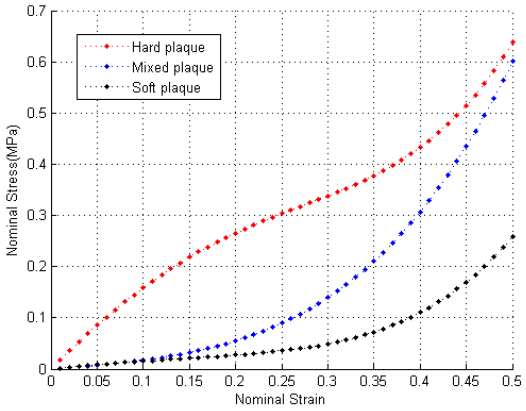

Figure 4.4: *Material data reported by* [5] *for average representative hard, mixed and soft plaques*

The average value of soft plaque response in tension was used in this thesis to model the response of the echolucent or soft plaque in tension. This model was chosen since the combination of the two curves gave a material fit that satisfied the Drucker stability criterion and the slope at zero energy state for loading and unloading was consistent. The combined data has been shown below.

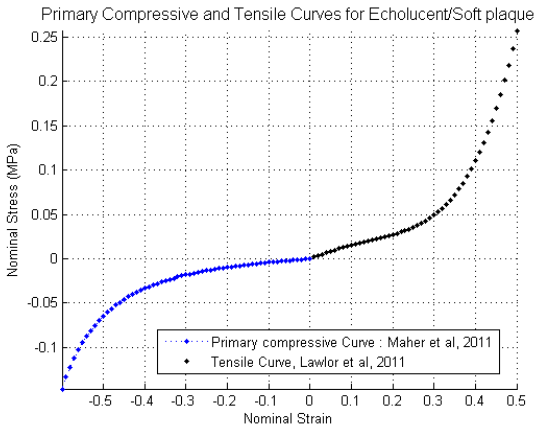

Figure 4.5: *Combined compressive and tensile material data for echolucent plaque*

For calcified plaque in the tensile regime, experimental data was derived from Maher et al [6] 2009 who performed uniaxial tensile and compressive loading tests on fresh carotid plaques. A second order Polynomial Hyperelastic strain energy density function was fit to the experimental data. The parameters were reported for the polynomial function for the compressive and tensile samples. A calcified plaque sample (11) in tension was used to describe the tensile properties of the calcified plaque. This sample was selected since it provided an accurate fit along with satisfying the Drucker stability criterion. The primary plaque response for calcified plaque in tension and compression has been shown below. Note that the curve fit in tension that was shown earlier in figure (4.3) for both calcified and soft plaque was much softer than can be seen in figures (4.5, 4.6) and therefore was not sufficient in describing the material response completely.

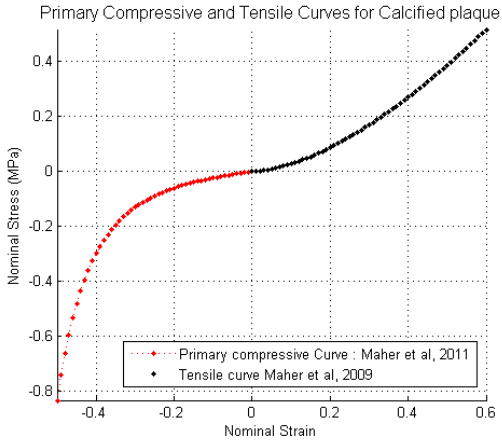

Figure 4.6: *Combined compressive and tensile material data for calcified plaque*

As stated earlier, the strains during orbital atherectomy test simulation were mainly compressive along with some locations experiencing tensile strains. Therefore the combined 3rd order Ogden function for the two kinds of plaques for atherectomy was fit in a way that provided good accuracy within the range of operation along with maintaining material stability. During balloon angioplasty test simulation, the strain observed in both plaque types was mainly tensile along with some amount of compression in the calcified layer. Therefore the 3rd order Ogden model that provided the best accuracy and stability within this strain range was found. The material fits for Balloon angioplasty and Atherectomy for the plaque types have been shown in figures (4.7, 4.8).

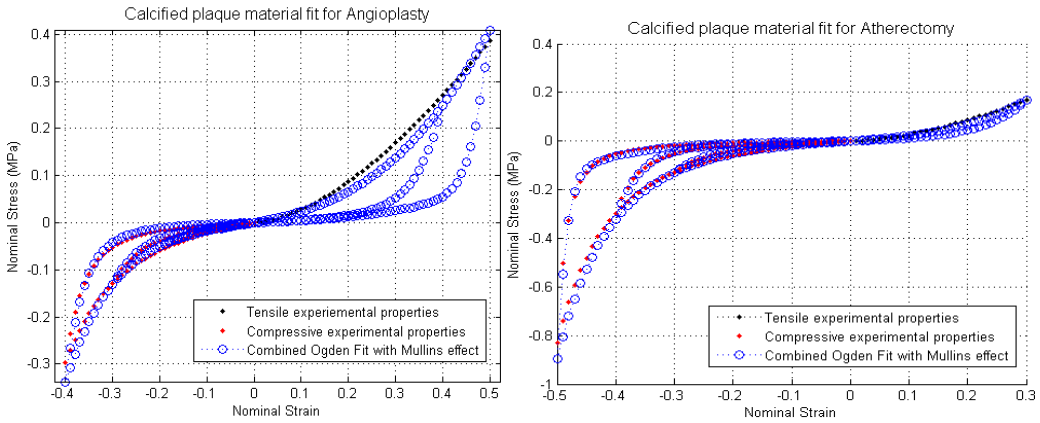

Figure 4.7: *Final material model of calcified plaque for angioplasty and orbital atherectomy simulations respectively*

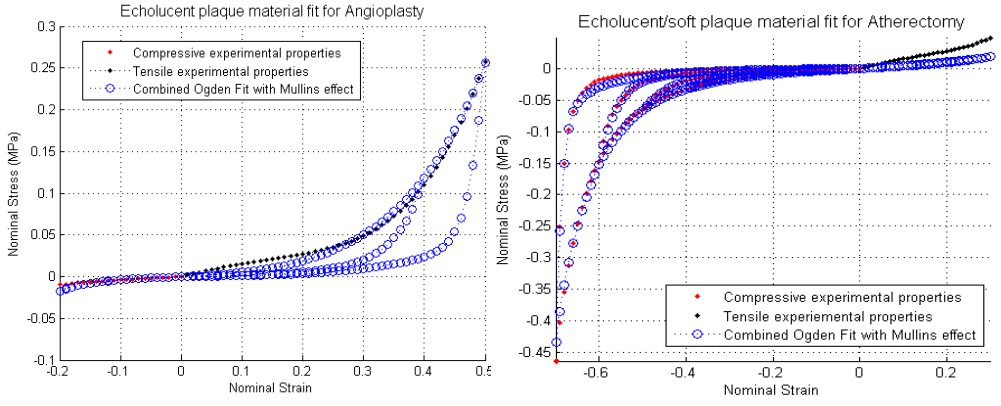

Figure 4.8: *Final material model of echolucent/soft plaque for angioplasty and orbital atherectomy simulations respectively*

In summary, the material fits were the best possible fits in the active strain ranges that satisfied Drucker stability criterion. Experimental data from Maher et al, 2011 [6] demonstrate the softening behavior of plaque tissue in cyclic loading. The cyclic loading data was available only for compressive tests. The damage parameters that have been fit to these tests have been extrapolated onto the tensile primary curves. According to Weisbecker et al [14], as will be seen in the following section, Horny et al [] and Gultova et al [], cyclic loading tests in tension on human arterial tissue showed softening curves similar to the results by Maher et al. Therefore the extrapolation of the damage parameters onto the tensile region was assumed to be justified for the scope of this thesis.

4.2.1 Compressibility

Most soft materials like biological tissues are modelled as incompressibile materials. The material fits obtained experimentally have also been modelled using incompressible hyperelastic strain energy density functions. [Maher et al, Lawlor]. In Abaqus Standard, totally incompressible or almost incompressible materials can be used. The incompressibilty constraint in such a situation is modelled using missed u-p formulations with Hybrid elements. In Hybrid elements, pressure degree of freedom is also added onto the displacement degrees of freedom since the displacement alone is insufficient to describe the response. According to Abaqus Analysis manual [33], almost or near incompressibile behavior must be simulated using hybrid elements. Also reduced integration must be used in such cases since fully integrated elements have a tendency to lock. In Abaqus Explicit, since hybrid elements are not available, some amount of compressibility must be provided to the material. The compressibility factor D in Abaqus is the ratio of the initial bulk modulus K_0 to the initial shear modulus μ_0. The Poisson's ratio of the material can be then defined as

$$\nu = \frac{3D-2}{6D+2}\ ; where\ D = \frac{K_0}{\mu_0} \tag{10}$$

According to Abaqus Manual, the default value of Poisson's ratio for incompressible materials in Abaqus Explicit is 0.475. Also, using a maximum Poisson's ratio of 0.495 or equivalently a D value of 100 or lesser is recommended since larger ratios introduce high

frequency noise into the dynamic solution and therefore require an excessively small time increment. However, from trial simulations it was observed that, a poisson's ratio of 0.495 for the soft plaque layer decreased the critical time step drastically. Therefore for all practical purposes, the Poisson's ratio for this layer was kept at the default value of 0.475. The Poisson's ratio for the calcified plaque layer was set to 0.495. Single element uniaxial compression simulation checks were performed to check the compressibility of the plaque types. It was found that the maximum compressibility at a compression of 0.6 strain level for echolucent plaque was 8.03% and for calcified plaque was 6.61 % which were considered acceptable since it was based on a balance of computational cost and accurate material representation.

4.3 COMPUTATIONAL MODELLING OF THE ARTERIAL WALL

Weisbecker et al [14] performed cyclic uniaxial tensile tests on individual layers of the abdominal and thoracic aorta in the circumferential and axial directions to determine the primary and cyclic behavior of the arteries. The Cauchy stress-stretch curves were then used to fit the Mullins effect parameters r,m and β. The typical behavior of an artery in the circumferential and axial directions is shown in the figure below.

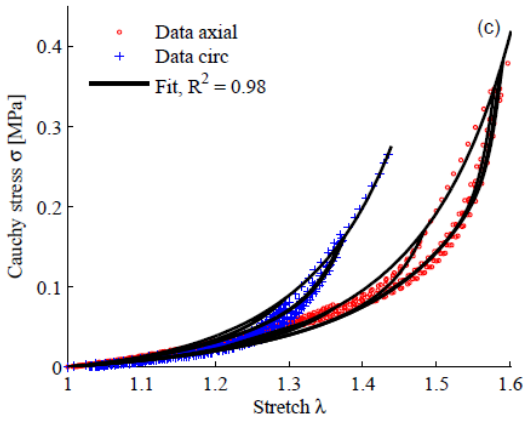

Figure 4.9: *Representative case of damage accumulation in Arterial Tissue as reported by Weisbecker et al* [14]

Weisbecker et al found the typical average values of the material properties for the media and adventitia. These values were used in the analyses performed in this thesis. The

material model used was that of the Holzapfel-Gasser Ogden (HGO) type which was discussed in the previous chapter with Mullin's effect.

$$\psi(J, \bar{C}, \eta) = \psi_{vol}(J) + \eta\, \psi^0(C) + \phi(\eta) \tag{11}$$

Where as stated in [14], ψ_{vol} is a strictly convex function that describes the volumetric elastic response, ψ^0 is the isochoric strain energy of the undamaged material and $\phi(\eta)$ is the damage function. Damage is only associated with deviatoric part of the strain energy density function.

$$\psi^0 = \psi^0_{matrix} + \psi^0_{fibers} \tag{12}$$

$$\psi^0_{matrix} = \frac{\mu}{2}(I_1 - 3) \tag{13}$$

$$\psi^0{}_{fibers} = \frac{k_1}{2k_2}\left[e^{k_2(I^*{}_i - 1)^2} - 1\right], where\ I^*{}_i = \kappa I_1 + (1 - 3\kappa) I_i \quad ; for\ i = 4,6 \tag{14}$$

The form of the SEDF was discussed in the previous chapter and the formulation follows from the same except that the damage variable η is to be multiplied to the deviatoric stress response. The primary hyperelastic curves for these parameters were plotted in MATLAB and have been shown below in figure (4.11). These material properties were used in Abaqus Standard as incompressible materials and in Abaqus Explicit with some amount of compressibility with a poisson's ratio of 0.495. Dog bone specimens were modelled in Abaqus and the stress-strain response for the given material was simulated. The dogbone specimen used has been shown below. One-eighth symmetry model was used for the uniaxial test simulation. Local element orientations were assigned to each element and fiber direction vectors as required by the HGO model were assigned through the input file from Abaqus.

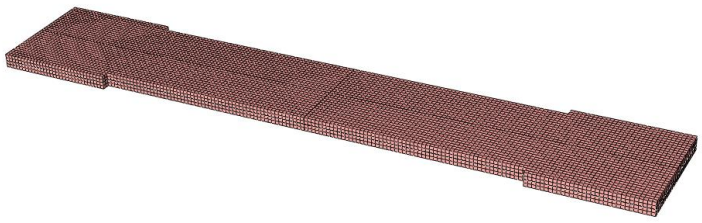

Figure 4.10: *Dog Bone specimen used in Abaqus to simulate the arterial response in the Theta direction*

The primary curves for the same compared to the curves for the experimental results are shown below.

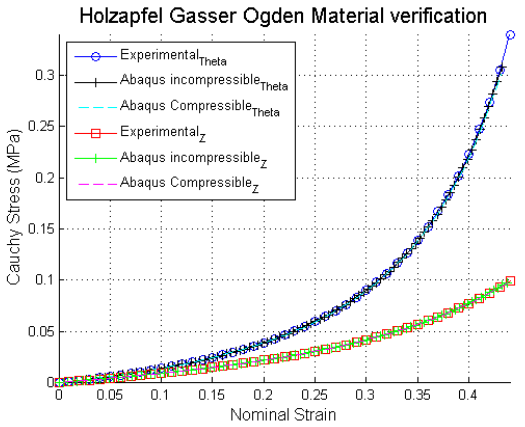

Figure 4.11: *Comparison of primary response of the experimental and FEA results for Human Thoracic Aorta Tissue*

Weisbecker et al found that, the damage in the matrix part is negligible and that the collagen fibers govern the damage in the material. However the material model in Abaqus only allows for an isotropic damage function, which means that the same damage parameters will be used for the matrix and the collagen part. This would create a shift in material response from the exact solution since the simulated response will be softer than the experimental result. The experimental and numerical values from Abaqus Standard and Explicit were plotted and the error of the response was calculated.

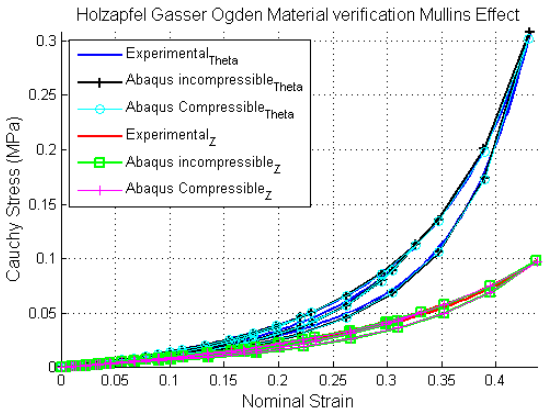

Figure 4.12 *Comparison of Cyclic loading response of the experimental and FEA results for Human Thoracic Aorta Tissue*

As seen in the graph above in figure (4.12), the error in the simulated response is zero for the primary loading curve since the Mullin's damage variable is inactive; however the error for the unloading curve initially increases from zero and reduces back to zero at the end of the unloading cycle. The maximum error recorded during the simulated response is 6.06 percent, which was deemed acceptable for the scope of this thesis.

5. PERCUTANEOUS TRANSLUMINAL ANGIOPLASTY
COMPUTATIONAL MODELLING

5.1 OVERVIEW

Balloon Angioplasty often accompanied by stenting is a procedure performed in order to increase the blood flow in a stenotic diseased artery. A pressure expanded balloon is introduced into the diseased portion of the artery using a balloon catheter mounted on a guide wire. Once at the site of blockage, the initially deflated balloon is expanded using (water) pressure ranging from 2 to 8 atm or more if needed. The procedure is also referred to as percutaneous transluminal angioplasty (PTA).

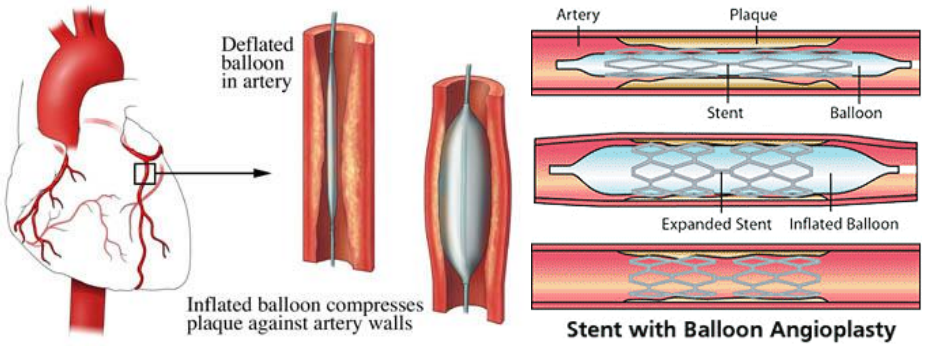

Figure 5.1*: Percutaneous Transluminal Coronary Angioplasty before and after balloon inflation* [34], *Stent implantation with balloon angioplasty*

PTA has been successfully used to treat arterial occlusions and till date remains one of the main procedures with or without stenting to treat coronary arterial stenosis. If the material properties of the tissue, the surrounding and the Balloon are characterized appropriately, the process of Balloon Angioplasty can be treated as a structural mechanics problem that can be solved using Numerical Techniques like the Finite Element Method.

As outlined in chapter 3, balloon angioplasty is associated with high rates of restenosis which has been attributed to the mechanism of action of PTA that induces high stresses in the arterial wall. Inelastic effects like damage and dissection are important aspects of the tissue response during the intervention [26]. It has also been observed that the presence of calcification has a key role in determining the reaction of vessel during angioplasty.

Therefore, characterizing the stresses and damage in the different components of the lesion is crucial in gaining a better understanding of the mechanical process.

5.2 COMPUTATIONAL SET-UP

5.2.1 Geometry

The vessel in consideration is a 3cm long segment of the Superficial Femoral Artery (SFA) depicted in figure (5.2). This histology image was provided courtesy of Cardiovascular Systems Inc. A sector of calcification can be seen in a layer of soft plaque which is fused with the intima. The artery wall is modelled as media and adventitia surrounded by a layer of surrounding tissue to mimic the environment that the vessel is embedded in. The plaque is modelled as a sector of calcified plaque embedded in a layer of echolucent plaque fused with the intima. The vessel geometry is assumed to be constant over the length of 3cm with plaque present over a central portion of 2cm. Angioplasty is performed over the lesion using a tri-Folded Balloon described by Laroche et al [22] with an expanded diameter of 5.5mm which is the average diameter of the parent vessel in figure (5.2). In order to study the effects of type of changing plaque morphology, an idealized geometry was created with the dimensions derived as average values from the SFA shown in Figure (5.2). The percentage stenosis of the idealized vessel was found to be 63.56 %. The original SFA model and the idealized geometry can be seen in figure 5.4

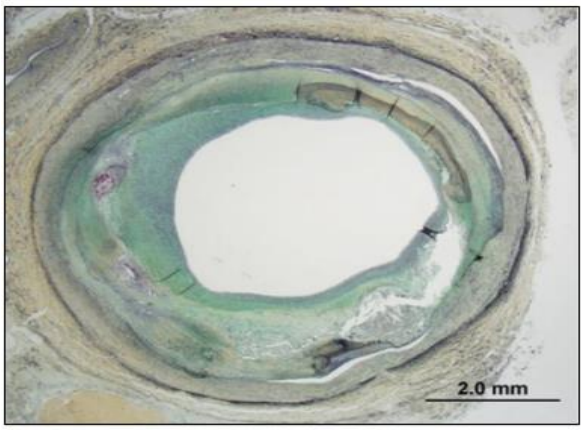

Figure 5.2: *Histology image of Superficial Femoral Artery used to model the 3D vessel*

Murray et al [60] carried out a study to assess the effect of calcified deposits in coronary arteries using intravascular ultrasound imaging (IVUS). The evolution of calcified plaque through stages of necrosis and spotty calcification to calcium arcs was outlined. The IVUS images from the study demonstrating these stages have been shown below (Necrotic Core: NC, Spotty calcification: SC).

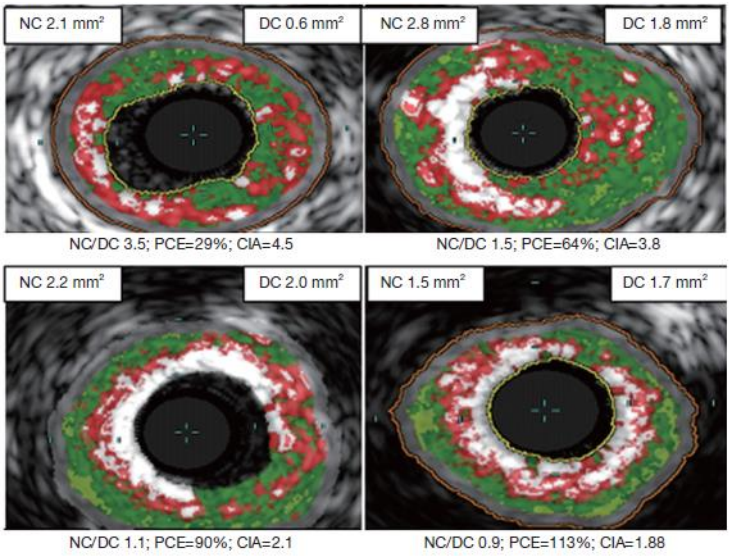

Figure 5.3*: Virtual Histology evolution of plaque from primitive necrosis (red) and spotty calcium through to calcium arcs (white). Fibrous material and fibro-fatty deposits are shown in green and light green respectively. From reference [60] with permission*

The calcification observed in the SFA from the histology image in figure (5.2) has an arc of calcium similar to studies observed by Murray et al [60].

In order to characterize the effect of increasing the calcified portion in the plaque, the angle subtended by the calcified layer was varied from 90 to 180and 270degrees. These three cases will henceforth be referred to as 90C, 180C and 270C case. Balloon angioplasty simulations were performed and the effect of the balloon artery interaction onto the stresses induced into the medial and adventitial layer were observed. The same balloon pressure of 8 atm was used for the all the cases. The results have been outlined in section 5.3.1

In order to study the effect of softening of plaque, the stiffness of the plaque components was reduced to 50% and 20%. The result on the stresses in the media and adventitia is reported in section 5.3.3

5.2.2 Mesh and Material Properties

The material properties used were discussed earlier in Chapter 4. The material models suitable for balloon angioplasty have been used to model the plaque. The artery has been modelled as an anisotropic model of the Holzapfel-Gasser-Ogden (HGO) type with fiber distribution and Mullins effect. The details of the same have also been described in chapter 4. The element type used for the aforementioned layers is C3D8R which is a brick type element in Abaqus Explicit with reduced integration and enhanced hourglass control and distortion control. A mass proportional damping has been used with a Rayliegh's parameter α. Material damping sensitivity study has been carried out and will be discussed in a later section. The muscle tissue has been modelled as a linear elastic material with a thickness of 0.1mm having a 50kPa elastic modulus and a poison's ratio of 0.3. The element type used for the same is S4R which is a shell element with reduced integration. Similar methods for modelling the muscle tissue were followed by Harewood et al [59] and Conway et al [24]. Taking advantage of the symmetry, half plane symmetry has been used for the model. The complete model is shown in the figure 5.4, however note that only half the length of the model was simulated using symmetry.

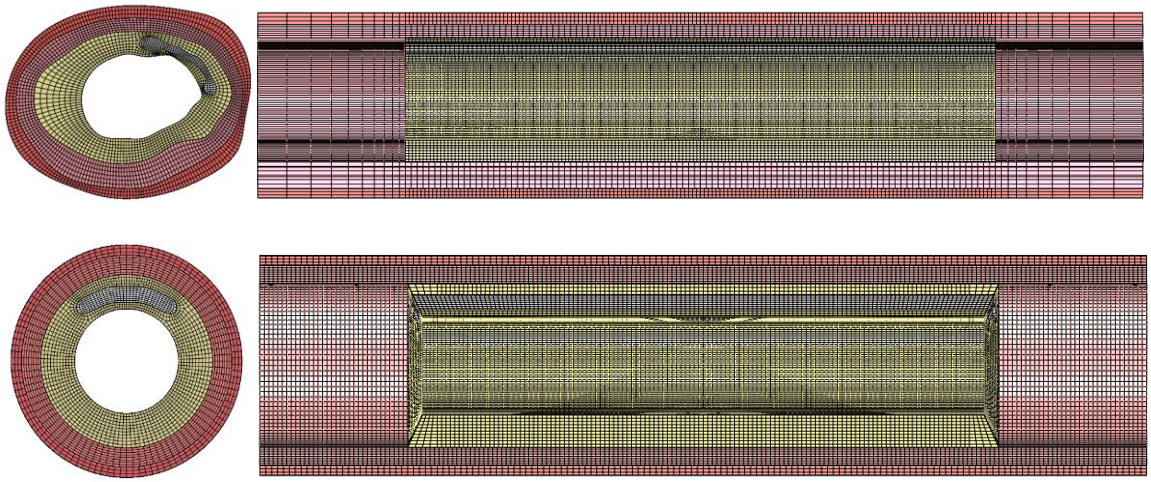

Figure 5.4: *Cross-sectional and axial section view of SFA model and idealized SFA model with 90 degree calcification. Half symmetry models of the meshes shown above has been used*

5.2.3 Balloon Model and free-expansion

The geometric description for a folded angioplasty balloon surface was first introduced by Laroche et al [22]. This model is formulated as follows. The geometry of the folded balloon surface is constructed by mapping the points of the deployed balloon onto the folded state. Points P_i on the deployed balloon of radius c are mapped onto points $\overline{P}_i$ of the folded balloon with inner radius a and outer radius b. In polar co-ordinates, points P_i and $\overline{P}_i$ can be expressed as (c, θ) and $(\bar{r}, \bar{\theta})$ respectively. A folded flap starts out at point $\overline{P}_1$ and ends at point $\overline{P}_2$. The angle β between P_1 and P_2 is given by

$$\beta = \frac{\phi}{2}\left(\frac{b+a+2c}{b+a}\right) \quad ; where\ \phi = \frac{2\pi}{n}, \tag{1}$$

Where *a*, *b* are the internal and external radii of the folded balloon shown in figure 5.5(b) and *c* is the radius of the balloon in the unfolded state in Figure 5.5 (d).

The angle between $\overline{P}_1$ and $\overline{P}_2$ is given by

$$\alpha = \frac{b+a}{2c}\,\beta \tag{2}$$

The angles and radii of the points P_i are mapped onto the points $\overline{P}_i$ using the following rule,

If $\theta \subset [0, \alpha]$, then

$$\bar{\theta} = \frac{\beta}{\phi}\theta \tag{3}$$

$$\bar{r}\,(\bar{\theta}) = a + \frac{b-a}{\beta}\bar{\theta} \tag{4}$$

If $\theta \subset (\alpha, \beta]$, then

$$\bar{\theta} = \left(\frac{\beta-\phi}{\phi-\alpha}\right)(\phi-\theta) + \phi \tag{5}$$

$$\bar{r}(\bar{\theta}) = a + \left(\frac{b-a}{\beta-\phi}\right)(\bar{\theta}-\phi) \tag{6}$$

Once, the radial and theta positions of the points $\overline{P}_i$ are known, the coordinates of the balloon can be used to model a computational geometry that can be used to create a finite element mesh using membrane elements. The number of folds used in the current balloon

model is 3 and therefore will henceforth be referred to as a tri-folded balloon model. The element type used was M3D4R in Abaqus Explicit which is a 4 noded membrane element with reduced integration. The thickness of the balloon used is 0.02mm and its initial internal and external radii are 0.75mm and 1mm respectively. The elastic modulus of the balloon is 920MPa with a poisson's ratio of 0.4. The material model and thickness for the balloon was obtained from Martin et al [23]. The tri-folded balloon has a length of 30mm with a constant folded cross-section for the majority of the length (26mm). A surface blend was created at the end of the balloon (2mm on each side) to an unfolded radial ring of 1mm radius which was kept fixed in the radial direction during the simulation in order to emulate the attachment to the catheter. The surface blend was meshed with a combination of triangular and quad membrane elements. The tri-folded balloon in its initial and final configurations has been shown in the figure below.

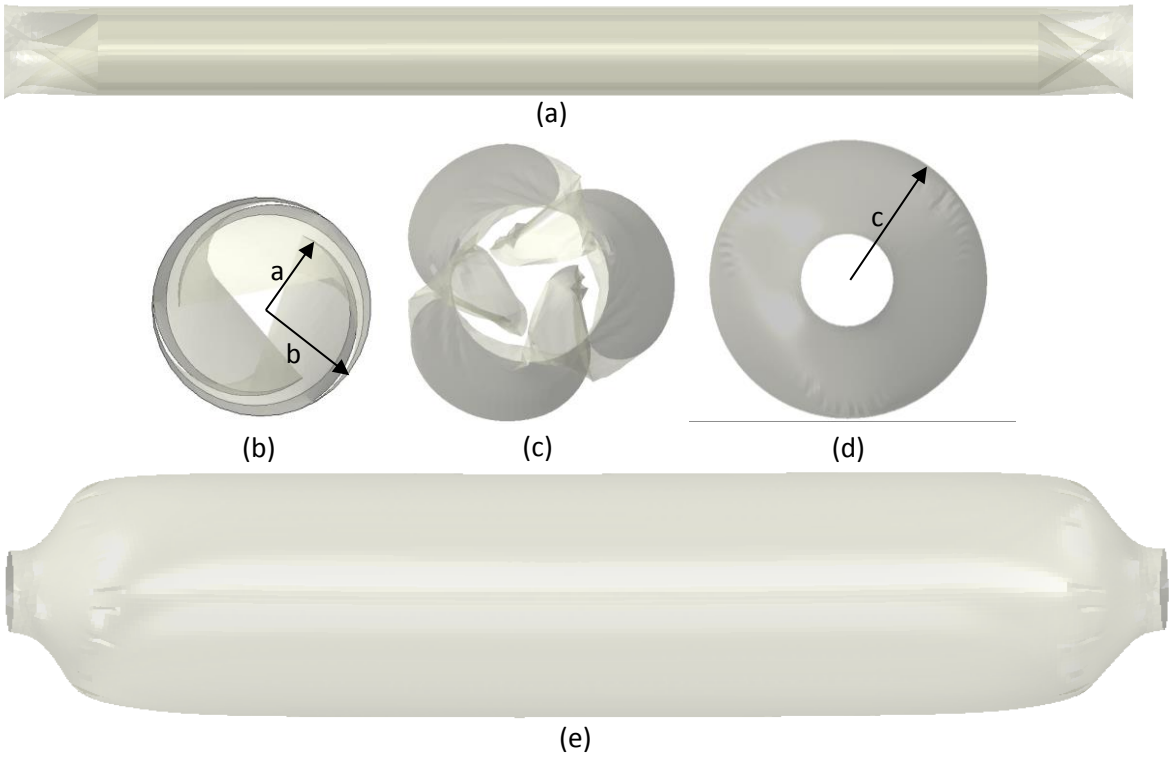

Figure 5.5: *Balloon in tri-folded configuration (a), cross-sectional view of 3 stages of Balloon deployment (not to scale) (b-d), Balloon in deployed state (e)*

5.2.4 Boundary Conditions and Loading

Given its extensive length in-vivo, the artery can be assumed to have a constant length during the process. Therefore, the far end of the artery has been fixed in the axial direction. Appropriate symmetry boundary conditions were applied at the other end. The balloon has been given a pressure load with an internal pressure of 8atm which lies within the pressure range for Angioplasty of calcified lesions. The angioplasty is simulated in two steps similar to Laroche et al [22], with unfolding or deployment and then radial expansion of the balloon due to internal pressure. The balloon is held at inflated for a time of 5 seconds since the peak stresses in the lesion are seen to plateau by this time. The interaction of the balloon with the internal wall of the vessel was assumed to be frictionless.

5.3 RESULTS OF ANGIOPLASTY SIMULATIONS

5.3.1 Effect of varying degree of calcification

Results for 90C case

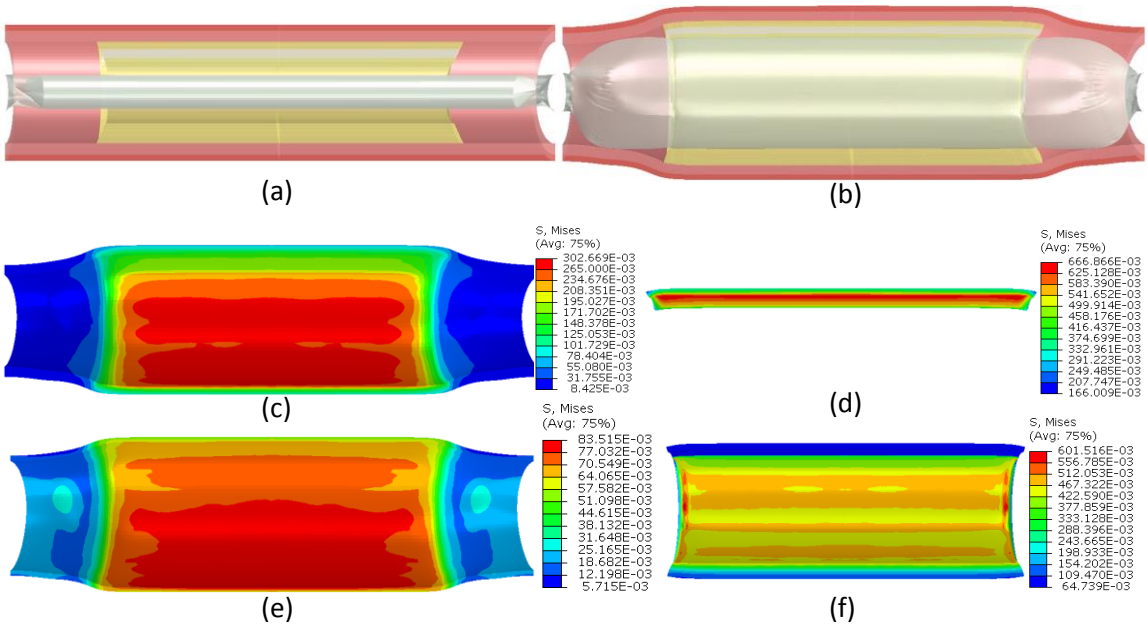

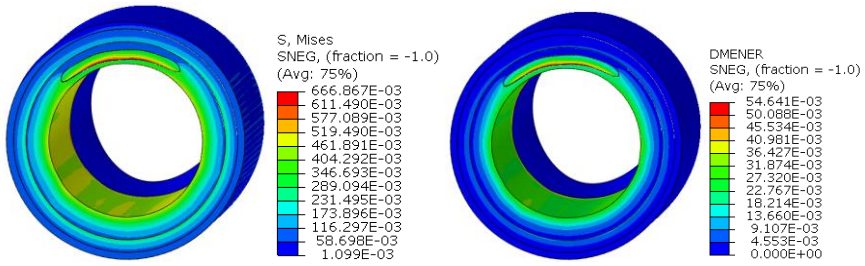

(g) (h)

Figure 5.6: *Initial (a) and Deformed configuration (b), Axial section cut of Mises stresses (MPa) in Media (c), Calcification (d), Adventitia (e) and Soft plaque (f), , Overall Mises stress field (MPa) in half symmetry model(g), Damage energy per unit volume dissipated for 90C case(h) (MJ/m^3)*

The maximum stresses in the media (302.67 KPa) and the adventitia (83.51 KPa) are seen to develop in the non-calcified side of the lesion and can be observed in figure 5.6 (c,e). Thus the region of the medial and adventitial tissue located behind the calcified layer faces lesser stress levels and is in a sense protected by the calcium. This implies that the possibility of vascular injury is more pronounced in the non-calcified portion of the vessel wall. This result is consistent with the reported observation by Ivan Casserly [61] which mentions that the in case of calcified lesions, high balloon pressures often result in increasing the risk of dissections to the compliant non-calcified portion of the media.

The damage energy represents the amount of energy dissipated per unit volume in the element. The higher the stresses induced, the higher will be the damage energy dissipation since it is associated with the peak stresses developed in the material. Thus the damage energy density (Figure 5.6 h) in the media and adventitia is higher in the non-calcified side. Similar results for the 180C case can be seen below.

Results for 180C case

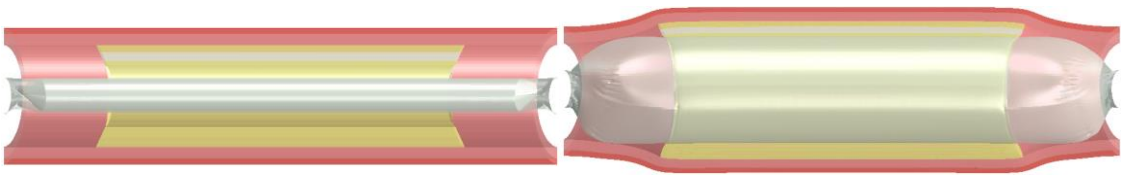

(a) (b)

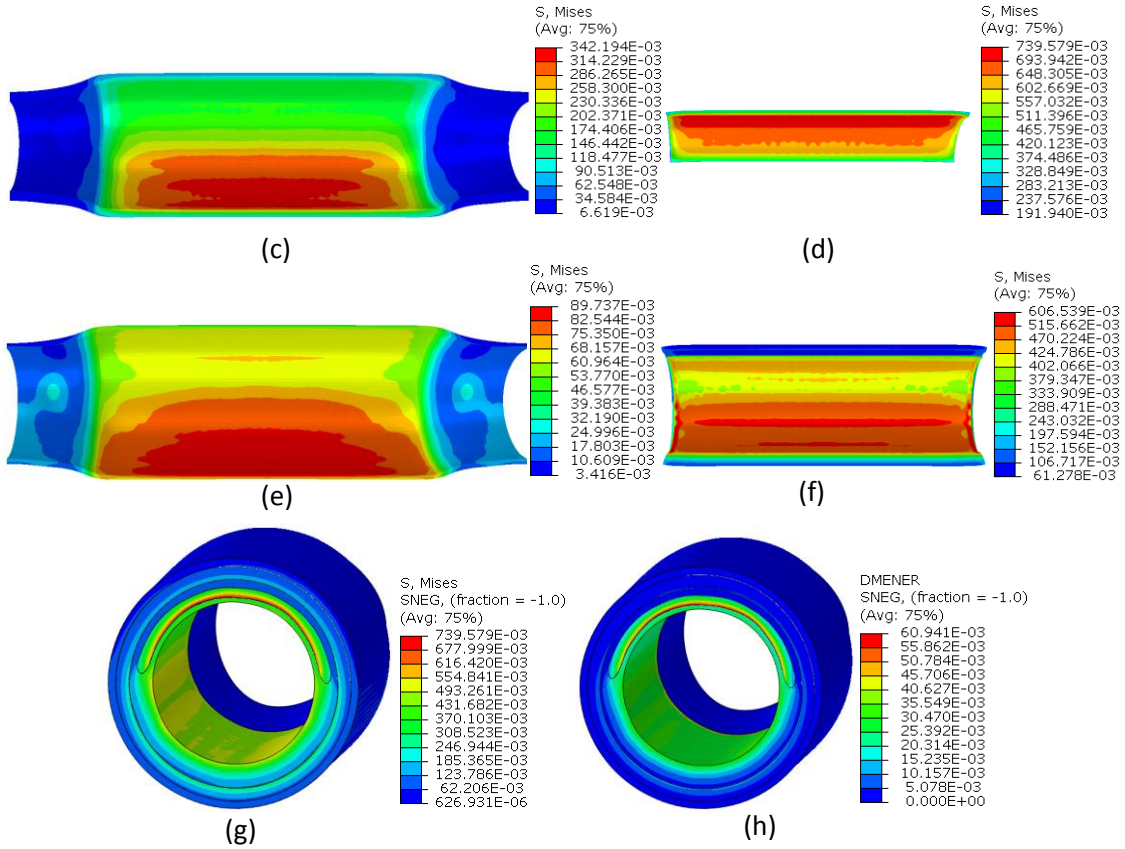

Figure 5.7: *Initial (a) and Deformed (b) configuration, Axial section cut of Mises stresses (MPa) in Media (c), Calcification (d), Adventitia (e) and Soft plaque (f) , Overall Mises stress field in half symmetry model (g) and Damage energy per unit volume dissipated for 180 C case (h) (MJ/m^3)*

These results demonstrate that for the 180C case, similar to 90C, the major stresses in the arterial layers are on the non-calcified region. The peak stresses in the media (342.19 KPa) are seen to be higher than those found in 90C (302.67 KPa). However the number of elements located behind the calcified layer is also larger; therefore a large portion of the vessel wall is protected by the layer of calcium. The high stress region can therefore be said to be relatively more localized. The damage energy per unit volume also follows a similar trend as expected that is, the damage energy density in the vessel wall is higher on the non-calcified side as compared to the side protected by the calcification.

Results for 270C case

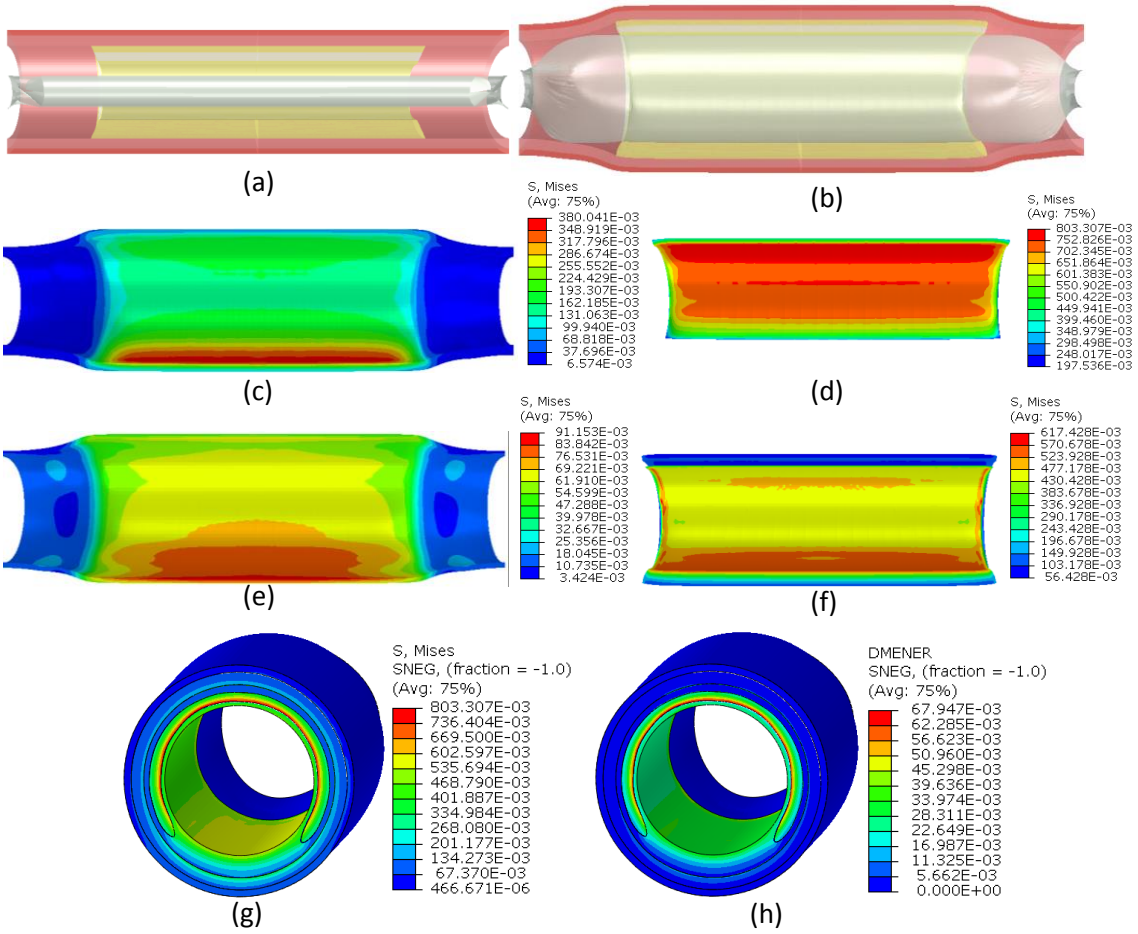

Figure 5.8: *Initial (a) and* D*eformed (b) configuration, Axial section cut of Mises stresses (MPa) in Media (c), Calcification (d), Adventitia (e) and Soft plaque (f), Overall Mises stress field in half symmetry model(g) and Damage energy per unit volume dissipated for 270C case (h) (MJ/m^3)*

The peak stress in the media (380.04 KPa) in the 270C case is larger than the previous cases (302.67Kpa for 90C and 342.19 KPa for 180C). The stress is concentrated as one would expect, in the non-calcified side of the lesion. The damage energy per unit volume also follows a similar trend as the peak stresses being maximum on the non-calcified side of the wall. The peak stresses in the adventitia in the three cases studied seem to be quite similar. A histogram plot shown below shows the medial stress distributions over the length of the disease in the three different cases studied above.

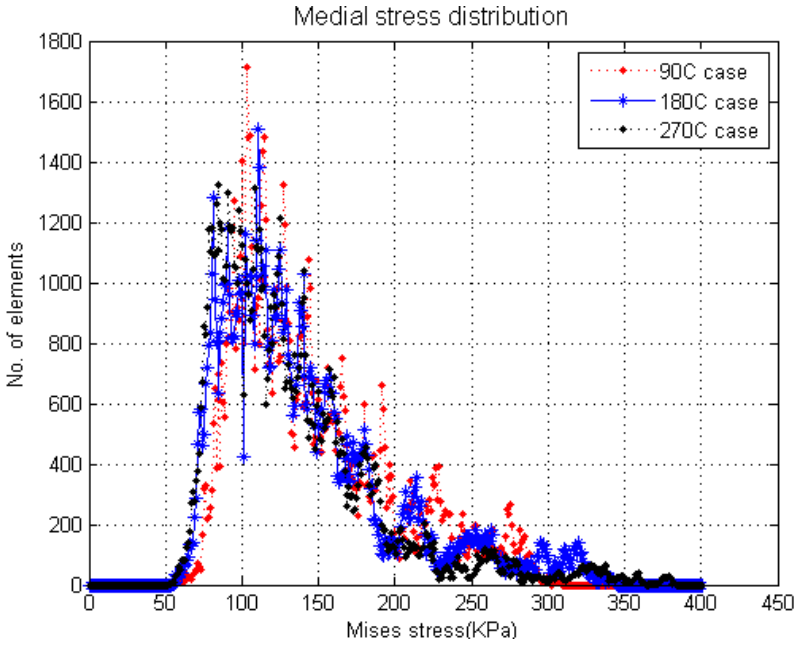

Figure 5.9: *Histogram plots of medial stress distribution for 90C, 180C and 270C cases undergoing PTA*

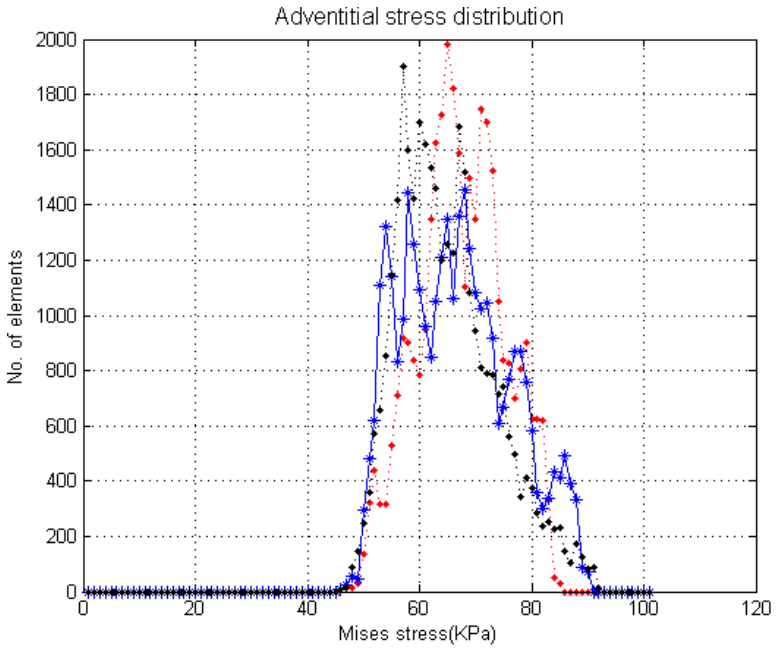

Figure 5.10: *Histogram plots of adventitial stress distribution for 90C, 180C and 270C cases undergoing PTA*

The figure (5.9) shows that the effect of calcification on medial stresses is quite ambiguous. For example, compare the black and red curves for medial Mises stress;

although the peak stresses increased with increasing calcification, the high stress region became more localized since the region protected by the calcified layer in the 270C case seemed to be larger. Therefore, calcification is seen to perform, both a detrimental as well as a protective function. It is seen in all the aforementioned cases however, that the stresses in the arterial wall during balloon angioplasty are more pronounced on the non-calcified portion therefore making it more prone to vacular injury.

5.3.2 Mesh convergence study

A mesh convergence study was performed for the angioplasty simulation with the 180deg calcification case. An h-type mesh convergence was implemented, which means that the number of elements was increased keeping the order of the elements the same. The order (p-type) was not varied since that would increase the computational time drastically. Convergence was based on the generally accepted criterion of 5% change in solution. Once a converged mesh was obtained, similar mesh densities were used for the other simulations. Three mesh densities were used for the mesh convergence study. The solution presented earlier had a mesh size of 252032 elements; two other finer meshes with 299781 and 374559 elements were used and the solution error of the peak stresses with respect to the first mesh was evaluated. The error for the second mesh of 299781 elements was seen to be 1.99% and the error for the third mesh with 374559 elements was 3.02%. Therefore the first mesh was considered a converged mesh. The solution of the equivalent stress field along with the mesh for the three mesh densities has been shown in Figure 5.11.

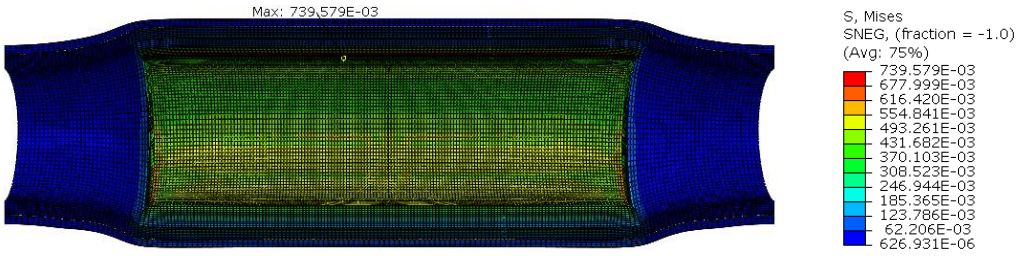

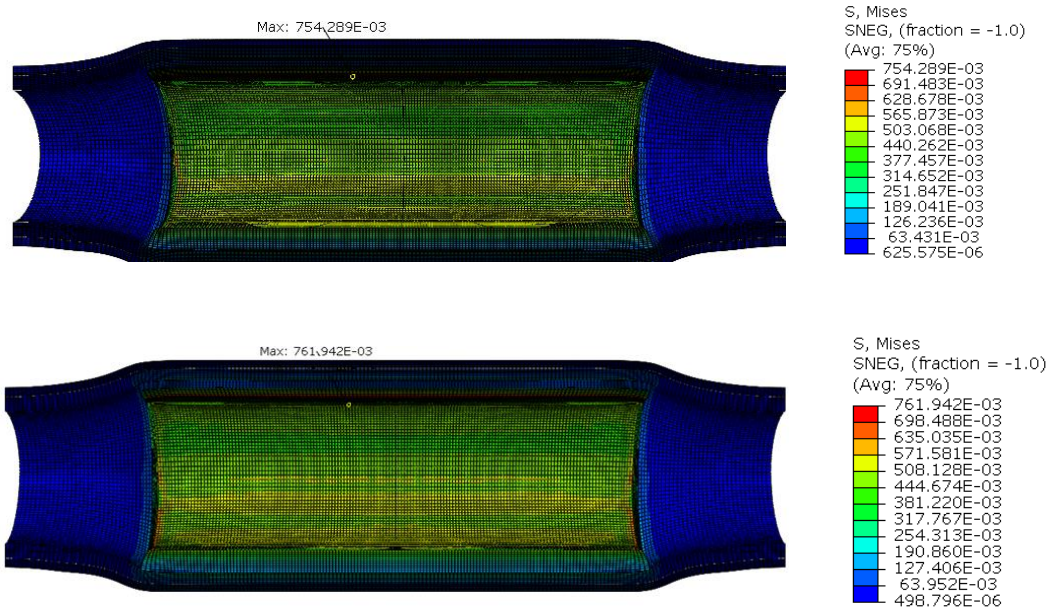

Figure 5.11: *Axial cut of equivalent Mises stress field for the three mesh densities for 180C*

5.3.3 Effect of plaque softening

As discussed earlier, biological tissues tend to soften or damage under cyclic loading and that the peak stresses developed in the medial layer may be an important marker for vessel injury. Angioplasty induces high stresses in all the components of the lesion including the plaque and the arterial walls. On unloading and reloading the angioplasty balloon, the stresses observed at the same strain level will be smaller as an outcome of Mullins effect until the previously achieved maximum strain energy is surpassed. The response of the lesion components will in general be softer. However the peak stress in medial wall during the complete history of deformation would still be large due to the first loading cycle. If the plaque components could to be damaged or softened, without significantly damaging the medial layer, the stresses induced in the medial layer would be worth noting. Therefore, plaque models with 50% the original stiffness and 20% the original stiffness were simulated and the stresses in the media were calculated and can be seen in the Figures (5.12 and 5.13) respectively.

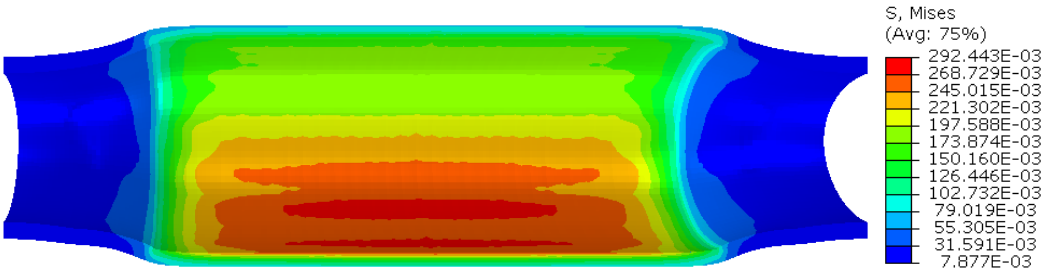

Figure 5.12: *Medial stress in lesions having plaque components with 50% the original stiffness*

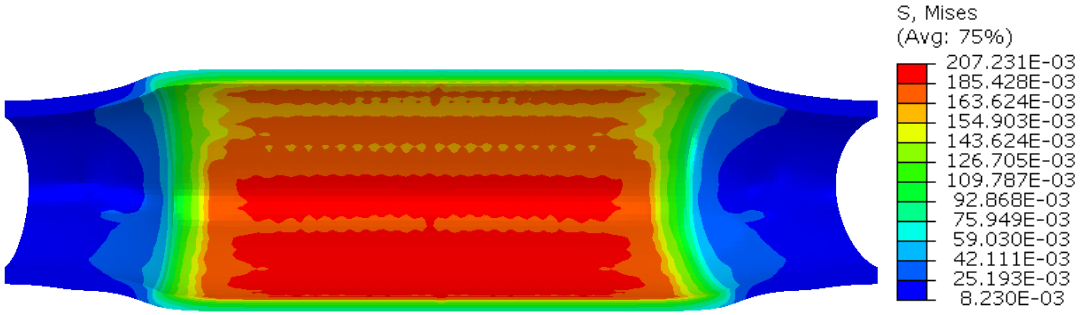

Figure 5.13: *Medial stress in lesions having plaque components with 20% the original stiffness*

It can be observed in the figures above that the peak stress observed in the medial layer decreased as the stiffness of the plaque layers was decreased. Originally, the peak stress in the media during angioplasty simulation of the 180C case was 342.19 KPa and reduced to 292.44 Kpa and 207.23 KPa for plaques with 20% and 50% the stiffness. Thus increasing the compliance or decreasing the stiffness of the plaque may decrease the chances and degree of vascular injury induced in the arterial wall under the action of a semi-compliant balloon. In order to soften to plaque components a mechanism like orbital atherectomy may be used and thus will be discussed following the next chapter.

5.3.4 Results with inclusion of Plasticity

Lawlor et al [5] reported the ultimate tensile stress values for the plaque models in uniaxial tension. The average tensile curves for soft plaque have been used in this research as discussed earlier in the material modelling section. An average ultimate tensile stress (UTS) value for these plaques was determined (231.5KPa) and used in a perfect plasticity model along with the hyperelastic material model currently being used. Perfect plasticty implies that after reaching the yield point, the material can take no further stress on further loading. The tensile properties for calcified plaque were derived

from Maher et al [3], however no ultimate tensile stresses were reported in the study. Therefore the UTS for the calcified plaque was derived from Loree et al [1] (701Kpa). This value was also used as a perfect plasticity model along with the the currently used hyperelastic material model. UTS values for media and adventitia were derived from Holzapfel et al [10] however the stress values observed in these layers was smaller than the reported values from the study. Therefore no plasticity was observed in these layers.

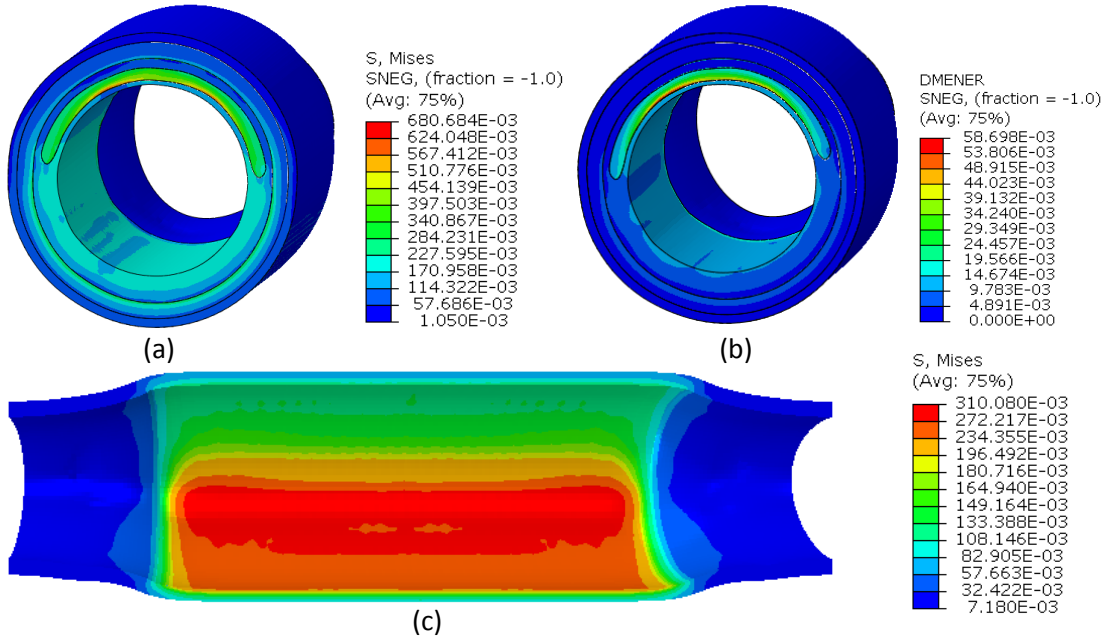

Figure 5.14: *Equivalent Mises stress in the half symmetry model (a) (MPa), Damage energy per unit volume (MJ/m^3) in the half symmetry model (b), Equivalent Stress in the Medial layer(c) (MPa) for the simulation with inclusion of plasticity*.

The mises stress field and damage in the entire lesion and the mises stress field in the media can be seen in the figure 5.14.

5.3.5 Results for superficial femoral artery (SFA) with plasticity

The original lesion geometry was also simulated for PTA to characterize the wall stresses and damage energy density. As discussed above, a perfect plasticity model was included for the respective UTS values. The results for the simulation can be seen in Figure 5.15

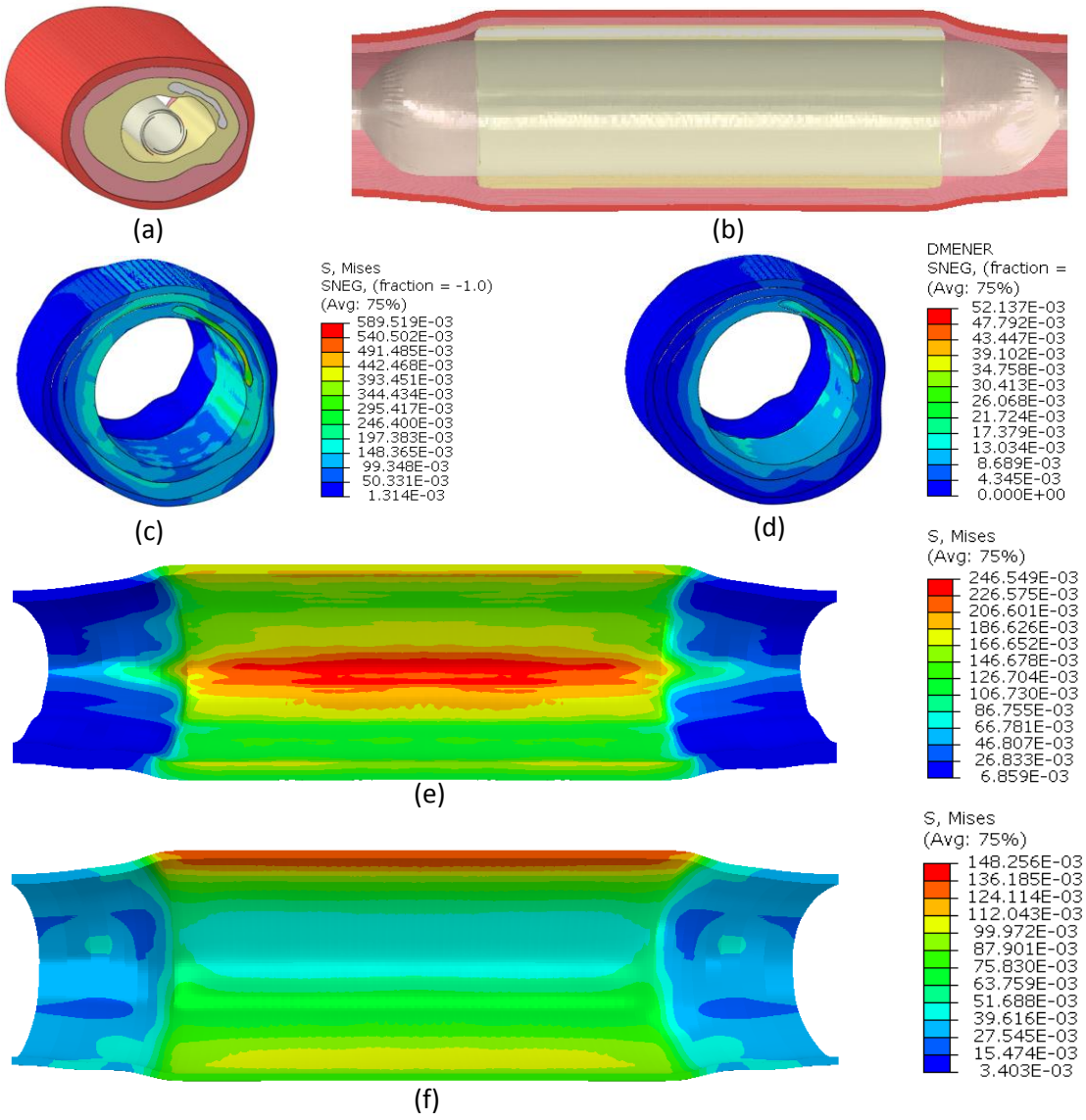

Figure 5.15: *Undeformed shape-half symmetry model (a), deformed shape (b), Equivalent Mises stress in the half symmetry model (MPa)(c), Damage energy per unit volume (MJ/m^3) in the half symmetry model(d), Equivalent Stress in the Medial layer(e)(MPa), Equivalent Stress in the Adventitial layer(f)(MPa), for the SFA simulation with inclusion of plasticity*

As seen in Figure 5.15, the peak stresses in the media and adventitia are seen to be on the non-calcified portion of the artery and the shoulder regions of the calcification therefore making these regions more prone to damage.

5.3.6 Damage energy density analysis for PTA

Damage energy density represents the amount of energy dissipated per unit volume in an element. The damage energy density values for the 2cm portion of the lesion were calculated and the mean damage energy density of every layer was evaluated for the simulations presented above. The results have been summarized in Table 5.1.

	Mean Damage energy density (MJ/m^3)				Total Damage energy Density	Percentages			
	Calcification	Echolucnet plaque	Media	Adventitia		Calcification	Echolucnet plaque	Media	Adventitia
90C PTA	5.60E-02	2.46E-02	8.40E-03	1.58E-03	9.06E-02	61.82	27.16	9.27	1.74
180C PTA	6.30E-02	2.44E-02	8.20E-03	1.49E-03	9.71E-02	64.89	25.13	8.45	1.53
270C PTA	7.44E-02	2.36E-02	7.60E-03	1.45E-03	1.07E-01	69.50	22.05	7.10	1.36
180C PTA with Plasticity	4.50E-02	1.37E-02	7.20E-03	1.27E-03	6.71E-02	67.02	20.37	10.72	1.89
SFA with plasticity	4.22E-02	1.70E-02	6.52E-03	2.64E-03	6.83E-02	61.77	24.82	9.54	3.86

Table 5.1: Damage energy density for the different components of the lesion for PTA simulations

From Table (5.1), it can be concluded that of the total damage energy dissipation in the lesion, the media experiences about 7-11% damage and the adventitia takes about 1-4% damage. Also as the degree of calcification was increased, the amount of mean damage energy and percentage decreased which goes to show that the peak damage and therefore the peak stresses even though higher are more localized as the degree of calcification is increased.

6. ORBITAL ATHERECTOMY

EXPERIMENTAL INVESTIGATION AND COMPUTATIONAL MODELLING

6.1 OVERVIEW

Orbital atherectomy is one of the traditional atherectomy procedures used for debulking of calcified plaque. The procedure is carried out using a spinning grinding tool known as the crown rotating and orbiting inside the lesion. The atherectomy devices were introduced conceptually with the idea to reduce plaque burden without affecting the rest of the vessel wall. [62]

Figure 6.1: *Peripheral orbital atherctomy system Diamondback 360 (CSI) and orbital atherectomy crowns* [63]

The orbital atherectomy procedure has recently gained much attention in regards to changing lesion compliance. Dattilo et al [31] conducted a study in 2014 to test this hypothesis. Fifty patients were enrolled with calcified femoropopliteal disease. Since BA for calcified lesions in FP disease is associated with increased dissection rates, the objective of this study was to compare the results of OA + BA vs standalone BA. It was seen that the mean maximum balloon pressures in OA +BA was 4 atm as compared to 9.1 atm in BA alone. Therefore it was concluded that OA + BA yields better luminal gain by improving lesion compliance and decreasing stenting for femoropopliteal disease. Similarly, a study by Deokar and Nguyen that will discussed in the next section observed a change in compliance of the vessel after atherectomy at low pressure levels.

Zheng et al [64] conducted a study on the motion and grinding forces of the orbital atherectomy crown in an arterial phantom using a high speed camera and a piezoelectric

dynamometer. It was observed in the study that the crown motion consists of two frequencies: a high frequency rotation about its center axis and a low frequency orbiting around the vessel lumen. At crown rotational speeds of 60,000, 90,000 and 120,000 rpm inside a phantom artery of 4.8mm diameter, the orbital frequencies were 18, 38 and 40 Hz, respectively. At the speed of 120,000 rpm, a vessel wall radial indentation of approximately 0.5 mm was observed.

6.2 EXPERIMENTAL STUDY OF CHANGE IN LESION COMPLIANCE DUE TO ORBITAL ATHERECTOMY PROCESS

Clinical investigations of OA have suggested that OA procedure may improve lesion compliance. In the study by Shammas et al, lesser dissections were observed during PTA when pre-treated with OA [30]. Therefore an experimental investigation in cadaveric lesions was carried out to explore the change in compliance post orbital atherctomy.

The compliance measurement study was conducted at Cardiovascular Systems Inc. (CSI), St.Paul Minnesota by Deokar and Nguyen. Compliance of a lesion is defined as the slope of the pressure area or pressure volume curve [65, 66] .It has an inverse relation with stiffness of the material which implies that higher the stiffness, lesser the compliance of the material and lower the stiffness, more compliant the material. In the experimental study, 2 cadaveric superficial femoral arteries were obtained and mounted on a test set up. The ends of the vessel were fixed and the vessel was submerged in a food grade grease to emulate the surrounding environment of the artery. The internal diameters of the arteries were measured using vernial capilers at the ends and were noted to be 6mm and 5mm. Similarly, the lengths of the arteries were measured to be 178 mm and 310mm respectively. OA device provided by CSI was the Diamondback 360 peripheral orbital atherectomy system with 1.5 and 2mm solid crowns. An internal pressure was applied to the vessel using a hydraulic pressurizing apparatus. Pressure levels of 80mmHg, 100mmHg, 120mmHg, 140 mmHg and 160mmHg were used. Optical coherence tomography (OCT) imaging was used to measure the lumen diamters at the applied pressure levels. The arteries were divided into several sections of 5 cm each along the length. One section of the first artery and two sections of the second artery were treated with OA procedure. The artery holding fixture with the cadaveric SFA sample has been

shown in Figure 6.2. The OCT and OA catheters were introduced through the introducer sheath mounted on the distal end.

Figure 6.2: *Artery holding fixture for cadaveric SFA samples with introducer sheath*

Fluroscopy was used at all times to montior the position of the crown at the specific sections inside the vessel as shown in Figure 6.3.

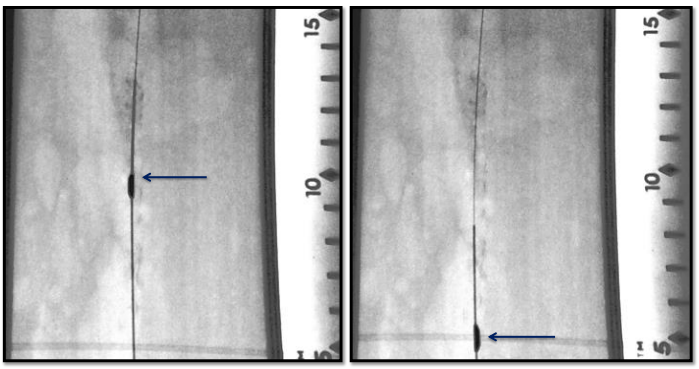

Figure 6.3: *Fluroscopy image of OA device inside the lesion along with marker along the length of the lesion*

OCT imaging was performed on the untreated vessel at the different internal pressure levels as an initial state characterization. Orbital atherectomy was performed on selected sections and OCT pullback was again carried out at the aforementioned pressure levels. OCT images of the cross-section of the lesion can be seen in Figure 6.4 below.

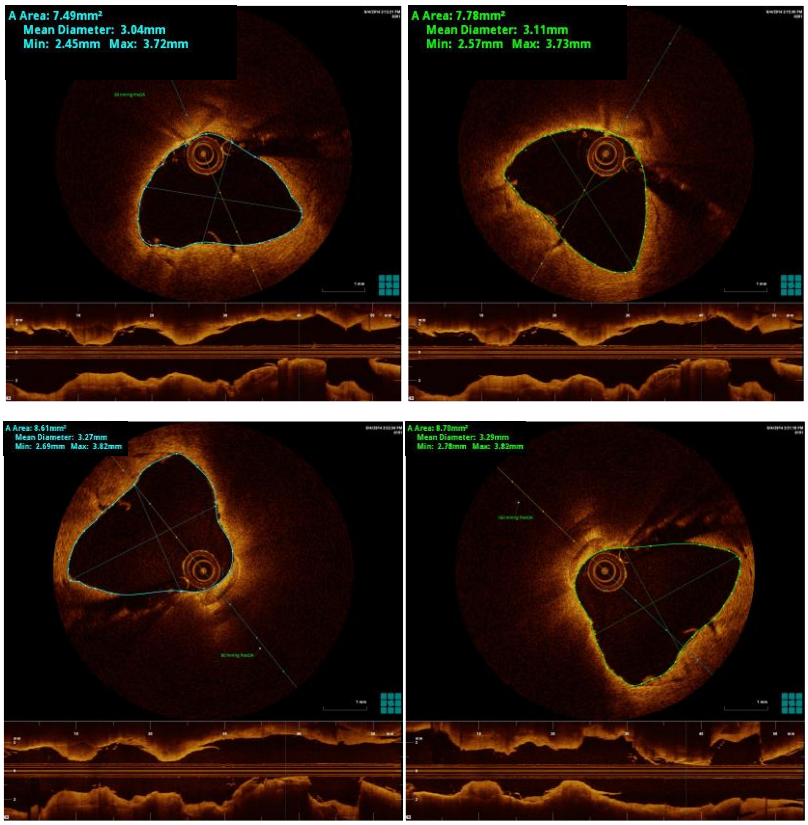

Figure 6.4: *OCT image of the crossection before OA (top) and after OA(bottom) at 80mmHg (left) and 160mmHg(right) respectively*

The results of the study showing the cross-sectional areas at different pressure levels have been summarized in the tables below.

Artery 1 Section 1 (10-5cm)		
Pressure (mmHg)	Areas (mm^2)	
	Pre OA	Post OA
80	6.16	7.06
100	6.15	7.11
120	6.25	7.26
140	6.25	7.3
160	6.3	7.35

Pressure (mmHg)	Areas (mm^2)	Artery 2 Section 2 (25cm-20cm)					
		Cross-Section 1		Cross -Section 2		Cross-Section 3	
		PreOA	PostOA	PreOA	PostOA	PreOA	PostOA
80		11.49	12.1	13.63	14.19	16.21	17.32
120		11.98	12.28	14.26	14.54	16.58	17.59
160		12.28	12.62	14.44	14.98	16.68	18.17

Pressure (mmHg)	Areas (mm^2)	Artery 2 section 1 (10cm-5cm)							
		Cross-Section 1		Cross-Section 2		Cross-Section 3		Cross-Section 5	
		PreOA	PostOA	PreOA	PostOA	PreOA	PostOA	PreOA	PostOA
80		7.16	7.31	7.49	8.61	7.81	8.21	9.6	10.12
120		6.73	7.67	7.75	8.69	8.4	8.71	9.67	10.24
160		6.81	7.32	7.78	8.7	8.43	8.7	9.87	10.43

Table 6.1 Area vs pressure values from OCT study pre and post orbital atherectomy procedure

Compliance is defined as $\frac{dV}{dP}$ or for a constant length of artery, as $\frac{dA}{dP}$ or $\frac{\Delta A}{\Delta P}$ where P is the internal pressure and A is the cross-sectional area [65, 66]. A trendline was calculated for the graphs of pressure versus area and compliance was the slope of the trend-line. The percentage increase in compliance before and after OA was evaluated and the overall percentage was averaged out for the considered samples. The cross-section 4 of the artery 2 section 1 was not considered since no calcification was present in that section. Therefore, only sections 1,2,3 and 5 were considered. One of the 8 cross-sections used was excluded because although there was an increase in compliance at this location, the compliance slope pre-OA was negative which is physically irrelevant since it would mean decreasing area with increasing load. There was a large dissection present at this location which could be the reason for the anomaly. The compliance change for all the cross-sections was evaluated and the mean was found. The final results demonstrated a mean 8.26% increase in area at a given pressure and a mean 10.44 % increase in compliance of the lesion after orbital aterectomy for the two SFA cadaveric lesions.

While these studies have shed light on the clinical implications and experimental observations of the OA procedure, computational modelling exploring the structural response of the tissue during OA have not yet been done. Thus in this research, a numerical study of Orbital atherectomy was also performed using FEA in Abaqus in order to study the softening effect observed in the exerpimental study.

6.3 COMPUTATIONAL SET UP

6.3.1 Geometry, Mesh and material properties

The element types for the different layers of the atherosclerotic lesion are the same as discussed in the angioplasty simulation. The orbital atherectomy tool better known as the OA crown has been modelled using shell type rigid elements. The material models used for plaque in the OA simulations have been discussed in chapter 4. The material models for the artery and the muscle tissue are the same as in the angioplasty simulations. No symmetry approximation has been made since for the crown dynamics no plane of symmetry exists. The geometry of the crown is shown below in Figure 6.5.

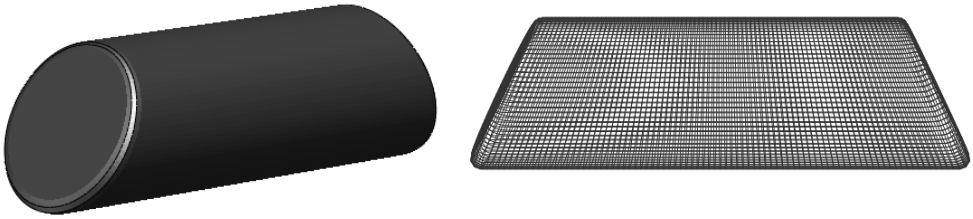

Figure 6.5*: Solid crown model (3D view) and discrete rigid element mesh for crown used in OA simulations*

The axial section of the overall mesh used (90deg calcium) has been shown below in Figure 6.6. The mesh size in this case is 775710 elements. The mesh was decided from a mesh convergence analysis which will be discussed in section 6.4.2. In order to study the effect of varying the degree of calcification, the 180C case was modelled with a similar mesh density.

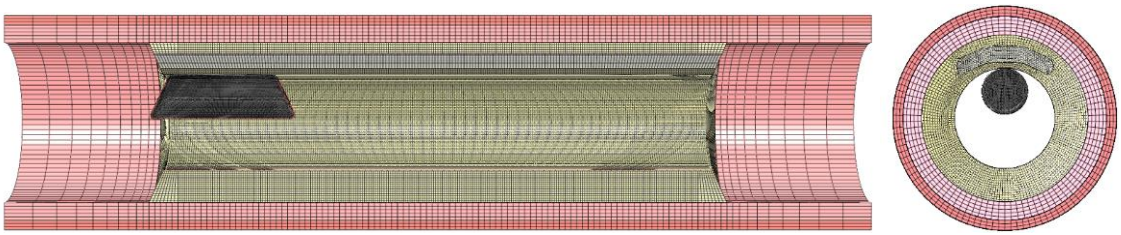

Figure 6.6 *Axial and cross-sectional view of mesh used in OA simulations (90C case)*

6.3.2 Boundary conditions and loading

Zheng et al [64] observed that at 120,000 rpm rotational speed, the orbiting frequency of the crown was seen to be 40Hz. A radial displacement of the crown into the vessel wall was observed to be 0.5 mm in the above study. Therefore, for the simulations to follow, the crown was given a radial displacement of 0.5 mm in the first step and held fixed in the radial direction. The crown was then given an orbiting frequency of 40Hz and moved axially along the length of the vessel at a rate of 1cm/s. One complete pass with the crown returning to its original starting position was simulated. The simulation time for the combined rotation and axial translation of crown through the diseased portion of 2cm was therefore 4 seconds. The interaction of the crown and the lesion has been modelled as frictionless with kinematic contact control. The 3cm long vessel was constrained at both the ends in the axial direction to emulate a semi-infinite vessel and circumferential direction to constrain rigid body rotation.

6.4 RESULTS FOR ORBITAL ATHERECTOMY SIMULATIONS

6.4.1 Effect of varying degree of calcification

The case of the 90deg (90C) and 180deg (180C) calcified plaques were simulated to study the effect of OA on lesions with increasing degree of calcification. The equivalent Mises stress field and principal compressive logarithmic strain field for a given instant of t = 2sec in the 90C case has been plotted below in Figures 6.7, 6.8 respectively. The damage energy plot at 0.1 seconds after the unloading of the crown tool has been shown as well in Figure 6.7.

Results for 90C case

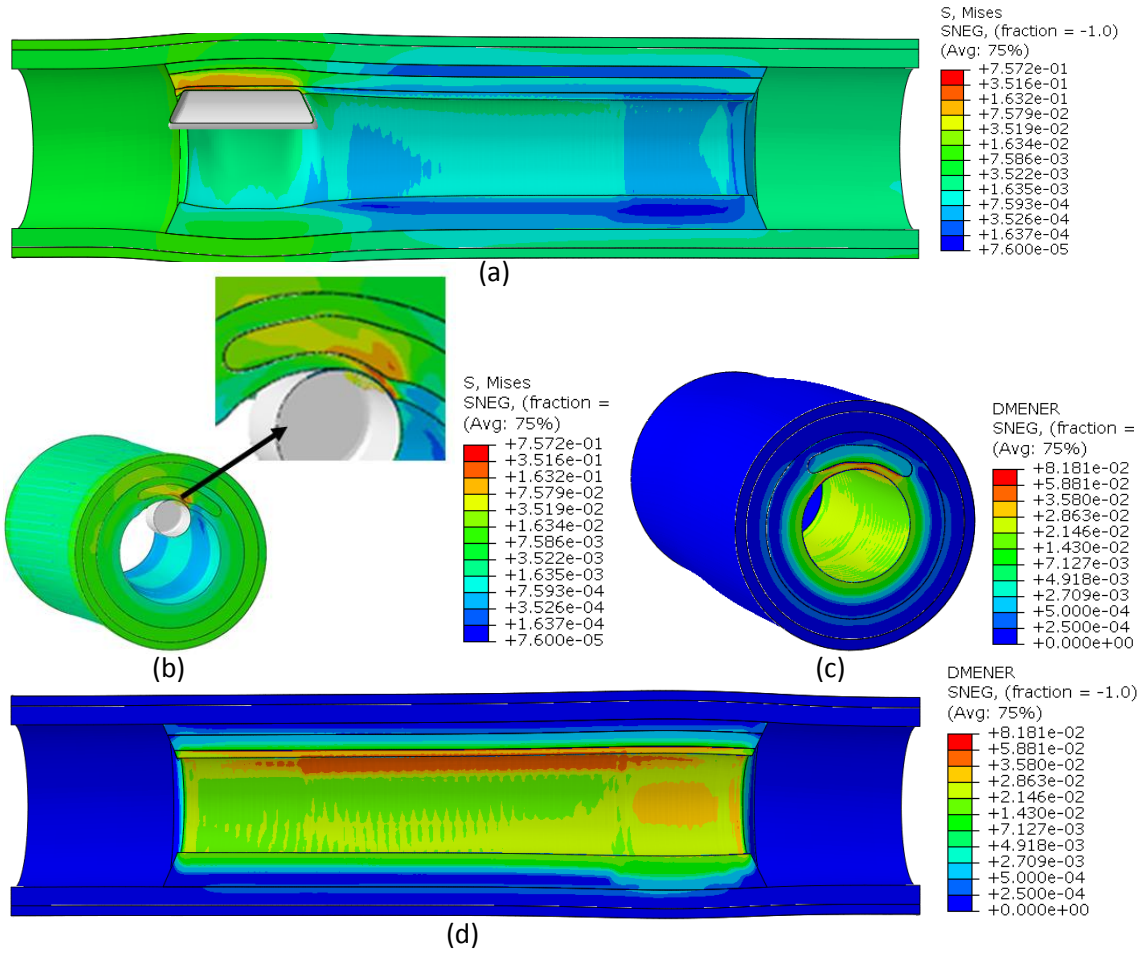

Figure 6.7*: Equivalent Mises stress -axial section (a), Equivalent mises stress -cross-section (b) at t=2sec. Damage energy after OA simluation -cross-section (c), damage energy after OA simulation -axial section (d) for 90C*

It can be seen in the Figure 6.7 above that the stress field is quite localized and concentrated in the area of contact near the soft-plaque and calcification. The maximum stresses developed in the media and adventitia at the time snapshot of 2 seconds plotted in Figure 6.7 are 39.1KPa and 15.1 KPa, which are smaller in comparison to the stresses in the contact region which are 757KPa in the Echolucent plaque and 196KPa in the calcified plaque. The relative stresses in the media and adventita to the plaque components are also seen to be smaller in OA than in PTA simulations due to the nature of the mechanism.

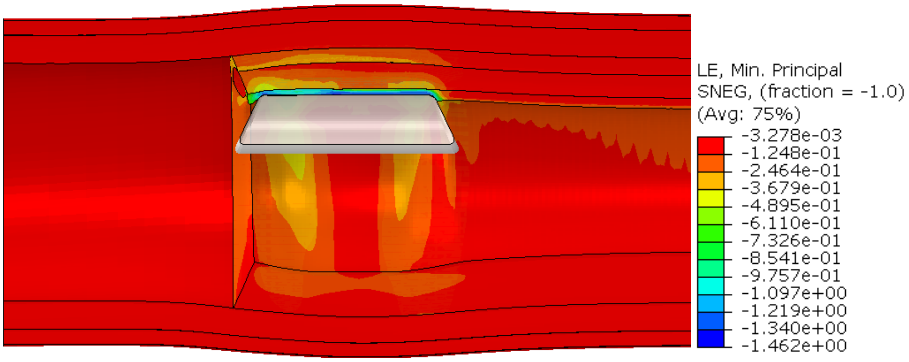

Figure 6.8: *Logarithmic compressive strain in the principal dirrection at t=2sec*

As discussed earlier in the formulation of Mullins effect, the damage or softening of a material is given by the damage variable η that is governed by the maximum energy state that the material has been subjected to throughout the history of deformation. An estimate of the strain energy at the maximum energy state can be derived based on the strains observed in the material throughout the history of deformation. The lorarithmic strains at the instant of t =2 seconds are plotted in Figure 6.8 and demonstrate that highly compressive strains are formed at the area of contact. The maximim principal compressive nominal strain in the direct vicinity of the crown at the given snapshot in time is -0.77 for the echolucent plaque and -0.39 for the calcification. At the same time, across the thickness of the two plaque layers, the principal compressive nominal strains observed are -0.65 and -0.22 respectively. When the crown is in contact with the echolucent plaque sector on the non-calcified side of the lesion, the strains observed in the echolucent plaque are around -0.7 in the vicinity of contact and -0.33 through the width. The area of contact of the crown rapidly changes throughout the simulation since the crown is known to orbit at 40 Hz and move 1 cm/s in the axial direction. The solution

field therefore is similar throughout the angle and length of the plaque being treated. The strain fields mentioned above can be used to give an estimate of the maximum strain energy value that governs the damage variable η through the strain energy density and equation (62) in chapter 2. The values for damage variable for these peak strains amount to 0.22 for the peak strain in calcified plaque and 0.19 for the Echolucent plaque.

It can be observed that the damage energy is concentrated at the area of contact and therefore larger in the plaque layers than in the medial and adventitial layers. Detailed results of damage energy have been presented in a later section.

Results for 180C case

For the 180C case, the results were seen to be similar to the results in 90 C case. The stress field is concentrated near the calcified plaque and echolucent plaque layers.

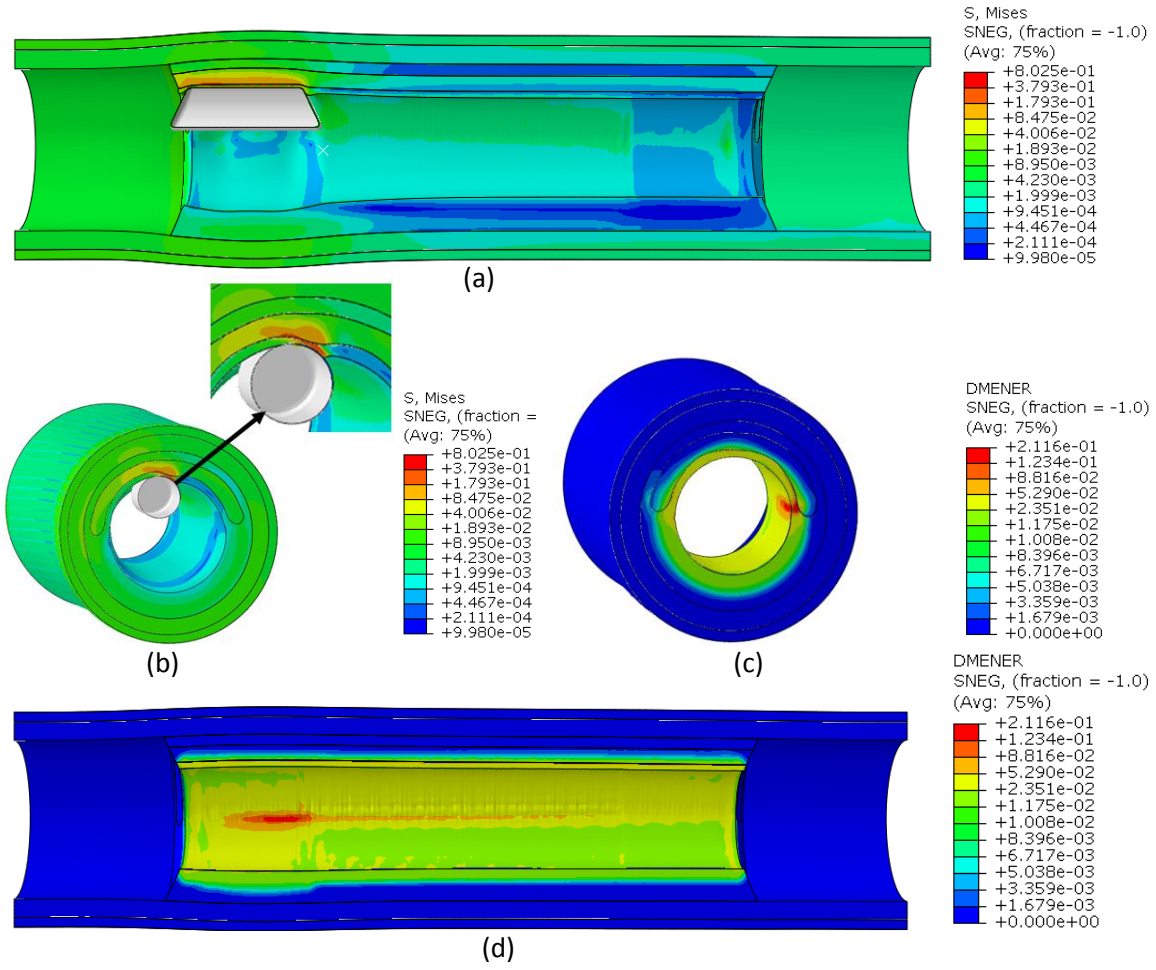

Figure 6.9: *Equivalent Mises stress -axial section (a), Equivalent mises stress- cross-section at t=2sec (b). Damage energy after OA simluation -cross-section (c), damage energy after OA simulation -axial section (d), for 180C*

The peak stress in the media and adventitia shown in Figure 6.9 in this case at the instant of 2 sec are seen to be 29.3 KPa and 17.5 KPa as compared to 282KPa in the calcium and 802 KPa in the echolucent plaque and the need for the 270C case was not felt since the stress distribution in both the 180C and 90C cases was similar wherein the damage and peak stresses in the media and adventitia are quite small in comparison to the plaque layers in contact with the crown.

6.4.2 Mesh convergence

Three mesh densities were used for the 90 degree calcified plaque case to gage the mesh convergence. The first mesh was a coarse mesh of the size 434810 elements; second mesh was the same as the one used in the previously reported OA simulation for 90C case and had a mesh size of 775710 elements as mentioned earlier; the third mesh was refined further to 1082430 elements. The peak stresses observed at the 2 second instant were examined and the percentage error was calculated. The error for the coarse mesh was found to be larger than 5%. Therefore the mesh was refined further. The change in the peak stress values between the second and third mesh was 3.6% which was within the generally acceptable 5% error criterion. The number of elements for the atherectomy simulations is much larger than the angioplasty simulations since coarser meshes were seen to not be mesh convergent and no symmetry model was used for OA simulations. The equivalent mises stress from the 2nd and 3rd mesh density is shown in figure 6.10.

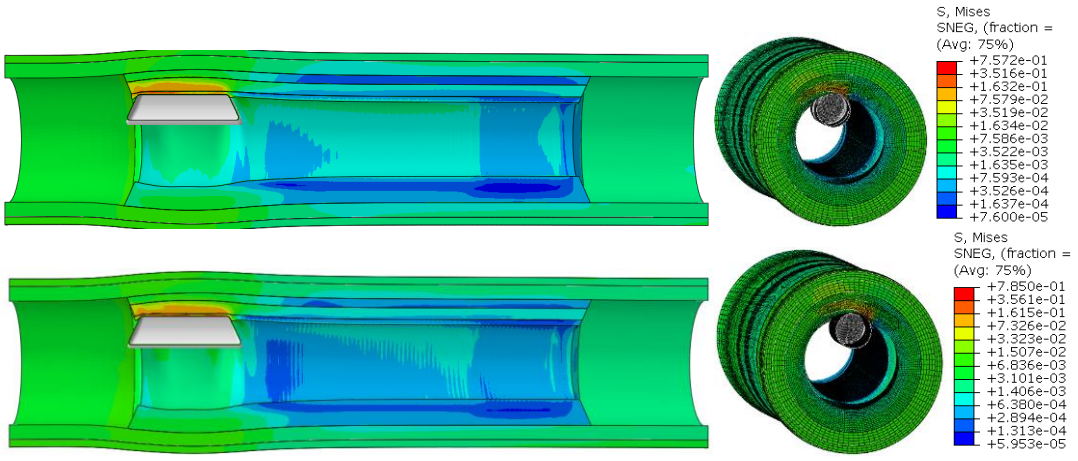

Figure 6.10: *Equivalent Mises stress (axial section) at t=2sec for mesh size of 775710 and 1082430 elements respectively*

It can be seen in figure 6.10, that the solution for the stress field in the 2nd and 3rd mesh densities are quite similar and the error in the magnitude is small. Thus the 2nd mesh was converged.

6.4.3 Results with inclusion of permanent set

Cyclic tests from Maher et al [6] also demonstrated a permanent strain obtained in the plaque after unloading of the compression samples. Therefore in order for the OA simulations to capture the reality of the physical situation better, this phenomenon must be included. These permanent strains can be accounted for using Mullins effect with permanent set [67]. The results for the 90 degree calcification case including permanent set effect for the plaque models have been shown below in Figure 6.11

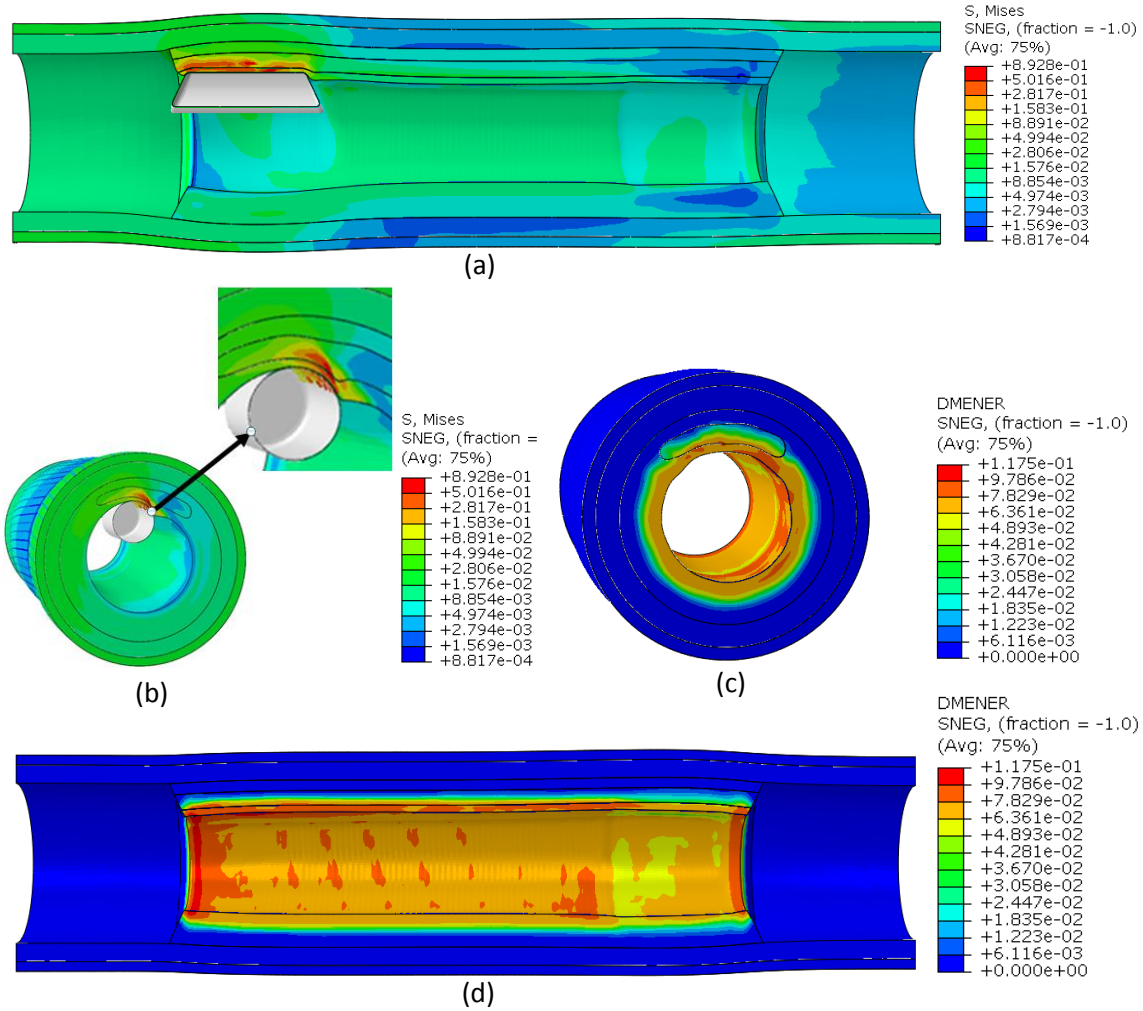

Figure 6.11: *Equivalent Mises stress -axial section (a), Equivalent mises stress -cross-section(b), at t=2sec, damage energy after OA simluation -cross-section (c), damage energy after OA simulation axial view(d) for 90 degree calcification with permanent set*

Accounting for the permanent set in the material, it can be seen that the stress in the calcified layer is larger than in the simulation without permanent set shown in Figure 6.7. The stress in the Media and adventita is seen to be 50.6 KPa and 25.2KPa respectively and are seen to be smaller than the stresses in the calcification and echolucent plaque which are 851KPa and 893KPa respectively.

6.4.4 Material damping parameter study

Proportional damping has been used in the OA and PTA simulations presented. Thus a fundamental theory and solution sensitivity analysis of proportional damping is in order.

Rayleigh's mass and stiffness proportional damping factors are used to construct an artificial damping matrix $\mathbf{C}$ as a linear combination of mass and stiffness matrices such that,

$$\mathbf{C} = \alpha\,\mathbf{M} + \beta\,\mathbf{K}$$

In the absence of a first order time derivative term in the governing equation of solid mechanics, and due to the use of a time independent material model, the $\mathbf{C}$ matrix is absent and may be constructed through Rayleigh's coefficients α and β. Mass proportional damping as stated by Abaqus Analysis Manual [33] introduces damping caused by absolute velocities of the model in a sense that it gives a damping contribution proportional to the mass matrix of the element. In Abaqus explicit, the factor α is multiplied to the lumped mass matrix to define a diagonal matrix $\mathbf{C}$. Evaluation of appropriate damping parameters for a large system is quite involved since it needs the evaluation of the eigenfrequencies of the model. Therefore only estimates of damping parameters are used here and results for the same are compared.

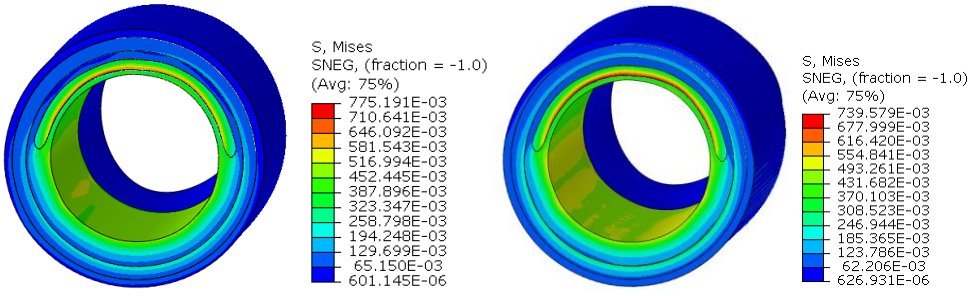

Figure 6.12: *Equivalent Von Mises stress distribution for α = 0 (no damping) and α = 500 case in balloon angioplasty simulations*.

Damping parameters of $\alpha = 0$ and α=500 are used to study the PTA simulations. The stress field distributions for both the cases seem to be quite similar. It was seen that using a damping factor of $\alpha = 0$ and $\alpha = 500$, the change in the peak stress in the model was around 4.6%. The reason for the relatively small variation in the solution may be as a result of the low velocity terms involved in the simulation of angioplasty. The sensitivity of the solution to damping in OA simulations however, was seen to be much larger. At low or no damping, large oscillations were observed in the OA simulations. These large oscillations may be interpreted as manifestation of low frequency modes which can be damped using mass proportional damping without significantly affecting the stable time increment [33]. Mass proportional damping parameters of 0, 100 and 500 were used for the damping parameter study in OA simulations. Excessive element distortions were observed in damping parameters of 0 and 100 and the solution failed possibly due to a negative element jacobian arising from element inversion. The α=500 case was much more stable to element distortions. The OA and PTA simulations reported in this study therefore use a damping parameter α =500. A detailed damping study was not carried out in this research and is probably in order for high speed simulations like OA.

6.4.5 Damage energy density analysis for OA

The damage energy density for the above OA simulations described above has been shown in the table below.

	Mean Damage energy density (MJ/m^3)				Total Damage energy Density	Percentages			
	Calcification	Echolucnet plaque	Media	Adventitia		Calcification	Echolucnet plaque	Media	Adventitia
90C OA	3.26E-03	8.46E-03	1.23E-04	4.96E-06	1.18E-02	27.52	71.40	1.04	0.04
180C OA	4.30E-03	1.17E-02	1.30E-04	6.11E-06	1.61E-02	26.65	72.51	0.81	0.04
90C OA with Permanent set	3.08E-02	3.28E-02	2.05E-04	1.55E-05	6.38E-02	48.26	51.39	0.32	0.02

Table 6.2: Damage energy density for the different components of the lesion for OA simulations

From Table (5.3), it can be concluded that the media experiences about 0-1% damage and the adventitia experiences about 0-0.05% damage. The plaque layers directly in contact with the crown or in vicinity of the crown during the procedure underwent the most amount of damage energy dissipation. The percentage of damage with increasing degree of calcification was quite similar in rows 1 and 2. Inclusion of permanent set increased

the damage energy density in the calcification since the peak stresses in the calcified layer also increased. The percentage damage in the medial and adventitial layers is quite small as compared to their PTA counterparts which might suggest that OA has a local field of effect.

6.4.6 Change in compliance after orbital atherectomy procedure

The damage energy plots for the OA simulations illustrate the softening in the plaque layers due to the procedure. The damage in different locations of the plaque is different therefore the local compliance change is variable depending on how much damage energy was dissipated at that location. In order to characterize the overall change in compliance of the lesion as a whole, a dynamic internal pressure is applied to the internal surface. Compliance with and without OA was calculated as the slope of the pressure area curve and the percentage change was evaluated. Lumen cross-sectional areas were calculated at internal pressure levels of 40, 80, 120 and 160mmHg which lie around the range of the blood pressures observed for a healthy individual. The results have been shown in the Figures 6.13 and 6.14 below.

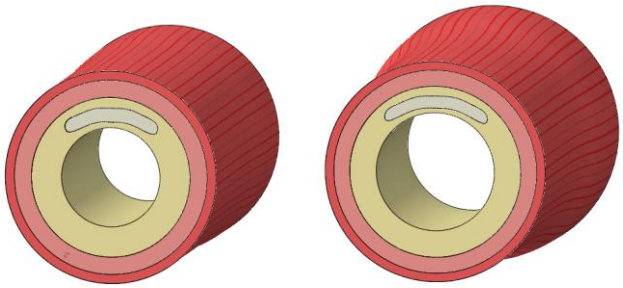

Figure 6.13: *Deformed shape at internal pressure of 40mmHg and 160mmHg for lesion without OA procedure*

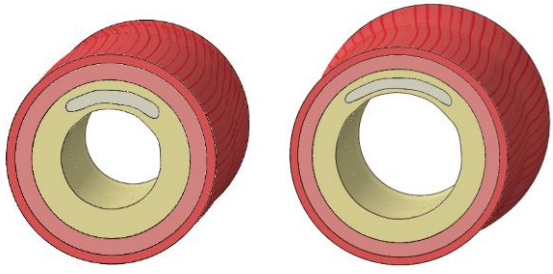

Figure 6.14: *Deformed shape at internal pressure of 40mmHg and 160mmHg for lesion after OA procedure*

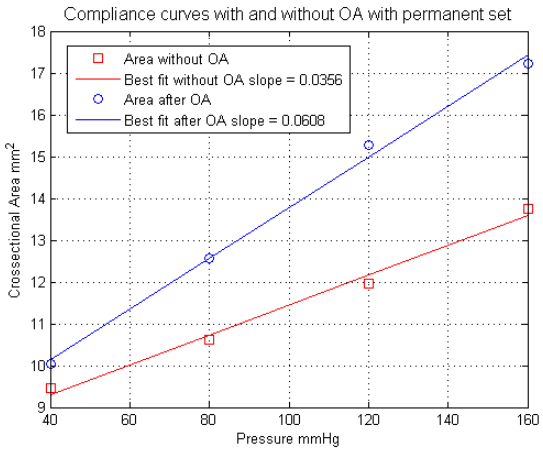

Figure 6.15: *Compliance curves for lesion with and without OA procedure*

As seen in figure 6.15, the slopes of the area pressure curves shown above determine the compliance of the lesion. A linear best fit line is constructed through the observed data points and its slope is evaluated. The larger the slope, the greater the compliance at the given pressure levels. The compliance within this range of operation for a lesion after OA procedure is seen to be $0.0608\,\frac{mm^2}{mmHg}$ and for the lesion without OA procedure is seen to be $0.0356\,\frac{mm^2}{mmHg}$. Therefore for the given range of operation there is a 70.8% increase in compliance of the lesion after OA procedure.

Dattilo et al [31] in their study on comparison of PTA with OA followed by PTA, reported that "plaque modification rather than maximum debulking is the OA objective" and that "pretreatment with OA may possibly result in decreased vessel wall injury via diminished deep wall dissection along with reduced barotrauma afforded by lower balloon pressures". It would be of interest to simulate the response of the lesion to PTA post OA and determine the stresses in the arterial wall to investigate the change in compliance of the vessel at high balloon pressures. However as discussed in chapter 4, the material model for plaque that has been modelled for atherectomy is not accurate at high tensile strains observed in angioplasty which therefore limits this model. Therefore, increase in compliance at low pressure levels has been established using the above simulations. Future work using material models accurate in tension and in compression needs to be done.

6.4.7 Crown Force analysis

Zheng et al [64] presented the grinding forces measured using a piezoelectric dynamometer during experimental OA study in a phantom artery. The magnitude of the forces ranged from 0 to 0.5N with a mean force of 0.2N at 120,000 rpm which was reported as an orbiting speed of 40Hz.

Magintude of equivalent forces acting on the crown during OA simulations were output and were found to be close to the range of values observed in the aforementioned experimental study. The force vs time plot is shown in figures (6.16, 6.17, 6.18) below. The first 0.5 seconds simulate the radial displacement of the crown to 0.5mm after which the crown is fixed radially as discussed in the boundary conditions section 6.3.2. The crown rotation ranges from t=0.5 seconds to t=4.5 seconds after which the crown is withdrawn.

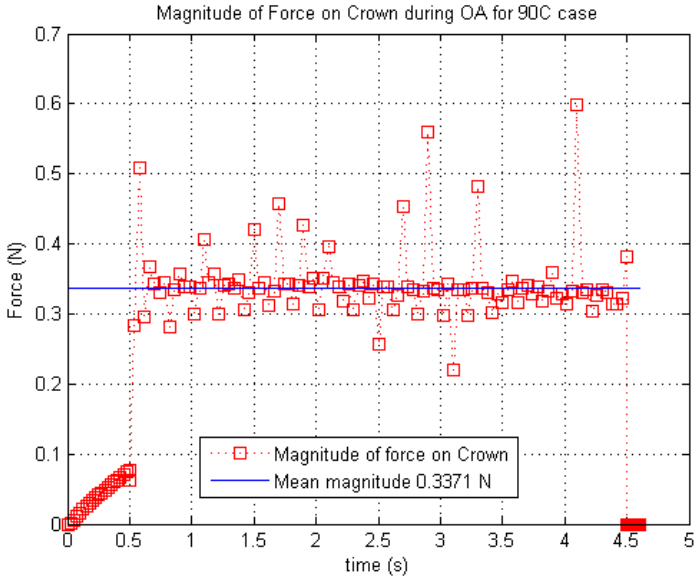

Figure 6.16: *Magnitude of force on the OA crown during 90C OA simulation and the resultant mean magnitude*

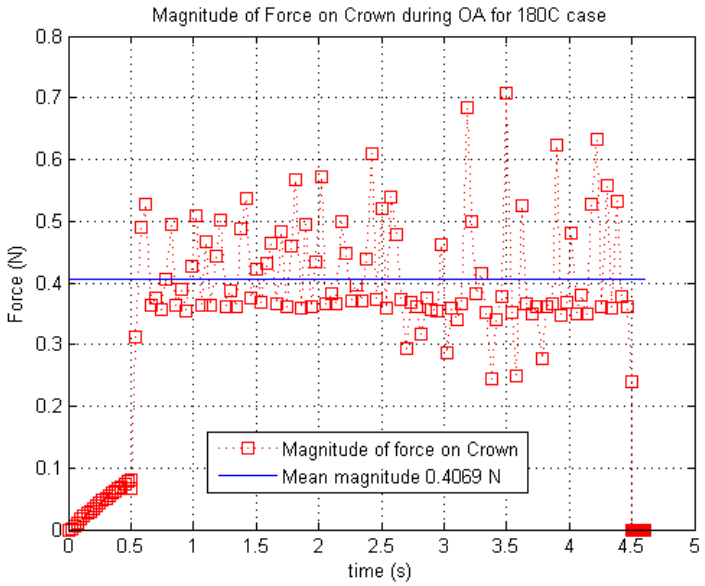

Figure 6.17: *Magnitude of Force on the OA crown during 180C OA simulation and the resultant mean magnitude*

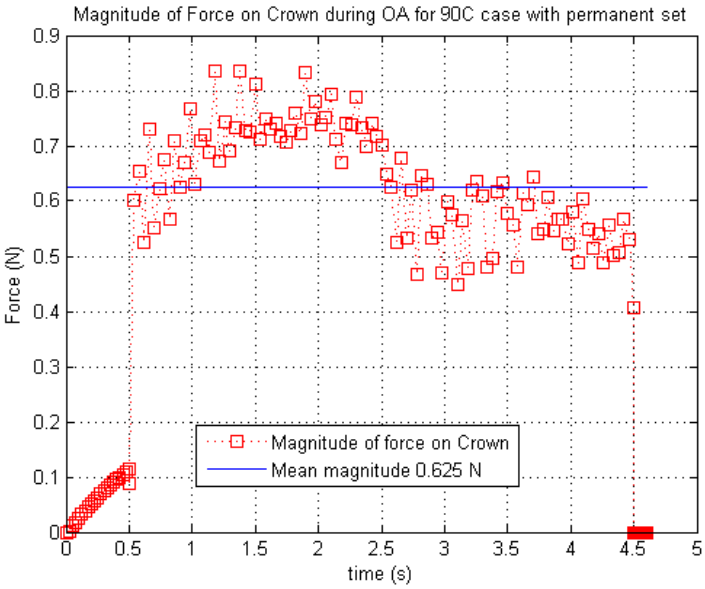

Figure 6.18: *Magnitude of Force on the OA crown during 90C OA simulation with permanent set and the resultant mean magnitude*

As seen in the figures above, there is an oscillation in the magnitude of force. This is expected since as the crown moves, it moves from the vicinity of the harder calcification to the softer plaque therefore experiencing different reaction forces. Also,

due to the inclusion of permanent set, the reaction force magnitude in Figure 6.18 drops after the first pass of 2 seconds. The mean magnitudes in the 90C, 180C and 90C with permanent set case were found to be 0.337 N, 0.407N and 0.625N and are close to the magnitude of force obesrved by Zheng et al [64]. The mean was calculated for the orbiting and translation time of the crown from t=0.5 to t=4.5 sec.

7. DISCUSSION, LIMITATIONS AND FUTURE WORK

7.1 DISCUSSION

Treatment procedures like percutaneous transluminal angioplasty and orbital atherectomy are being used extensively to treat cardiovascular diseases. Vascular injury during treatment procedures is seen to be an important marker for restenosis of the lesion. Peak stresses induced in the artery especially in the media may be an important measure to predict the vessel damage and injury. Therefore, simulations of percutaneous transluminal angioplasty and orbital atherectomy were conducted to study the effect of changing lesion characteristics on stresses in the vessel wall.

A typical diseased superficial femoral artery histology image was used as a template to create idealized lesion models with 90, 180 and 270 degree calcification arcs. The increase in extent of calcification through increasing calcium arcs was consistent with intravascular ultrasound study by Murray et al [60]. Performing angioplasty simulations on 90C, 180C, and 270C models, it was observed that calcification may serve as protection to the medial and adventitial layers during PTA in the portion surrounded by calcium arcs. However increasingly higher peak stresses are observed in the non-calcified portion of the media and adventitia which is consistent with the observation by Ivan Casserly [61]

The 180C case was then considered for further simulations to determine the effect of plaque softening on stresses in the media under the action of a semi-compliant balloon. Decreasing the stiffness and therefore increasing the compliance of the plaque components decreased the peak stresses observed in the media. Therefore softening the plaque components may decrease the chances and degree of vascular injury during PTA under the action of a semi-compliant balloon.

Mesh convergence study for PTA simulations was carried out using 3 mesh sizes in the 180C case. Once a converged mesh was obtained, similar mesh densities were used for the other cases as well.

Accounting for the ultimate tensile stresses (UTS) in the plaque components and the arterial tissue, perfect plasticity was added to the material models with their respective UTS values. Note that perfect plasticity suggests that once the stress crosses the maximum permited value, no more stress is generated with increasing strain therefore the material in-effect has no stiffness on further loading. No plastic strains were observed in the media and adventitia since the stresses didn't cross the UTS values. The results for the model with plasticity were presented. The stresses observed in the media and adventitia are smaller in this case than the 180C case without plasticity which may reinforce the finding that softening the plaque components may reduce the stresses in the wall under the action of a semi-compliant balloon. The results of the original SFA model with inclusion of plasticity were also presented. The peak stresses in the wall were seen to develop in the non-calcified portion and near the shoulder regions of the calcification.

Damage energy density analysis was performed for PTA. The simulations presented and mean damage energy density of the different layers of the lesion was compared. It was concluded that the media and adventitia undergo 7-11% and 1-4% damage respectively. Also as the degree of calcification was increased, the amount of mean and percentage damage energy in the wall components decreased which demonstrated that, even though the peak stresses are higher, they are more localized.

Orbital atherectomy simulations were carried out on 90 and 180C cases to characterize the relative damage energy and peak vessel wall stresses. A 90C case with permanent set included in the plaque model as seen in experimental observations by Maher et al [6], was also simulated. It was observed that the wall stresses in the media and adventitia were much smaller during OA as compared PTA simulations. The stress field was more localized to the vicinity of the contact region of the crown. This shows that OA should be used in heavily diseased and calcified lesions where the contact region of the crown will be concentrated at the plaque burden.

The damage energy density analysis demonstrated 0 to 1% and 0-0.05% damage dissipation in the media and adventitia which is smaller than the values observed in PTA simulations. The peak stresses and damage energy density results from the OA

simulations suggest that softening of plaque components may be possible without inducing significant vascular injury to the media and adventitia using OA procedure.

The compliance of the lesion without OA and post-OA procedure was measured at low pressure levels. The results of the simulations show that there was an increase in the compliance of the lesion at low pressures, due to softening of the tissue during OA simulations. This observation is consistent with the experimental study conducted at Cardiovascular Systems Inc. by Deokar and Nguyen.

7.2 LIMITATIONS AND FUTURE WORK

It is important to realize and address the limitations of the work presented in the course of this research. Tissue material data in the compressive and tensile loading conditions were selected from different sources since, to the writer's knowledge, no experimental results for cyclic loading of plaque tissues in tension and compression are available in the literature. Cyclic loading data available in the compressive regime was extended onto the tensile regime based on a justification provided in the section (4.2). Experimental data based on cyclic uniaxial tensile and compressive tests of plaque tissue from the same sources would be ideal. Atherosclerotic plaque as represented in the experimental studies, were assumed to be isotropic materials. However in reality due to the fibrous deposits in the plaque, the nature of the behavior could be anisotropic. In addition as discussed in section (4.2.1), some amount of compressibility has been permitted in the material models for practicality of computational effort. Biological tissues are known to exhibit time rate dependent behavior and viscoelastic effects. Such effects have not been taken into account in this work and therefore qualify as a limitation of the study. Also, residual stresses and axial pre-stretch of the vessel have not been accounted for in this study. A damping parameter study was carried out and the damping parameter suitable for the OA simulations was determined. However a damping study based on experimentally observed results and eigenfrequencies must be carried out for high speed simulations like OA. The Mullin's effect model based on discontinuous damage theory was used for the damage of the plaque components and the arterial layers. A continuous damage model would probably result in a different solution. However due to the ease of fitting

parameters to the discontinuous type model, the continuous type models are rarely used in literature to model atherosclerotic plaque.

In absence of cyclic compression and tensile tests on human atherosclerotic plaques in the femoral artery, carotid plaque properties have been used. Similarly cyclic tensile properties of human thoracic aorta presented by Weisbecker et al [14] were used since, to the author's knowledge, no cyclic tensile tests on SFA were available in the literature. Frictionless interactions were used to model the interaction between the balloon/OA crown and the lesion in absence of known friction coefficients. The formation of a fluid (blood) layer between the crown and the lesion would make this a reasonable assumption.

In addition, although plasticity and permanent set effects have been taken into account in some of the simulations, plaque removal (given the extremely small size of the particulates from sanding [90]) and tear/fracture in the tissue has not been accounted for which may be an important effect of these interventional procedures. Internal luminal pressures were not applied during the simulation of PTA and OA since the material properties from various sources have been derived in-vitro are already damaged up to physiological loading conditions. Application of physiological loading conditions would therefore damage the material which should be avoided.

The geometry of the lesion was assumed to be constant throughout its length since it was constructed from a 2D histology image. 3D models constructed from high resolution MRI scans as have been used in [25] would be able to capture the stress and damage response of the lesion better. The fiber orientations in the medial and adventitial layers are modelled using a cylindrical co-ordinate system which therefore can be represented perfectly for the idealized cylindrical geometries. However for the original SFA model, the directions will be a little deviant since the circumferential direction of the lesion must change at every point around the perimeter. Therefore individual elements would need to be given their own individual co-ordinate system that has a variable orientation depending on its location around the periphery.

The number of samples used in the experimental investigation of change in compliance was 2, which is small. Therefore a study with much larger number of samples is in order for the experimental work to be statistically significant.

For future work, material models based on experimental stress-strain data of the plaque tissue from the same source must be used. This material data may be more likely to produce a Drucker stable material model in tension and compression. The advantage of such a model would be that a sequential simulation of PTA and OA could be carried out to study the change in lesion compliance at high pressure levels.

A displacement based approach for the crown dynamics during OA has been used in this research based on the study by Zheng et al [64]. A force based approach with stiffness of the guide-wire and mass of the crown taken into account would provide a better understanding of the lesion response. Fluid-dynamics may influence the motion of the crown therefore, if possible, fluid structure interaction should be modelled to characterize the dynamics of the crown.

REFERENCES

[1] L. HM, G. AJ, P. SY, G. LJ and L. RT, "Static and circumferential tangential modulus of human atherosclerotic tissue," *J Biomechanics,* 1993.

[2] I. Pericevic, C. Lally, D. Toner and D. J. Kelly, "The influence of plaque composition on underlying arterial wall stress during stent expansion : The case for lesion-specific stents," *Medical Engineering & Physics 31 (2009) 428–433,* 2009.

[3] E. Maher, A. Creane, S. Sultan, N. Hynes, C. Lally and DanielJ.Kelly, "Tensile and compressive properties of fresh human carotid atherosclerotic plaques," *Journal of Biomechanics 42(2009)2760–2767,* 2009.

[4] D. M. Ebenstein, D. Coughlin, J. Chapman, C. Li and L. A. Pruitt, "Nanomechanical properties of calcification, fibrous tissue, and hematoma from atherosclerotic plaques," *Wiley InterScience,* 2007.

[5] M. G.Lawlor, M. R.O'Donnell, B. M.O'Connell and M. T.Walsh, "Experimental determination of circumferential properties of fresh carotid plaques," *Journal of Biomechanics 44(2011)1709–1715,* 2011.

[6] E. MAHER, A. CREANE, S. SULTAN, N. HYNES and C. LALLY, "Inelasticity of Human Carotid Atherosclerotic Plaque," 2011.

[7] M. Koji Imoto, M. P. Takafumi Hiro, M. P. Takashi Fujii, A. Murashige, P. MD, M. Yusaku Fukumoto, M. Genta Hashimoto, M. P. Takayuki Okamura, M. P. Jutaro Yamada, P. Koji Mori and M. P. F. Masunori Matsuzaki, "Longitudinal Structural Determinants of Atherosclerotic Plaque Vulnerability," *Journal of Americal College of Cardiology Vol. 46, No. 8, 2005,* 2005.

[8] G. C. Cheng, H. M. Loree, R. D. Kamm, M. C. Fishbein and R. T. Lee, "Distribution of Circumferential Stress in Ruptured and Stable Atherosclerotic Lesions :A Structural Analysis With Histopathological Correlation," *Journal of Americal Hear Association 1993;87:1179-1187,* 1993.

[9] H. M. Loree, R. D. Kamm, R. G. Stringfellow and R. T. Lee, "Effects of fibrous cap thickness on peak circumferential stress in model atherosclerotic vessels," *Journal of the Americal Heart Association 1992;71:850-858,* 1992.

[10] G. A. Holzapfel, G. Sommer, C. T. Gasser and P. Regitnig, "Determination of layer-specific mechanical properties of human coronary arteries with nonatherosclerotic intimal thickening and related constitutive modeling," *Am J Physiol Heart Circ*

Physiol 289: H2048–H2058, 2005..

[11] C. Lally, S. Dally, A.J.Ried, T.C.Lee, D.Quinn and F.Dolan, "Analysis of Prolapse in Cardiovascular Stents: A Constitutive Equation for Vascular Tissue and Finite-Element Modelling," *Journal of Biomechanical engineering,* 2001.

[12] E. GULTOVA, L. HORNY, H. CHLUP and R. ZITNY, "AN ANISOTROPIC PSEUDO-ELASTIC MODEL FOR THE MULLINS EFFECT IN ARTERIAL TISSUE," in *XI International Conference on Computational Plasticity.*.

[13] L. Horny, E. Gultova, H. Chlup, R. Sedlacek, J. Kronek, J. Vesely and R. Zitny3, "Mullins effect in human aorta described with limiting extensibility evolution," in *MEDICON 2010, IFMBE Proceedings 29, pp. 768–771, 2010*, 2010.

[14] H. Weisbecker, D. M. Pierce, P. Regitnig and G. A. Holzapfel, "Layer-specific damage experiments and modeling of human thoracic and abdominal aortas with non-atherosclerotic intimal thickening," *Journal of the mechanical behavior of biomedical materials 12(2012)93-I06,* 2012.

[15] R.W.Ogden and D.G.Roxburgh, "A pseudo-elastic model for the Mullins effect in filled rubber," *The royal society,* 1998.

[16] M. L, "Effect of stretching on the properties of rubber," *J. Rubber Res 16 275-289,* 1947.

[17] D. Balzani, J. Schroder and D. Gross, "A Simple Model for Anisotropic Damage with Applications to Soft Tissues," in *Proc. Appl. Math. Mech. 4, 236–237 (2004).*

[18] D. Balzani, J. Schröder and D. Gross, "Simulation of discontinuous damage incorporating residual stresses in circumferentially overstretched atherosclerotic arteries," 2006.

[19] D. Balzani and T. Schmidt, "Comparative analysis of damage functions for soft tissues: Properties at damage initialization," *Mathematics and mechanics of solids,* 2013.

[20] B. Calvo, E.Pena, M.A.Martinez and M. Doblare, "An uncoupled directional damage model for fibred biological soft tissues. Formulation and computational aspects," *International journal for numerical methods in engineering Int. J. Numer. Meth. Engng 2007; 69:2036–2057*, 2007.

[21] E. Peña, J. A. Peña and M. Doblaré, "On the Mullins effect and hysteresis of fibered biological materials: A comparison between continuous and discontinuous damage

models," *International Journal of Solids and Structures 46 (2009) 1727–1735,* 2009.

[22] D. Laroche, S. Delorme, T. Anderson and a. R. DiRaddo, "Computer Prediction of Friction in Balloon Angioplasty and Stent Implantation," 2006.

[23] D. Martin and F. Boyle, "Finite Element Analysis of Balloon-Expandable Coronary Stent Deployment: Influence of Angioplasty Balloon Configuration," *INTERNATIONAL JOURNAL FOR NUMERICAL METHODS IN BIOMEDICAL ENGINEERING,* 2013.

[24] C. CONWAY, F. SHARIF, J. P. MCGARRY and a. P. E. MCHUGH, "A Computational Test-Bed to Assess Coronary Stent Implantation Mechanics Using a Population-Specific Approach," *Cardiovascular Engineering and Technology, Vol. 3, No. 4, December 2012 pp. 374–387,* 2012.

[25] G. A. Holzapfel, M. Stadler and C. A. Schulze-Bauer, "A layer-specific 3D model for the simulation of balloon angioplasty using MR imaging and mechanical testing," 2002.

[26] T. C. Gasser and G. A. Holzapfel, "Finite element modeling of balloon angioplasty by considering overstretch of remnant non-diseased tissues in lesions," *Comput. Mech. (2007) 40: 47–60,* 2005.

[27] C. Conway, J.P.Mcgarry and P.E.Mchugh, "Modelling of Atherosclerotic Plaque for Use in a Computational Test-Bed for Stent Angioplasty," 2014.

[28] F. ERIC D. GRASSMAN MD, M. F. SARAH A. JOHNSON and M. F. RONALD J. KRONE, "Predictors of Success and Major Complications for Primary Percutaneous Transluminal Coronary Angioplasty in AcuteMyocardial Infarction : An Analysis of the 1990 to 1994 Society for Cardiac Angiography and Interventions Registries," *Journal of American College of Cardiology,* Vols. Vol. 30, No. 1 July 1997:201–8, 1997.

[29] M. GLENNN . LEVINE and N. P. C. M. J. L. M. P. D.A, "Restenosis Following Coronary Angioplasty: Clinical Presentations and Therapeutic Options," *Clin. Cardiol. 18, 693-703 (1995),* 1995.

[30] A. IJsselmuiden, P. Serruys, A. Scholte, F. Kiemeneij, T. Slagboom, L. v. Wieken, G. Tangelder and G. Laarman, "Direct coronary stent implantation does not reduce the incidence of in-stent restenosis or major adverse cardiac events," *European Heart Journal (2003) 24, 421–429,* 2003.

[31] E. Faglia, L. D. Paola, G. Clerici, J. Clerissi, L. Graziani, M. Fusaro, L. Gabrielli, S.

Losa, A. Stella, M. Gargiulo, M. Mantero, M. Caminiti, S. Ninkovic, V. Curci and A. Morabito, "Peripheral Angioplasty as the First-choice Revascularization Procedure in Diabetic Patients with Critical Limb Ischemia: Prospective Study of 993 Consecutive Patients Hospitalized and Followed Between 1999 and 2003," *Eur J Vasc Endovasc Surg 29, 620–627 (2005),* 2005.

[32] R. Ferraresi, M. Centola, M. Ferlini, R. D. Ros, C. Caravaggi, R. Assaloni, A. Sganzaroli, G. Pomidossi, C. Bonanomi and G. Danzi, "Long-term Outcomes after Angioplasty of Isolated, Below-the-knee Arteries in Diabetic Patients with Critical Limb Ischaemia," *Eur J Vasc Endovasc Surg (2009) 37, 336e342,* 2009.

[33] M. F. JULES Y. T. LAM, M. F. JAMES H. CHESEBRO, M. B. (. F. PETER M. STEELE, P. MRINAL K. DEWANJEE, P. UNA BADIMON and M. F. VALENTIN FUSTER, "Deep Arterial Injury During Experimental Angioplasty: Relation to a Positive Indium-Ill-Labeled Platelet Scintigram, Quantitative Platelet Deposition and Mural Thrombosis," *JACC Vol. S. No. 6 December 1986:1J8G-6,* 1986.

[34] M. Andrew Cragg, M. Wilfrido R. Castañeda—Zuñiga and M. Kurt Amplatz, "Pathophysiology of Transluminal Angioplasty," in *SEMINARS IN INTERVENTIONAL RADIOLOGY VOLUME 1, NUMBER 4 DECEMBER 1984,* 1984.

[35] C. Rogers, D. Y. Tseng, J. C. Squire and E. R. Edelman, "Balloon-Artery Interactions During Stent Placement A Finite Element Analysis Approach to Pressure, Compliance, and Stent Design as Contributors to Vascular Injury," *Circulation Journal of the American Heart Association,* Vols. 84:378-383, 1999.

[36] C. AW, C. MM, F. J and R. MA, "Kinetics of cellular V. Role of acute distension in the induction of smooth muscle proliferation," *Lab Invest. 1989;70:360 –364.,* 1989.

[37] W. LN, R. MM and B. DE., "Endothelial healing following defined injury to rabbit aorta: depth of injury and mode of repair," *Arteriosclerosis 1983;47:123–130.,* 1983.

[38] S. IJ, L. PJ, S. SL, T. I, S. J, H. C and E. MD., "Influence of inflation pressure and balloon size on the development of intimal hyperplasia after balloon angioplasty: a study in the atherosclerotic rabbit.," *Circulation. 1989;80:1029 –1040.,* 1989.

[39] H. JW, S. JS, J. R, M. RG, G. S, S. MP, B. TA, V. G, C. M, T. AS, W. HB, M. JR, H. JA and P. CJ, "Restenosis after coronary angioplasty: a multivariate statistical model to relate lesion and procedure variables to restenosis," *J Am Coll Cardiol.*

1991;18:647– 656, 1991.

[40] R. GS, D. J. Jr and K. S. III, "Influence of balloon size on initial success, acute complications, and restenosis after percutaneous transluminal coronary angioplasty," *Circulation. 1988;78:557–565.*, 1988.

[41] K. RE, S. RD, C. JP, F. RF, M. M and B. DS., "The importance of acute luminal diameter in determining restenosis after coronary atherectomy or stenting," *Circulation. 1992;86:1827–1835.*, 1992.

[42] P. MJ, B. C and K. RE., "The relative importance of arterial remodeling compared with intimal hyperplasia in lumen renarrowing after balloon angioplasty," *Circulation. 1994;89:2816 –2821,* 1994.

[43] A. HR, M. M, T. M and F. E., "Remodeling rather than neointimal formation explains luminal narrowing after deep vessel wall injury," *Circulation. 1996;93:1716 –1724,* 1996.

[44] K. T, C. JW, H. CC, R. TJ and F. DP., "Differences in compensatory vessel enlargement, not intimal formation, account for restenosis after angioplasty in the hypercholesterolemic rabbit model," *Circulation. 1994;89:2809 –2815,* 1994.

[45] T. SHK, G. EJ, Z. Y, L. W, v. E. F and P. H, "Effect of balloon angioplasty on femoral artery evaluated with intravascular ultrasound imaging," *Circulation 86:483–493,* 1992.

[46] V. R, F. A and B. AP, "Coronary angioplasty from the perspective of atherosclerotic plaque: morphologic predictors of immediate success and restenosis.," *Am Heart J 127:163–179,* 1994.

[47] B. J, d. M. C, O. Y, E. J, G. R, d. F. P, R. JR and S. PW, "Impact of plaque morphology and composition on the mechanism of lumen enlargement using intracoronary ultrasound and quantitative angiography after balloon angioplasty," *Am J Cardiol 77:115–121,* 1996.

[48] C.-Z. W, "Pathophysiology of transluminal angioplasty. In: Meyer J, Erberl R, Rupprecht HJ (eds) Improvement of myocardial perfusion," *pp 138–141. Martinus Nijhoff Publisher, Boston,* 1985.

[49] S.-B. CAJ, R. P and H. GA, "Mechanics of the human femoral adventitia including high-pressure response," *Am J Physiol. Heart Circ Physiol 282:H2427–H2440 2002.,* 2002.

[50] Z. CL, S. E, S. R, C. J, B. WF, C.-Z. WR and A. K, "Transluminal angioplasty evaluated by electron microscopy," *Radiology 153:369–374,* 1994.

[51] M. Attila Thury, M. Glenn van Langenhove, M. Stephane G. Carlier, M. Mariano Albertal, M. Ken Kozuma, M. Evelyn Regar, M. George Sianos, P. Jolanda J. Wentzel, M. P. Rob Krams, P. Cornelis J. Slager, M. P. Jan J. Piek and P. Parick W. Serruys MD, "High shear stress after successful balloon angioplasty is associated with restenosis and target lesion revascularization," *AMERICAN HEART JOURNAL 2002.123110,* JULY 2002.

[52] R. D. Lovik, J. P. Abraham and E. M. Sparrow, "Assessment of possible thermal damage of tissue due to atherectomy by means of a mechanical debulking device," in *Proceedings of the ASME 2008 Summer Bioengineering Conference (SBC2008),* 2008.

[53] R. D. Safian, K. Niazi, J. P. Runyon, D. Dulas, B. Weinstock, V. Ramaiah and R. Heuser, "Orbital Atherectomy for Infrapopliteal Disease:Device Concept and Outcome Data for the Oasis Trial," *atheterization and Cardiovascular Interventions 73:406–412 (2009),* 2009.

[54] N. W. Shammas, R. Lam, J. Mustapha, J. Ellichman, G. Aggarwala, E. Rivera, K. Niazi and N. Balar, "Comparison of Orbital Atherectomy Plus Balloon Angioplasty vs. Balloon Angioplasty Alone in Patients With Critical Limb Ischemia," *J ENDOVASC THER 2012;19:480–488,* 2012.

[55] M. Raymond Dattilo, M. Stevan I. Himmelstein and M. R. Robert F. Cuff, "The COMPLIANCE 360° Trial: A Randomized, Prospective Multicenter, Pilot Study Comparing Acute and Long-Term Results of Orbital Atherectomy to Balloon Angioplasty for Calcified Femoropopliteal Disease," *INVASIVE CARDIOL 2014;26(8):355-360,* 2014.

[56] K.I.Romanov, "The drucker stability of a material," *Journal of Applied Mathematics and Mechanics, Vol65 Issue1,* pp. 155-162, Feb 2001.

[57] "ABAQUS (2014) `ABAQUS 6.14 Analysis User's Manual'. Online Documentation Help: Dassault Systèmes.".

[58] "Uvahealth," [Online]. Available: uvahealth.com .

[59] S. W. Murray, B. Patel, R. H. Stables, R. A. Perry and N. D. Palmer, "Site-specific intravascular ultrasound analysis of remodelling index and calcified necrosis patterns reveals novel blueprints for coronary plaque instability," *Cardiovasc Diagn*

Ther 2014;4(4):287-298 10.3978/j.issn.2223-3652.2014.07.03, 2014.

[60] H. F, G. J and M. P, "multiscale approach to failure assessment in deployment for cardiovascular stents," *Multiscale Model 2010;2:1–22*, 2010.

[61] M. B. IVAN P. CASSERLY, "The Role of Atherectomy in the Femoropopliteal Artery," *SUPPLEMENT TO ENDOVASCULAR TODAY SEPTEMBER 2009,* 2009.

[62] M. F. F. J. A. MUSTAPHA, "Atherectomy Today: Go Slow to Finish Fast, An update on the newest generation of atherectomy devices and how this technique is currently being used to treat peripheral vascular disease".*ENDOVASCULAR TODAY OCTOBER 2011.*

[63] "Cardiovacular Systems Inc," [Online]. Available: http://www.csi360.com/.

[64] Y. Zheng, B. Belmont and A. J. Shih, "Experimental Investigation of the Grinding Wheel Dynamics in Atherectomy," in *43rd Proceedings of the North American Manufacturing Research*, 2015.

[65] M. E.G, B. J. A and C. N. J, "Arterial Compliance," *Willerson, J. T., Cardiovascular medicine, Springer, London, pp 1811-1831, Chap. 58.*.

[66] H. K, "Experimental approaches on measuring the mechanical- properties and constitutive laws of arterial- walls," *J. Biomech. Eng.-Trans. ASME, 115(4), 481-488.*, 1993.

[67] A. Dorfmann and R. Ogden, "A constitutive model for the Mullins effect with permanent set in particle-reinforced rubber," *International Journal of Solids and Structures 41 1855–1878,* 2004.

[68] G. Holzapfel, T. Gasser and R. Ogden, "A new constitutive framework for arterial wall mechanics and a comparative study of material models," *Journal of Elasticity 61, (2000) 1-48,* 2000.

[69] "Texas Heart Institute," [Online]. Available: http://www.texasheart.org/HIC/Anatomy/anatomy2.cfm.

[70] M. Alan S. Go, D. M. MD and F. DrPH, "Heart Disease and Stroke Statistics—2014 Update," *Circulation. 2014;129:e28-e292,* 2014.

[71] [Online]. Available: http://www.lifebeat.pt/uk/exams-and-services/coronary-artery-disease/].

[72] Herbert.C.Stary, Atlas of Atherosclerosis: Progression and regression, Perthenon

Publishing, 2003.

[73] M. ROBERT A . VOGEL, "Coronary Risk Factors, Endothelial Function, and Atherosclerosis: A Review," *Clin. Cardiol. 20,426-432 (1997).*

[74] A. D. Michaels, MD and M. F. Kanu Chatterjee, "Angioplasty Versus Bypass Surgery for Coronary Artery Disease," *Circulation. 2002;106:e187-e190.*

[75] T. W. Duerig and M. Wholey, "A comparison of balloon- and self-expanding stents," *Min Invas Ther & Allied Technol 2002: 11 (4) 173-178.*

[76] [Online]. Available: http://www.hopkinsmedicine.org/healthlibrary/test_procedures/cardiovascular/percutaneous_transluminal_coronary_angioplasty_ptca_and_stent_placement_92,P07981/ .

[77] R. Wessely, "New drug-eluting stent concepts," *Nature Reviews Cardiology 7, 194-203 (April 2010).*

[78] A. D, H. CJ and W. CM, "Nitinol stent fractures in the SFA".*Endovas Today 2004;7:22-34.*

[79] N. A, S. HB and O. K, "Fracture of self-expanding nitinol stents stressed in vitro under simulated intravascular conditions.," *J Vasc Surg. 2008;48:435-440.*

[80] M. Matthew I. Tomey, M. Annapoorna S. Kini and M. Samin K. Sharma, "Current Status of Rotational Atherectomy," *Jacc Cardiovascular intervention Vol7,* 2014.

[81] "Boston Scientific Jetstream," [Online]. Available: http://www.bostonscientific.com/en-US/products/atherectomy-systems/jetstream-atherectomy-system.html.

[82] "Boston Scientific Rotablator," [Online]. Available: http://www.bostonscientific.com/en-US/products/atherectomy-systems/rotablator-rotational-atherectomy-system1.html.

[83] T. WULFMAN, "Jetstream® Aspirating Revascularization Technology From calcium to thrombus: an overview of the evolution of this technology," *SUPPLEMENT TO ENDOVASCULAR TODAY ,* SEPT 2009.

[84] "Covidien," [Online]. Available: http://www.ev3.net/peripheral/us/plaque-excision/.

[85] N. I. Akkus, A. Abdulbaki, E. Jimenez and N. Tandon, "Atherectomy devices: technology update," *Medical devices : Evidence and Research,* 2015.

[86] M. P. Peter J. Fitzgerald, M. F. Thomas A. Ports and M. F. Paul G. Yock, "Contribution of Localized Calcium Deposits to Dissection After Angioplasty, An Observational Study Using Intravascular Ultrasound," *Circulation. 1992;86:64-70,* 1992.

[87] J. Bonet and R. D. Wood, Nonlinear Continuum Mechanics for Finite Element Analysis, Cambridge University Press, 1997.

[88] S. B. L. Beomkeun Kim1, J. Lee, S. Cho, H. Park, S. Yeom and S. H. Park, "A Comparison Among Neo-Hookean Model, Mooney Rivlin Model, and Ogden Model for Chloroprene Rubber," *INTERNATIONAL JOURNAL OF PRECISION ENGINEERING AND MANUFACTURING Vol. 13, No. 5, pp. 759-764.*

[89] G. A. Holzapfel and R. W. Ogden, Biomechanics of Soft Tissue in Cardiovascular Systems, SpringerVienna, 2003.

[90] M. Richard R. Heuser, M. Robert Safian, M. Marc Bosiers and M. Mark A. Turco, "Orbital Atherectomy : Initial experiences with a new system for the percutaneous treatment of peripheral vascular stenosis," *ENDOVASCULAR TODAY,* SEPTEMBER 2006.